Three-dimensional Quantitative Visualization for Mechanics of Discontinuous Materials

Thesis by
Kimberley Ann Mac Donald

In Partial Fulfillment of the Requirements for the
Degree of
Doctorate of Philosophy in Mechanical Engineering

CALIFORNIA INSTITUTE OF TECHNOLOGY
Pasadena, California

2020
Defended 6 August 2019

To the girl, young or old, who builds, makes, tinkers, and dreams.
To my mother, a constant inspiration.

ACKNOWLEDGEMENTS

Most people who have undertaken a PhD would likely agree that it is not a task that can be completed alone. A great many people have made this thesis possible both directly and indirectly. To thank each of them is a daunting task, but in the next several paragraphs I will attempt to acknowledge some of them.

First, thank you to my advisor, Ravi Ravichandran for his cheerful greetings of "hey, how’s it going?" and constant encouragement to "just do it!" Thank you also for introducing me to so many varied topics and avenues for exploration. Thank you to José Andrade for seeing a potential for my work far beyond anything I could have seen myself. I would also like to thank Kathy Faber for her astounding influence on me as a person, a mentor, and a researcher. To Melany Hunt, thank you for agreeing to serve on my committee, and for allowing me to be a part of your outreach efforts in Giving Voice. Thank you also to Mike Mello for always being interested in talking about whatever I have on my mind and for many great discussions on my research.

For most of my time at Caltech, I was fortunate to be a part of an interdisciplinary fracture mechanics research group. Thank you to Kaushik Bhattacharya, Ravi Ravichandran, Kathy Faber, and Blaise Bourdin for teaching me so much and for helping me think critically about my work from a variety of perspectives. I also need to thank the students and post docs in this group for their constant support, ideas, and encouragement: Louisa Avellar, Stella Brach, Neal Brodnik, Chun-Jen Hsueh, and Nha Tran.

Thank you to Ryan Hurley for mentoring me through my first Summer at Caltech. I appreciate all the time and energy you put into guiding me. Thank you also to Eloïse Marteau for teaching me how to use GEM, sharing your codes and example data, and helping me trouble shoot when I ran into problems. Thank you to Bob Grubbs for teaching me polymer chemistry and helping me understand and improve my inverse suspension polymerization method. Thank you to Red Lhota for training me on the rheometer, for helping me in polymer chemistry class, and for being an incredibly helpful and kind person.

This work would also not have been possible without the expertise of Petros Arakelian, Bruce Dominguez, John Van Deusen, and Ali Kiani. I cannot begin to thank Mike Allegro and Randy Meyers (aka my Nikon fairies) enough for all the time, effort, and knowledge they poured into helping me. Andres Collazo and Steven

Wilbert in the Biological Imaging Facility have been similarly invaluable. I also need to thank several past members of Ravi's research group. In particular, thank you to Jacob Notbohm and Christian Franck for passing on so much of your microscopy and image correlation knowledge. Thank you also to the Ravi and Kaushik research groups: Louisa, Zach, Christian, Owen, Matt, Moriah, Paul, Dingyi, Jin, Vinamra, Tomo, Tori, Ying Shi, Zev, Korhan, Leah, and many others.

Thank you to all the friends (whether at Caltech or elsewhere) who have been with me through this adventure. Your support and encouragement has been incredible: Zoila, Rachel, Ellen, Melissa, Voon, Bekah, Kirsti, Serena, Emily, Camille, Josh, Abbey, Zach, Rachel, Christie, Justin, Nina, Terri, Jim, Lisa, Debi, Joseph, BD, Russel, and Thomas. Thank you in particular to Blaire, Georgina, Hanako, and Alex for being there for me even though we have been physically far apart for the past few years.

Thank you to my first research advisor, Jim Giancaspro at the University of Miami. I would not be where I am today without the support and guidance you gave me. Thank you also to my research mentors and mentees, you have taught me so much in out short time together: Shan Yuan, Lauren Millman, Eunice Yoon, and Polina Verkhovodova.

Thank you also to my mother. Your support of me has been unwavering and I do not think I would have been able to do this without your encouragement. Thank you to my sister for being there through thick and thin. Thank you also to my grandfather for the stories that captured my interest and led me to science and engineering.

Any research of course requires funding. I am grateful to the National Science Foundation for supporting me through the Graduate Research Fellowship under Grant No. DGE-1144469. I am also grateful to have been a part of the fracture mechanics work conducted for National Science Foundation Award No. DMS-1535083 under the Designing Materials to Revolutionize and Engineer our Future (DMREF) program. My work on granular materials was sponsored by the Department of the Defense, Defense Threat Reduction Agency (HDTRA1-12-0041). The content of the information does not necessarily reflect the position or the policy of the federal government, and no official endorsement should be inferred. And finally, thank you to the Biological Imaging Facility where the majority of imaging for this work was conducted, with the support of the Caltech Beckman Institute and the Arnold and Mabel Beckman Foundation.

ABSTRACT

The complexity and multiscale nature of material microstructures introduces significant intricacies to many mechanics problems for which we do not have a full theoretical understanding. Under loading, these microstructures can introduce significant nonlinearities that cannot be described sufficiently by current theories and models. This leads us to consider experiments we could perform to improve our understanding of such effects. This thesis describes the design of experiments exploring two aspects of material microstructure effects: (i) crack propagation and renucleation in soft brittle polymers and (ii) interparticle forces in granular materials.

First, experimental and analysis methods are developed to study fracture mechanics in soft brittle polymers with the goal of developing a more detailed understanding of the effects of microstructural heterogeneities on crack propagation and renucleation in three-dimensions. To better understand these processes, experiments on crack propagation in thin soft polymers using confocal microscopy images are conducted. Traditional metrics associated with crack propagation including stress intensity factor (SIF, K) and energy release rate (ERR, G) are calculated by direct measurement of the crack tip opening displacement (CTOD, δ_t) on the sub-millimeter scale. Errors in these calculations are comparable to those reported in the literature for more traditional fracture experiment geometries. Fluorescent speckle images are captured using confocal microscopy imaging, a fast and low cost 3D optical imaging technique, to study crack geometry during propagation. Images of renucleation events are also captured allowing investigation of factors contributing to slow crack roughening observed by earlier researchers. The goal of this study is to provide an experimental method to enhance understanding of crack interactions with microstructural heterogeneities and of renucleation events, which can significantly improve our ability to design material toughness.

To begin to understand the effects of engineered microstructural heterogeneities such as inclusions in materials, we must be able to produce such engineered systems and understand the interparticle interactions. To this end, a method to manufacture volumetrically speckled spheres in-house with controlled diameters was developed. Additionally, an experimental method combining confocal microscopy with digital volume correlation (DVC) was also used to study interparticle force transmission in 3D. Analysis of an in-plane 2D projection of volumetric surface data shows that three-dimensional effects play a significant role in the deformation of granular assemblies. Study of a single grain in 3D demonstrates progress in experimental capabilities and highlights the need for more studies to validate existing numerical models and theories for granular matter. Analysis of particle scale deformations and strains with the Granular Element Method (GEM) allows us to determine inter-particle forces and understand the development and evolution of force chains in a granular assembly under a wide variety of loading conditions. These experiments can also lead to development of new understanding of the effects of inclusions on material properties, processes, and damage evolution.

PUBLISHED CONTENT AND CONTRIBUTIONS

[1] K. A. Mac Donald and G. Ravichandran. “Confocal microscopy and digital volume correlation methods for intergranular force transmission experiments”. *Experimental Techniques*, 2018. DOI: `10.1007/s40799- 018-0292-8`.
K.A.M.D. participated in the conception of the project, conducted the experiments, analyzed the data, and wrote the manuscript.

[2] K. A. Mac Donald and G. Ravichandran. “Crack propagation and renucleation in soft brittle hydrogels”. 2019. *Submitted*.
K.A.M.D. participated in the conception of the project, conducted the experiments, analyzed the data, and wrote the manuscript.

TABLE OF CONTENTS

LIST OF ILLUSTRATIONS

LIST OF TABLES

NOMENCLATURE

Abbreviations

µCT	Micro-computed tomography
AFM	Atomic force microscopy
CTOD	Crack tip opening displacement, δ_t
DEM	Discrete element method
DIC	Digital image correlation
DVC	Digital volume correlation
GEM	Granular element method
PMT	Photomultiplier tube
ROI	Region of interest
SEM	Scanning electron microscopy
SIF	Stress intensity factor, K
XRD	X-ray diffraction

Symbols

δ	Crack opening profile
$\delta\Omega$	Derivative of the volume, the surface, used for integration
δ_t	Crack tip opening displacement
ϵ	1D strain
γ	Surface energy
μ	Bulk modulus
$\nabla\cdot$	Divergence, dot product of the gradient operator with a vector field
∇	Gradient operator
ν	Poisson's ratio
Ω	The volume, used for integration
ρ	Mass density

$\underline{\epsilon}$	Stain tensor
$\underline{\sigma}$	Stress tensor
$\underline{a}$	Acceleration vector
$\underline{b}$	Body force vector
$\underline{n}$	Normal vector
$\underline{u}$	Displacement vector
A	Area
a	Crack length
d	Spatial dimension
E	Young's modulus
G	Energy release rate
G_c	Critical energy release rate
J	Rice's J-integral, see J. R. Rice, *J. Appl. Mech,* 35(2):379–386, 1968.
K	Stress intensity factor
K_c	Critical stress intensity factor
r	Radius, in polar coordinates the distance from the origin
r_t	The distance from the crack tip to the point where crack tip opening displacement is measured
r_{NL}	Estimate of the size of the nonlinear region
S	Surface area
U	Potential energy
V	Volume

Terminology

Confocal Common focus, often refers to confocal microscopy which uses pinholes and objective lenses to capture light from a single point in volumetric space

Fractography The study of fracture surfaces using images to identify key characteristics of the fracture event

Pixel 2D image unit representing a measure of illumination for a single point in a 2D plane

Voxel A 3D or volumetric pixel representing a measure of illumination for a single point in 3D space

Chapter 1

INTRODUCTION

The goal of the work described in this dissertation is first and foremost to advance understanding of the mechanics of materials beyond continuum models and toward improving deformation and damage models and predictions. This is achieved by employing three-dimensional (3D) quantitative visualization techniques such as digital image and digital volume correlation (DIC, DVC) to characterize the full-field displacements. By moving away from thinking of materials as a continuum and toward thinking of them as a discontinuous material system, we can broaden the scope of both material models and damage models while learning more about the complexity of mechanical processes that impact the behavior of the material system.

1.1 Motivation

If we think about a traditional engineering material such as metal, we can think about the grain structure and how the crystal structure of each grain affects the stiffness and toughness of a component manufactured from that metal. Typically, we, as engineers, are happy to know that models and design parameters predict that our component will not fail under some load limit. But we also desire to know what will happen if that load limit is exceeded. When and where will the component fail? The scientist in us now begins to ask how will it fail?

The deformation, fracture, and damage mechanics models we use today are largely based on these traditional engineering materials like metals where we can look at simple crystal structures and identify the associated slip and cleavage planes, and based on the crystal orientation in each grain we can tell which slip plane will be activated or along which cleavage planes the material will fail [1–4]. We can then quantify the accumulation of damage in the material. When we think about plasticity, even in metals, the damage process becomes significantly more complex [5, 6]. Additionally, there are many engineering materials in use today that are not metals and that do not have these crystal structures. Wood, masonry, and concrete are used extensively in the building industry. Fiber reinforced polymers (FRP) and ceramics (FRC) are used throughout the automotive and aerospace industries, and we are starting to see soft polymers come into use as load bearing materials in the biomedical field [7–10]. While we can think about some of these materials as having grain-like structures, or even having components with grain structures similar to what is seen in metals, the grains do not have the same interface properties as the grains in metals. Wood has a complex directional cellular structure where cells have layered walls and each wall is composed of a network of cellulose fibrils in a cellulose and lignin matrix [11]. Concrete has a cementitious matrix around sand and gravel particles that each have their own underlying granular structure [12]. Similarly FRP and FRC have a polymer or ceramic matrix respectively around fibrous inclusions that may be randomly dispersed or ordered in a woven mat [13]. Taking a polymer alone, there is a great deal of complexity in the chain entanglements or cross-linked network structure that significantly alters how we think about damage processes [14].

The complexity of the materials described above goes beyond the material system. Much of the research conducted on these materials measures global or continuum level behavior. In order to understand local behavior, full-field methods such as image correlation are employed but are often limited to the outer surface of the material [15]. Probing the full complexity of the three-dimensional nature of these material systems is typically a challenging and costly endeavor involving diffraction and tomography methods [10, 16–23].

This thesis presents experimental methods and work on fracture and granular mechanics problems using model materials or systems. Material properties, parameters, and mechanics quantities are measured from optical images and used to demonstrate the capabilities of these experimental methods as well as to improve our understanding of material deformation and damage processes.

1.2 Discontinuous Materials

Rather than thinking about the global behavior of a material or component, we want to understand how the microstructure of the material affects its local behavior and properties. Throughout this thesis polymers are used as model materials to study brittle fracture and granular mechanics. The structure and fracture behavior of the polymer itself is also of interest beyond its use as a model brittle material.

Polymers

Polymers are chains of many monomers chemically bonded to each other. If the chains are relatively short as in Fig. 1.1(b), the polymer behaves as a viscous liquid. Once the chains reach a critical length they begin to entangle as demonstrated in Fig. 1.1(c) and the polymer transitions to behaving more like a solid [14]. Crosslinking can be used to form a network polymer where the chains are not only entangled, but are also chemically bonded to each other, typically resulting in a stiffer more elastic solid material [24–29]. Some of these crosslinked network polymers are hydrophilic and absorb water into the pores formed between the chains. Fig. 1.1(d) demonstrates the polymerization of poly(acrylamide-bis-acrylamide) copolymer, the network hydrogel used in this thesis and (f) shows a diagram of how the network swells when it absorbs water [30–34].

As polymers deform under loading their chains move and reorient. In the case of an entangled chain polymer, the individual chains can move relative to each other. Longer chains are typically more entangled which limits this motion [14]. If the polymer is networked, the chains have fixed bonds to other chains or to themselves, directly limiting relative motion of the chains at these crosslink sites [33].

Damaged and fractured materials

Many polymers, including polyacrylamide, have very brittle fracture behavior. This means they possess low fracture toughness and energy, and fractography shows smooth fracture surfaces without indicators of plasticity such as voids or large permanent deformations. Traditional fracture theories predict that these polymers will exhibit fracture behavior and properties similar to other very brittle materials like ceramics and glasses [34, 35].

Unlike these very stiff brittle materials, hydrogels are very compliant with stiffnesses several orders of magnitude lower than those of ceramics, glasses, and even structural polymers such as PMMA. This means that the deformations at failure in gels are expected to be several orders of magnitude larger, and thus more easily measurable, than in the stiffer materials [35]. When a crack propagates in a sheet of glass, the crack opening before propagation is on the order of nanometers [36]. Scanning electron microscopy (SEM) is one of the few methods by which such small features can be measured. Conducting fracture tests on glasses *in-situ* in an SEM presents many challenges that limit further study of brittle fracture [37]. However, in a typical soft gel, the crack opening at propagation is in the tens to hundreds of micrometers or larger [7, 38]. At this scale, the crack is measurable via numerous optical techniques. This allows for a wide array of experimental configurations to advance understanding of brittle fracture processes using a polymer gel as a model brittle material.

Continuum level models of fracture typically account for damage via a single pa-

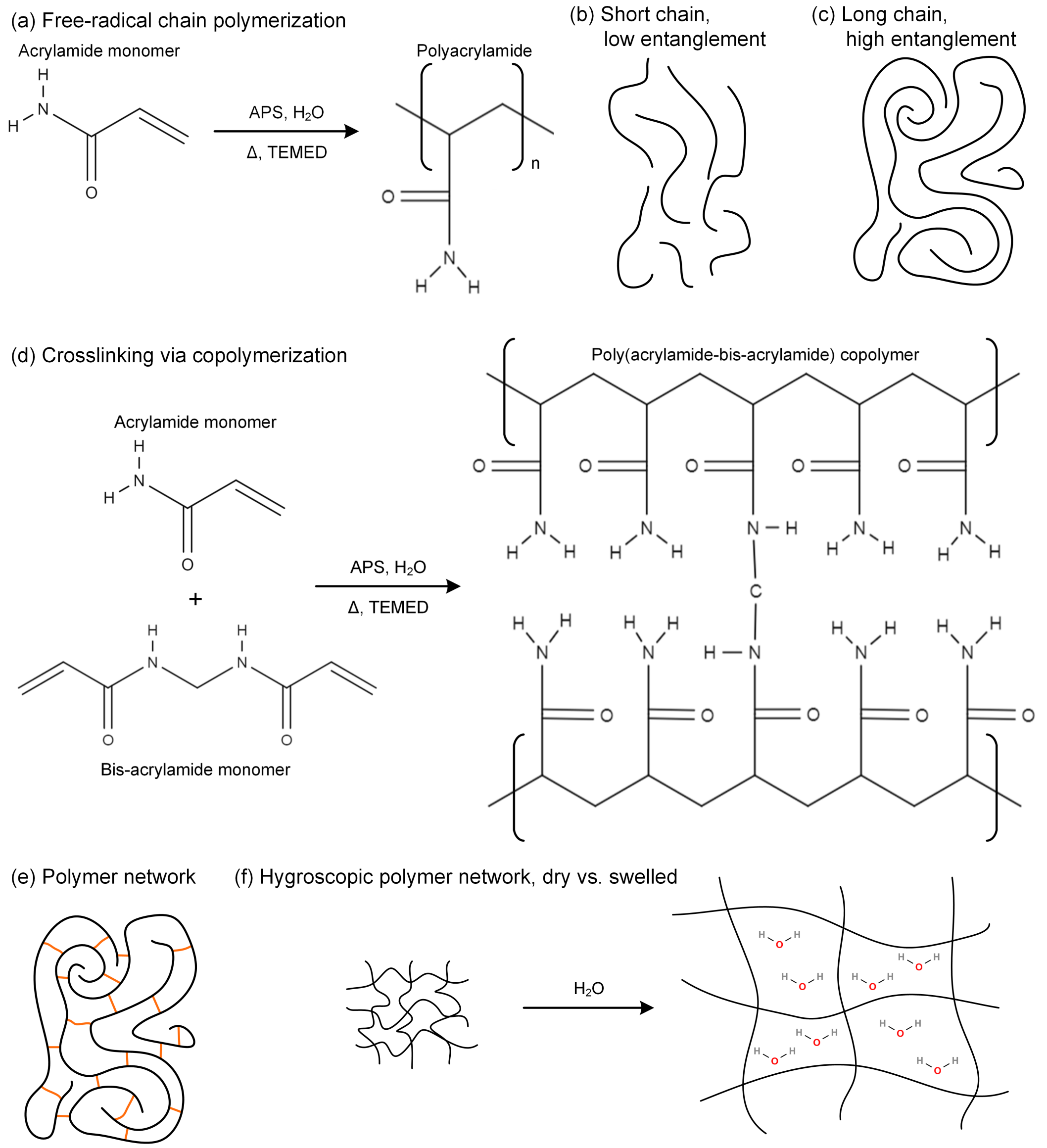

Figure 1.1: Polyacrylamide systems: (a) Free-radical chain polymerization of the acrylamide monomer to form polyacrylamide. Diagrams demonstrating (b) short chain polymer with low entanglement and (c) long chain polymer with high entanglement. (d) Copolymerization of acrylamide and bis-acrylamide monomers to form network poly(acrylamide-bis-acrylamide) copolymer. (e) Diagram of a polymer network where crosslinks are shown in orange. (f) Diagram demonstrating the dry and swelled states of a hygroscopic polymer network.

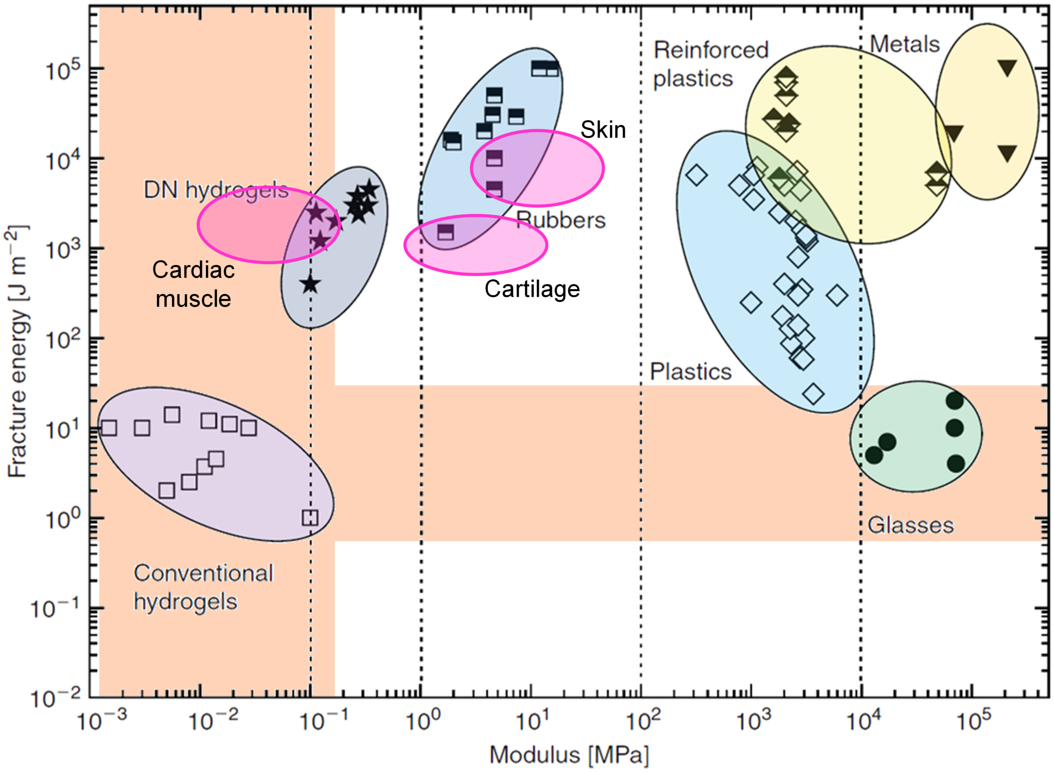

Figure 1.2: Ashby plot of stiffness modulus versus fracture energy for several materials. Adapted from Naficy et al. (2011) with permission from CSIRO Publishing [34]. Typical property ranges for conventional hydrogels are highlighted in orange and typical properties for human biological tissues are shown in pink.

rameter. In some formulations, when this parameter is equal to one the material is undamaged and when it is equal to zero the material is completely damaged and can no longer bear load. This is classified as failure or fracture [39, 40]. However, such a model does not describe or account for the processes that lead to the damage and fracture.

In brittle materials, fracture initiates at a critical flaw such as a microcrack or pore. The critical microstructural discontinuity grows into a macro-scale crack and becomes a continuum level discontinuity [41]. In modeling, these features can be accounted for through several methods including the damage parameter described above. Experimentally, the discontinuity introduced by a crack can be more challenging. Experimental methods to measure full-field displacements and strains (see Section 1.4) must account for errors due to the formation and propagation of a crack. This can be achieved via several methods such as manually removing the crack from the region of interest (ROI) or through integration methods that identify cracks through sharp changes in deformation gradients [42–45].

Over the last several years, advances in additive manufacturing technology have opened the way for designing, engineering, and printing microstructured materials. Several systems exist that allow for printing in multiple materials with different mechanical properties. For example, the Statasys Connex3 allows for a single print to use up to three different polymer materials with different mechanical properties. This printer can also mix the base polymers allowing for a range of material properties in a single print. Several researchers have begun exploring how this technology can be used to design material systems with enhanced fracture properties.

Several experiments on enhancing the adhesive properties of tape by using variation in the tape stiffness have demonstrated in a one-dimensional sense that elastic contrast interfaces between regions of different stiffnesses produce a toughening effect [46–48]. This work has been extended to the two-dimensional case using the Stratasys Connex3 and similar technologies to produce material systems with a wide array of toughening geometries. The simplest of these is a striped geometry with alternating stiff and compliant stripes normal to the crack [49, 50]. Circular and moon shaped inclusion arrays have also been studied as well as brick and mortar type arrays inspired by the structure of nacre [51]. All of these geometries are, however, two-dimensional and do not fully take advantage of the opportunities additive manufacturing technology allows.

Nevertheless, these studies show the powerful toughening effect engineered material discontinuities can have on the fracture properties of materials. Further study of these effects is needed to be able to effectively design such microstructures.

Heterogeneities have been shown to strongly impact stress fields near a crack tip, resulting in effective mixed mode fracture [20, 21, 52, 53]. This also influences crack front shape [54]. However, relatively few studies have sought to explore the 3D crack shape experimentally, except via fatigue [16, 22]. Fatigue cracks can be simpler to study in 3D because one can pause the loading for imaging without impacting the crack propagation. However, imaging an actively propagating crack in 3D is significantly more difficult due to imaging time constraints. Those studies that do explore 3D fracture via experiments or simulations show that understanding the 3D nature of crack shape and stress fields is necessary, especially in heterogeneous materials [52, 54].

Granular media

Particle inclusions is one of the many ways we can toughen a material. From nanoparticles in rubber to sand and gravel aggregates in concrete, particle inclusions affect stress distributions and increase the energy necessary for a crack to propagate through a material [55–60]. While granular materials are of interest as toughening mechanisms, their mechanical properties and behavior without a matrix are also of great interest.

From building foundations and overpass embankments to food grains and pharmaceuticals, the unique mechanical behavior of granular materials impacts our lives on a daily basis. When we think about foundations and embankments, we want these structures to behave like solids. But when we think about commercial processing of grains and pharmaceuticals, we want to take advantage of granular flow. Depending on grain size and shape as well as boundary conditions like slope angles and retaining walls, a given load may be supported but the grains or they may flow [61–66].

To understand these phenomena and when a granular structure will transition from behaving like a solid to flowing like a fluid, we need to think about the structure in terms of its individual grains rather than approximating it as a continuous material [67–70]. Similarly, when we think about particles as toughening inclusions, there is a lot to learn about the mechanisms of toughening by understanding how the inclusion and matrix deform and fracture as separate entities. In this way, we can view granular materials as discontinuous. We can also view a material that has been toughened via particle inclusions as discontinuous.

1.3 Mechanics

According to the Collins English Dictionary, mechanics describes "the branch of science, divided into statics, dynamics, and kinematics, concerned with the equilibrium or motion of bodies in a particular frame of reference." In the field of mechanics of materials, we typically use the classical mechanics formulations based on Newton's Laws of Motion. First the concept of equilibrium which can be described for a deformable body in general form by Eq. 1.1

$$\nabla \cdot \underline{\sigma} + \rho \underline{b} = \rho \underline{a}, \tag{1.1}$$

where $\underline{\sigma}$ is the stress in the body, ρ is the mass density of the body, $\underline{b}$ are the body forces acting on the body, and $\underline{a}$ is the acceleration of the body. This general form of equilibrium can be derived from balance of linear momentum.

Balance of angular momentum can be used to show symmetry of the stress tensor for the continuum as written in Eq. 1.2

$$\underline{\sigma} = \underline{\sigma}^{\intercal}, \tag{1.2}$$

where $(\cdot)^{\intercal}$ indicates the transpose.

These two equations are, however, not enough to describe the deformations that result form the action of the forces on a body. To relate the forces to deformations, or stresses to strains, a constitutive material model is required. Currently, material models are not derived from fundamental physics but rather are determined by fitting experimental data to a pre-defined model. Depending on the material, scale, boundary conditions, and loading, different models can be used [71].

In the simplest case, we make several assumptions: First we assume the material is a homogeneous continuum, then we further assume isotropy, meaning the material behavior is independent of loading direction. We then assume the material has a linear elastic response to loading, or in 1D, $\sigma = E\epsilon$, where E is the Young's modulus or stiffness of the material and ϵ is the strain [71]. For small deformations in traditional materials with simple geometries and loading conditions, this linear elastic isotropic constitutive model works well. However, it does not account for stresses that exceed the material's elastic limit. When the yield stress is exceeded, plastic deformations begin, and when the ultimate stress is exceeded it can no longer carry any load [60]. Ductile materials typically experience significant permanent deformations before failure while brittle materials typically fail with little evidence of yielding.

There are several methods to account for plastic yielding and failure in material models. Perhaps one of the simplest is to assume an elastic perfectly plastic model. That is, to assume that once the yield stress is reached, the material no longer supports additional load and the stress cannot increase, as illustrated in Fig. 1.3. Although this model allows the material to yield, it does not describe final failure of the material. For this, we need to turn to fracture mechanics.

Fracture mechanics

Consider an infinite plate under far-field stress σ_∞ with a semi-infinite crack as shown in Fig. 1.4 [72–75]. If we assume the material is linear elastic, then the stress concentration at the crack tip is infinite. However, as we know, real materials have limited strength, so the stress beyond its capacity must somehow be dissipated.

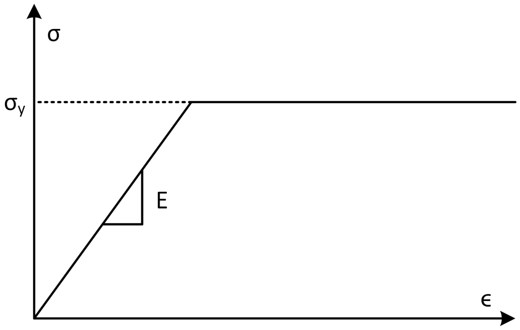

Figure 1.3: Elastic perfectly plastic material model for 1D tension loading.

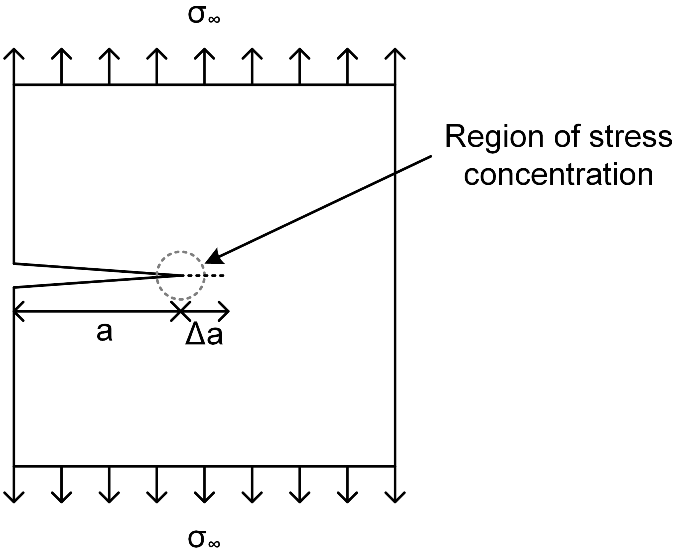

Figure 1.4: Infinite plate with an edge crack of length, a subjected to far field loading, σ_∞.

The effect of stresses on a deformable body can be understood as the energy needed to deform that body by a fixed amount. Thus, excess energy can be thought of as the energy which is expended by forming or propagating a crack through the material. Griffith described this as the potential energy and related it to the energy needed to break atomic bonds [72, 73]. He defined a critical energy release rate as

$$G_c = 2\gamma, \tag{1.3}$$

where γ is the energy needed to create a new surface and a crack is considered to consist of two newly created surfaces [76].

While this very simple equation only describes perfectly brittle materials, the concept of defining and measuring fracture energy is very powerful. We can describe more general fracture using this idea of energy release rate or the energy necessary to propagate the crack in Fig. 1.4 by the infinitesimal distance Δa as

$$G = -\frac{\delta U}{\delta a}, \tag{1.4}$$

where U is the potential energy and a is the initial crack length [72, 73].

Brittle materials have much lower critical fracture energies than more ductile materials. Often, fracture toughness is measured and described by the critical stress intensity factor (SIF), K_c , rather than the critical fracture energy, G_c, for traditional engineering materials. Since K_c is related to G_c and the material's stiffness by Eq. 1.5 we can think of the fracture energy as the square of the toughness normalized by the stiffness [72, 73].

$$G_c = \frac{K_c^2}{E'}, \tag{1.5}$$

where

$$E' = \begin{cases} E & \text{for plane stress,} \\ \frac{E}{1-\nu^2} & \text{for plane strain,} \end{cases} \tag{1.6}$$

E is the Young's modulus, and ν is Poisson's ratio.

In general, although we know that stiffer materials may have very high toughness like metals or very low toughness like ceramics, we often assume that more compliant materials will have a lower toughness. However, due to their chemistry and microstructures, biological, polymeric, and composite materials may not follow this trend. For example, hydrogels that have been toughened by double networking exhibit fracture energies comparable to much stiffer plastics while retaining most of the extreme compliance of a gel. On the other hand, conventional hydrogels are extremely compliant and exhibit fracture energies comparable to glasses and ceramics [34, 35].

In this thesis, fracture energy is used to describe the resistance of a conventional polymer hydrogel to fracture due to the nature of its networked microstructure.

Granular mechanics

A granular material is like a high volume fraction particle reinforced material where the matrix is infinitely compliant (zero stiffness). When there is no matrix, the particles directly contact each other. The particle motion is also significantly less constrained; they can now rotate and slide against each other. This leads to the unique ability of granular materials to behave like both solids and liquids [61, 66, 67, 77].

In many civil engineering applications engineers design granular materials to behave as solids and liquid-like flow is considered as a failure mode. Here, the majority of theories and design equations treat the granular material as a continuum. In industrial processes like commercial grain and pharmaceutical processing, engineers want these materials to behave as fluids and flow through equipment like hoppers. Here also, the granular material is often treated as a continuum in models and design equations. However, all these models and equations are specific to a certain geometry and loading condition. There is no universal continuum model that can describe a granular materials solid-like and fluid-like behaviors and the transition between them [77, 78].

Over the last few decades significant work has been done to improve our understanding of granular mechanics by considering grains as discrete particles. Several experimental techniques have been used to demonstrate how continuum level loads are carried via interparticle force chains in granular assemblies. Force chains are described as sets of particles in an assembly that carry large compressive loads while other particles near by experience much lower loads [68, 69, 79, 80]. Graphically, this concept is demonstrated in Fig. 1.5. The load applied to the upper boundary is carried primarily by two force chain branches that meet and transfer the load to the lower boundary. When the load exceeds a critical limit, force chains break and reconfigure. When the chains break, the particles are free to move relative to each other and can therefore flow. When flow happens in a narrow band through a granular specimen is is known as shear band failure, which is a very common mechanism of failure in granular structures [63, 69].

Fully three dimensional experiments on shear band formation and slip in granular materials are very challenging for several reasons. First, specimens ideally consist of many thousands of particles, making both analysis and modeling highly computationally expensive. Second, measuring the interparticle forces requires the abililty to measure or image all the particles *in-situ*. This can be very expensive and time consuming. Additionally, many available imaging methods have strict limitations on materials, geometries, and time-scales that significantly impact experimental capabilities [62, 64, 81, 82].

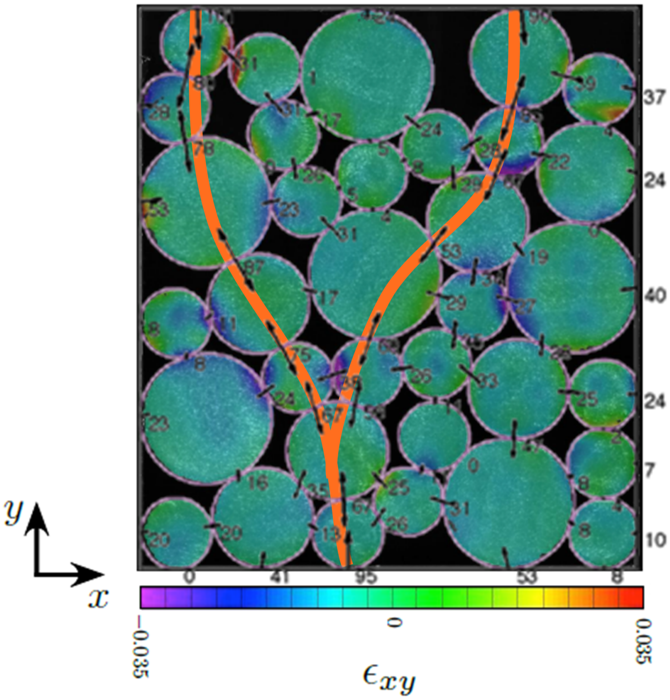

Figure 1.5: Particle level force chains carry a continuum level compressive load through a granular specimen. Adapted from Hurley et al. (2014) with permission from Elsevier [68].

1.4 Quantitative Visualization

To advance both granular mechanics and fracture mechanics theories, we need to expand experimental capabilities to be able to understand grain-level and micro-structural-level effects in a fully three-dimensional sense. Computational power for modeling, imaging, and analysis has greatly increased in recent years making these experiments and analyses more achievable than ever before [64, 83, 84].

Installing hundreds of thousands of minuscule strain gages or load cells on each particle in a granular specimen or distributed throughout a fracture specimen is not only impractical, it also affects the behavior of the specimens themselves. For this reason, volumetric imaging methods combined with quantitative analyses are becoming increasingly popular [85–88]. These methods are also being employed to improve modeling capabilities for complex geometries [12, 22, 89].

Volumetric imaging methods

Many volumetric imaging technologies are available, each with their own unique capabilities and challenges.

Diffraction methods such as neutron diffraction and X-ray diffraction (XRD) use interactions between the beam and the nucleus and electron clouds of atoms respectively to "image" specimens. In both of theses methods, average strain in crystallographic materials can be measured by determining the change in atomic spacing as a result of loading [4, 5, 12, 63, 67, 90, 91].

Tomographic scanning of a specimen can be used to build a 3D image of the geometry and grain structure. When X-rays are used with tomographic scanning it is commonly called micro-computed tomography (µCT.) This method is often used in the medical industry to image a patient's internal organs but it is also used in the aerospace and automotive industries for non-destructive assessment and inspection of parts and assemblies for damage and defects. More recently, it has been used for understanding mechanics and fracture inside opaque materials [62, 64, 70, 83, 84].

While these methods can provide excellent resolution both spatially and for measuring strains, they are very expensive and often highly time consuming. The diffraction methods also necessitate a material with a crystal structure in order to be able to measure grain strains via changes in atomic spacing. Tomographic image reconstruction is very challenging and can result in errors due to imaging artifacts [90, 92, 93].

Confocal Microscopy

Confocal microscopy is an optical volumetric imaging method that is much less expensive and less time consuming than the methods described above. As with any experimental method, it also has its own unique limitations among its many benefits.

The word "confocal" means having a common focus. This concept is illustrated in Fig. 1.6 for a transmission confocal microscope set up. The black lines show light that goes through the upper pinhole, is focused at the focal plane, and then transmitted through the lower pinhole to be captured by the detector. The dashed red lines show light that is not in the focal plane and is therefore not transmitted through the pinhole and captured by the detector. Most confocal microscopy systems capture reflected or emitted light rather than transmitted so incorporate a beam splitter to redirect the reflected or emitted light to the detector [94–97]. Commonly, this light is in the visible spectrum but it is also possible to use ultraviolet and infrared wavelengths just outside of the visible spectrum.

Simple raster scanning allows for capture of a 2D planar image. Volumetric images are typically captured as stacks of these 2D plane images by moving the microscope stage up or down in the vertical-direction.

Some confocal systems use photomultiplier tubes (PMTs) to capture the light intensity of individual voxels. When multiple PMTs are used, different light wavelength ranges can be captured separately allowing for identification and separation of different features in a specimen. Swept field and spinning disc systems usually use a CCD or CMOS camera and are typically faster because they capture several voxels or a line of voxels at once. While this does introduce some noise from spurious light reflections from adjacent pixels, it can exponentially increase scanning speeds. Additionally, CCD or CMOS camera cannot inherently filter different wavelengths of light so filters may need to be used in some applications [94, 95].

In most cases, lasers and fluorescent dyes or particles are used in confocal microscopy imaging. The laser excites the fluorescent molecules using a wavelength close to the peak excitation and the molecule then emits a photon at a lower wavelength known as the peak emission wavelength. The intensity of this emission is captured by the PMT or camera [94, 95].

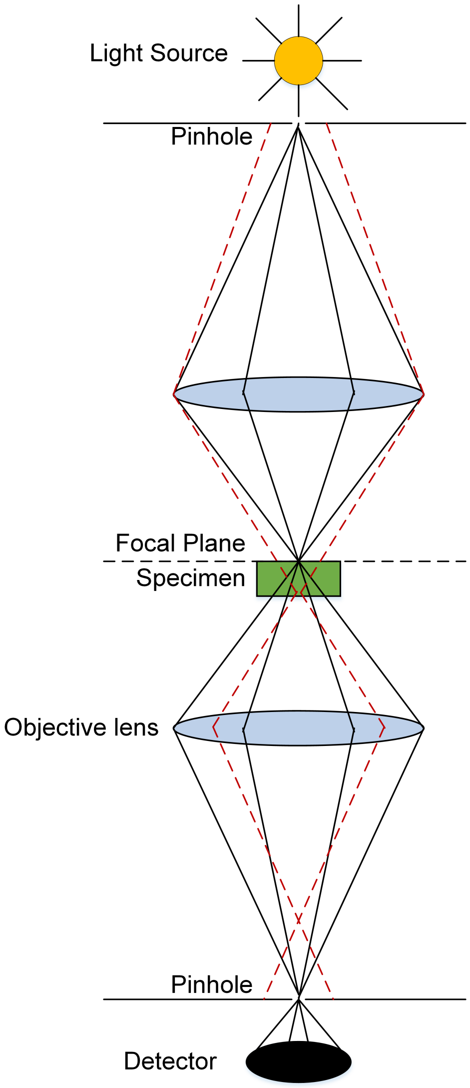

Figure 1.6: Illustration of the transmission confocal microscope concept where the black lines of light are in the focal "point" and the dashed red lines are out of focus and therefore not captured.

Confocal microscopy is commonly used in biological applications where different fluorescent dyes can be functionalized to bind to different components of cells. This allows biologists to differentiate parts of the cell such as the cell wall and nucleus, or to understand the structure produced by different proteins that make up the organelles [98].

Some researchers are using confocal microscopy to study how cells move, communicate, and respond to stimuli in 3D by measuring the deformations of a gel substrate around the cell. This is achieved by casting fluorescent microspheres into the gel and using these as tracking particles or as speckles for image correlation type methods [97, 99–104]. This suggests that a similar method could be used to study the mechanics of the polymer material itself in 3D [85]. It also motivates considering the wealth of geometries and loading conditions that could be studied [105–107].

One of the primary limitations of confocal microscopy is that in order to capture volumetric images, the material must have good optical transparency. Spatial resolution and optical constraints also limit the size of specimens and the imaging window. While this method is significantly faster than diffraction and tomography methods, raster scanning is still relatively slow compared to many material mechanical processes such as crack propagation.

Image correlation methods

In studying the mechanics of materials, several quantities need to be calculated or measured. A common way to measure full-field deformations is by using image correlation methods such as digital image correlation (DIC). A random pattern, often speckles, acts as a unique identifier for subsets of the image. Each subset in a reference image is matched to a subset in the deformed image by finding the closest pattern match using a cross-correlation coefficient. Displacements are then calculated for each subset and strains can be calculated from these deformations [108]. Then, knowing material properties allows for calculation of stresses. When boundary conditions and loading are well defined, material properties can be inferred from the deformation and strain results.

3D-DIC typically refers to the use of a multi-camera system to determine out-of-plane deformations. Digital volume correlation (DVC) extends the idea of DIC to volumetric space to determine the full 3D displacements and strains in a material. Most algorithms match subsets by allowing them to have both free-body motion and to deform but only measure the displacements directly [108, 109]. Strains are typically determined by computing the deformation gradient from the displacements.

In materials with discontinuities such as a crack or a granular assembly, care must be taken when applying image correlation methods. The discontinuity allows for large relative motions of the material on either side of a crack or between particles which artificially impact both displacement and strain measures. For fracture experiments, regions of interest (ROI) are commonly defined to exclude the final crack geometry [42–45]. For granular specimens, it is generally necessary to define an ROI for each particle individually [68, 110].

In addition to correlation methods, images can be used to measure geometric quantities such as particle shapes and areas in the case of granular materials. These parameters also allow for determining particle contacts and when combined with average strains determined using a correlation method become the inputs for the granular element method (GEM), an inverse solution method to determine interparticle forces [63, 68, 81, 110].

Granular element method

The granular element method (GEM) uses the discrete element method (DEM) as a basis and incorporates a contact law for interparticle friction. The formulation includes balance of forces and moments, $\mathbf{K_{eq}f} = \mathbf{0}$, the average stress in each particle, $\mathbf{K_{st}f} = \mathbf{b_{st}}$ where $\mathbf{b_{st}}^p = \Omega^p \boldsymbol{\sigma}^p$, and friction constraint equations, $\mathbf{Bf} \geq \mathbf{0}$. The inverse problem is solved as a minimization subject to constraints as in Eq. 1.7 as follows:

$$\mathbf{f} = \underset{\mathbf{f},\ \mathbf{Bf} \geq \mathbf{0}}{\arg\min} (\lambda ||\mathbf{K}_{eq}\mathbf{f}|| + (1 - \lambda)||\mathbf{K}_{st}\mathbf{f} - \mathbf{b}_{st}||), \tag{1.7}$$

where the preferred solution is determined by the knee point of the curve ($||\mathbf{K}_{eq}\mathbf{f}||$, $||\mathbf{K}_{st}\mathbf{f} - \mathbf{b}_{st}||$.) The full formulation of GEM can be found in the following references: [64, 68, 81, 82, 110, 111].

Applying GEM to experiments allows for determination of interparticle forces which can be used to understand force chains and how a granular material carries load. Images are used to extract geometric descriptors known as the granular fabric and correlation methods with a constitutive model for the particle's material are used to determine average particle stresses.

1.5 Outline

Chapter 1 presented the motivation for the research described in the thesis followed by a summary of the background, theories, and experimental methods used throughout. The rest of the thesis is organized into two primary chapters describing the experiments, results, and conclusions of work on both fracture mechanics and granular mechanics using 3D quantitative visualization techniques.

Chapter 2 describes work on understanding fracture processes in hydrogels. Slow stable crack propagation is achieved using fluid pressure in thin soft polymer gel specimens. Confocal microscopy is used to capture 2D internal plane fluorescent speckle images during propagation events and 3D volumetric images are captured before propagation and after crack arrest. Analysis of fracture energy shows that higher energy is needed to renucleate a crack after it arrests. Based on assessment of these renucleation events and on through thickness variation in crack shape, toughening mechanisms are suggested as contributors to the slow crack surface roughening observed by other researchers. Further experiments to better understand these effects are suggested. This experimental method is also recommended to improve understanding of interface and inclusion toughening effects.

Chapter 3 describes several aspects of conducting intergranular force transmission experiments using confocal microscopy imaging techniques. Commercially available fluorescently marked polymer spheres are considered as a potential model granular material. While the speckle pattern is excellent for image correlation techniques and the particle size is good for the scale of confocal microscopy imaging, the particles' optical properties are not appropriate for this imaging method. A method to produce custom in-house manufactured spheres with a volumetric speckle pattern that could be easily imaged using a confocal microscope is also presented. Imaging and DVC capabilities for a large gel sphere are then presented and suggest that many new granular experiments can be conducted using these particles with the described experimental technique.

These results are further summarized in Chapter 4 and several new research directions are presented based on the experimental capabilities described in the previous chapters.

REFERENCES

[1] W. T. Read. *Dislocations in crystals*. McGraw-Hill, 1953.

[2] J. P. Hirth, J. Lothe, and T. Mura. Theory of dislocations (2nd ed.). *Journal of Applied Mechanics*, 50(2):476–477, June 1983. ISSN 0021-8936. doi: 10.1115/1.3167075.

[3] A. N. Stroh. The cleavage of metal single crystals. *The Philosophical Magazine: A Journal of Theoretical Experimental and Applied Physics*, 3(30): 597–606, 1958. doi: 10.1080/14786435808565802.

[4] J. Oddershede, S. Schmidt, H. F. Poulsen, L. Margulies, J. Wright, M. Moscicki, W. Reimers, and G. Winther. Grain-resolved elastic strains in deformed copper measured by three-dimensional X-ray diffraction. *Materials Characterization*, 62(7):651–660, 2011. ISSN 1044-5803. doi: 10.1016/j.matchar.2011.04.020.

[5] U. Lienert, T. S. Han, J. Almer, P. R. Dawson, T. Leffers, L. Margulies, S. F. Nielsen, H. F. Poulsen, and S. Schmidt. Investigating the effect of grain interaction during plastic deformation of copper. *Acta Materialia*, 52(15): 4461–4467, 2004. ISSN 1359-6454. doi: 10.1016/j.actamat.2004.05.051.

[6] J. Marrow, C. Reinhard, Y. Vertyagina, L. Saucedo-Mora, D. Collins, and M. Mostafavi. 3D studies of damage by combined X-ray tomography and digital volume correlation. *Procedia Materials Science*, 3:1554–1559, 2014. ISSN 2211-8128. doi: 10.1016/j.mspro.2014.06.251.

[7] F. Baldi, F. Bignotti, I. Peroni, S. Agnelli, and T. Riccò. On the measurement of the fracture resistance of polyacrylamide hydrogels by wire cutting tests. *Polymer Testing*, 31(3):455–465, 2012. ISSN 0142-9418. doi: 10.1016/j.polymertesting.2012.01.009.

[8] J. P. Gong and Y. Osada. Soft and wet materials: From hydrogels to biotissues. In M. Cloitre, editor, *High Solid Dispersions*, pages 203–246. Springer Berlin Heidelberg, Berlin, Heidelberg, 2010. ISBN 978-3-642-16382-1. doi: 10.1007/12_2010_91.

[9] R. Long and C.-Y. Hui. Fracture toughness of hydrogels: measurement and interpretation. *Soft Matter*, 12(39):8069–8086, 2016. ISSN 1744-683X. doi: 10.1039/C6SM01694D.

[10] K. Madi, G. Tozzi, Q. H. Zhang, J. Tong, A. Cossey, A. Au, D. Hollis, and F. Hild. Computation of full-field displacements in a scaffold implant using digital volume correlation and finite element analysis. *Medical Engineering & Physics*, 35(9):1298–1312, 2013. ISSN 1350-4533. doi: 10.1016/j.medengphy.2013.02.001.

[11] R. B. Miller. Chapter 2 - Structure of wood. In *Wood handbook—Wood as an engineering material. General Technical Report FPL–GTR–113*. U.S. Department of Agriculture, Forest Service, Forest Products Laboratory, Madison, WI, 1999. ISBN 978-0-88415-474-7. doi: https://doi.org/10.2737/FPL-GTR-113.

[12] O. K. Mahabadi, B. S. A. Tatone, and G. Grasselli. Influence of microscale heterogeneity and microstructure on the tensile behavior of crystalline rocks. *Journal of Geophysical Research: Solid Earth*, 119(7):5324–5341, 2014. ISSN 2169-9356. doi: 10.1002/2014JB011064.

[13] R. M. Jones. *Mechanics of composite materials, 2nd Ed.* Taylor & Francis, Philadelphia, Penn, 1999. ISBN 156032712X.

[14] G. Odian. *Principles of Polymerization*. Wiley InterScience electronic collection. Wiley, 2004. ISBN 978-0-471-47874-4.

[15] T. A. Berfield, J. K. Patel, R. G. Shimmin, P. V. Braun, J. Lambros, and N. R. Sottos. Micro- and nanoscale deformation measurement of surface and internal planes via digital image correlation. *Experimental Mechanics*, 47 (1):51–62, 2007. ISSN 0014-4851. doi: 10.1007/s11340-006-0531-2.

[16] J. Lachambre, J. Réthoré, A. Weck, and J.-Y. Buffiere. Extraction of stress intensity factors for 3d small fatigue cracks using digital volume correlation and X-ray tomography. *International Journal of Fatigue*, 71:3–10, 2014. ISSN 0142-1123. doi: 10.1016/j.ijfatigue.2014.03.022.

[17] J. Lachambre, A. Weck, J. Réthoré, J.-Y. Buffière, and J. Adrien. 3D analysis of a fatigue crack in cast iron using digital volume correlation of X-ray tomographic images. In H. Jin, C. Sciammarella, C. Furlong, and S. Yoshida, editors, *Imaging Methods for Novel Materials and Challenging Applications, Volume 3: Proceedings of the 2012 Annual Conference on Experimental and Applied Mechanics*, pages 203–209. Springer New York, New York, NY, 2013. ISBN 978-1-4614-4235-6. doi: 10.1007/978-1-4614-4235-6_28.

[18] N. Limodin, J. Réthoré, J.-Y. Buffière, A. Gravouil, F. Hild, and S. Roux. Crack closure and stress intensity factor measurements in nodular graphite cast iron using three-dimensional correlation of laboratory X-ray microtomography images. *Acta Materialia*, 57(14):4090–4101, 2009. ISSN 1359-6454. doi: 10.1016/j.actamat.2009.05.005.

[19] N. Limodin, J. Réthoré, J.-Y. Buffière, F. Hild, S. Roux, W. Ludwig, J. Rannou, and A. Gravouil. Influence of closure on the 3d propagation of fatigue cracks in a nodular cast iron investigated by X-ray tomography and 3d volume correlation. *Acta Materialia*, 58(8):2957–2967, 2010. ISSN 1359-6454. doi: 10.1016/j.actamat.2010.01.024.

[20] M. Mostafavi, N. Baimpas, E. Tarleton, R. C. Atwood, S. A. McDonald, A. M. Korsunsky, and T. J. Marrow. Three-dimensional crack observation, quantification and simulation in a quasi-brittle material. *Acta Materialia*, 61 (16):6276–6289, 2013. ISSN 1359-6454. doi: 10.1016/j.actamat.2013.07.011.

[21] M. Mostafavi, S. A. McDonald, P. M. Mummery, and T. J. Marrow. Observation and quantification of three-dimensional crack propagation in polygranular graphite. *Engineering Fracture Mechanics*, 110:410–420, 2012. ISSN 0013-7944. doi: 10.1016/j.engfracmech.2012.11.023.

[22] J. Rannou, N. Limodin, J. Réthoré, A. Gravouil, W. Ludwig, M.-C. Baïetto-Dubourg, J.-Y. Buffière, A. Combescure, F. Hild, and S. Roux. Three dimensional experimental and numerical multiscale analysis of a fatigue crack. *Computer Methods in Applied Mechanics and Engineering*, 199(21–22): 1307–1325, 2009. ISSN 0045-7825. doi: 10.1016/j.cma.2009.09.013.

[23] Y. Tanaka, K. Fukao, Y. Miyamoto, and K. Sekimoto. Discontinuous crack fronts of three-dimensional fractures. *EPL (Europhysics Letters)*, 43(6):664, 1998. ISSN 0295-5075.

[24] E. M. Ahmed. Hydrogel: Preparation, characterization, and applications: A review. *Journal of Advanced Research*, 6(2):105–121, 2013. ISSN 2090-1232. doi: 10.1016/j.jare.2013.07.006.

[25] N. Annabi, J. W. Nichol, X. Zhong, C. Ji, S. Koshy, A. Khademhosseini, and F. Dehghani. Controlling the porosity and microarchitecture of hydrogels for tissue engineering. *Tissue Engineering. Part B, Reviews*, 16(4):371–383, 2010. ISSN 1937-3368 1937-3376. doi: 10.1089/ten.teb.2009.0639.

[26] A. K. Denisin and B. L. Pruitt. Tuning the range of polyacrylamide gel stiffness for mechanobiology applications. *ACS Applied Materials & Interfaces*, 8(34): 21893–21902, 2016. ISSN 1944-8244. doi: 10.1021/acsami.5b09344.

[27] C. A. Grattoni, H. H. Al-Sharji, C. Yang, A. H. Muggeridge, and R. W. Zimmerman. Rheology and permeability of crosslinked polyacrylamide gel. *Journal of Colloid and Interface Science*, 240(2):601–607, 2001. ISSN 0021-9797. doi: 10.1006/jcis.2001.7633.

[28] S. Kiatkamjornwong and P. Phunchareon. Influence of reaction parameters on water absorption of neutralized poly(acrylic acid-co-acrylamide) synthesized by inverse suspension polymerization. *Journal of Applied Polymer Science*, 72(10):1349–1366, 1999. ISSN 1097-4628. doi: 10.1002/(SICI)1097-4628(19990606)72:10<1349::AID-APP16>3.0.CO;2-K.

[29] S. K. Patel, F. Rodriguez, and C. Cohen. Mechanical and swelling properties of polyacrylamide gel spheres. *Polymer*, 30(12):2198–2203, 1989. ISSN 0032-3861. doi: 10.1016/0032-3861(89)90249-8.

[30] T. Bertrand, J. Peixinho, S. Mukhopadhyay, and C. W. MacMinn. Dynamics of swelling and drying in a spherical gel. *Physical Review Applied*, 6(6), 2016. doi: 10.1103/PhysRevApplied.6.064010.

[31] T. R. C. Boyde. Swelling and contraction of polyacrylamide gel slabs in aqueous solutions. *Journal of Chromatography A*, 124(2):219–230, 1976. ISSN 0021-9673. doi: 10.1016/S0021-9673(00)89737-X.

[32] R. Brighenti, A. Spagnoli, A. Carpinteri, and F. Artoni. Notch effect in highly deformable material sheets. *Thin-Walled Structures*, 105(Supplement C):90–100, 2016. ISSN 0263-8231. doi: 10.1016/j.tws.2016.03.030.

[33] A. Grillet. Polymer gel rheology and adhesion. In N. Wyatt, L. Gloe, and J. De Vicente, editors, *Rheology*, page Ch. 3. InTech, Rijeka, 2012. doi: 10.5772/36975.

[34] S. Naficy, H. R. Brown, J. M. Razal, G. M. Spinks, and P. G. Whitten. Progress toward robust polymer hydrogels. *Australian Journal of Chemistry*, 64(8):1007–1025, 2011.

[35] S. Agnelli, F. Baldi, F. Bignotti, A. Salvadori, and I. Peroni. Fracture characterization of hyperelastic polyacrylamide hydrogels. *Engineering Fracture Mechanics*, 2018. ISSN 0013-7944. doi: 10.1016/j.engfracmech.2018.06.004.

[36] M. V. Swain, J. C. Metras, and C. G. Guillemet. XIIth international congress on glass: A deformation and fracture mechanics approach to the scoring and breaking of glass. *Journal of Non-Crystalline Solids*, 38:445–450, 1980. ISSN 0022-3093. doi: 10.1016/0022-3093(80)90459-7.

[37] E. Bouchbinder and T. Goldman and J. Fineberg. The dynamics of rapid fracture: instabilities, nonlinearities and length scales. *Reports on Progress in Physics*, 77(4):046501, 2014. ISSN 0034-4885.

[38] T. Baumberger, C. Caroli, D. Martina, and O. Ronsin. Magic angles and cross-hatching instability in hydrogel fracture. *Physical Review Letters*, 100 (17):178303, 2008. doi: 10.1103/PhysRevLett.100.178303.

[39] I. Einav, G. T. Houlsby, and G. D. Nguyen. Coupled damage and plasticity models derived from energy and dissipation potentials. *International Journal of Solids and Structures*, 44(7–8):2487–2508, 2006. ISSN 0020-7683. doi: 10.1016/j.ijsolstr.2006.07.019.

[40] F. Nilsson. A tentative method for determination of cohesive zone properties in soft materials. *International Journal of Fracture*, 136(1):133–142, 2005. ISSN 1573-2673. doi: 10.1007/s10704-005-5125-y.

[41] T. Brenner, S. Matsukawa, K. Nishinari, and R. Johannsson. Failure in a soft gel: Delayed failure and the dynamic yield stress. *Journal of Non-Newtonian Fluid Mechanics*, 196:1–7, 2012. ISSN 0377-0257. doi: 10.1016/j.jnnfm.2012.12.011.

[42] J. Réthoré, F. Hild, and S. Roux. Extended digital image correlation with crack shape optimization. *International Journal for Numerical Methods in Engineering*, 73(2):248–272, 2008. ISSN 1097-0207. doi: 10.1002/nme.2070.

[43] J. Réthoré, S. Roux, and F. Hild. An extended and integrated digital image correlation technique applied to the analysis of fractured samples. *European Journal of Computational Mechanics*, 18(3-4):285–306, 2009. ISSN 1779-7179. doi: 10.3166/ejcm.18.285-306.

[44] J. Réthoré, S. Roux, and F. Hild. Optimal and noise-robust extraction of fracture mechanics parameters from kinematic measurements. *Engineering Fracture Mechanics*, 78(9):1827–1845, 2011. ISSN 0013-7944. doi: 10.1016/j.engfracmech.2011.01.012.

[45] S. Roux, J. Réthoré, and F. Hild. Digital image correlation and fracture: an advanced technique for estimating stress intensity factors of 2d and 3d cracks. *Journal of Physics D: Applied Physics*, 42(21):214004, 2009. ISSN 0022-3727.

[46] L. Avellar, T. Reese, K. Bhattacharya, and G. Ravichandran. Effect of cohesive zone size on peeling of heterogeneous adhesive tape. *Journal of Applied Mechanics*, 85(12):121005–121005–7, 2018. ISSN 0021-8936. doi: 10.1115/1.4041224.

[47] S. Xia, L. Ponson, G. Ravichandran, and K. Bhattacharya. Toughening and asymmetry in peeling of heterogeneous adhesives. *Physical Review Letters*, 108(19):196101, 2012.

[48] S. M. Xia, L. Ponson, G. Ravichandran, and K. Bhattacharya. Adhesion of heterogeneous thin films—I: Elastic heterogeneity. *Journal of the Mechanics and Physics of Solids*, 61(3):838–851, 2013. ISSN 0022-5096. doi: 10.1016/j.jmps.2012.10.014.

[49] C.-J. Hsueh, L. Avellar, B. Bourdin, G. Ravichandran, and K. Bhattacharya. Stress fluctuation, crack renucleation and toughening in layered materials. *Journal of the Mechanics and Physics of Solids*, 120:68 – 78, 2018. ISSN 0022-5096. doi: https://doi.org/10.1016/j.jmps.2018.04.011.

[50] N. Wang and S. Xia. Cohesive fracture of elastically heterogeneous materials: An integrative modeling and experimental study. *Journal of the Mechanics and Physics of Solids*, 98:87–105, 2016. ISSN 0022-5096. doi: 10.1016/j.jmps.2016.09.004.

[51] L. T. Avellar. *Observations of Failure Phenomena in Periodic Media*. Dissertation (Ph.D.), California Institute of Technology, 2018.

[52] M. L. Cooke and D. D. Pollard. Fracture propagation paths under mixed mode loading within rectangular blocks of polymethyl methacrylate. *Journal of Geophysical Research: Solid Earth*, 101(B2):3387–3400, 1996. ISSN 2156-2202. doi: 10.1029/95JB02507.

[53] S. Y. Wang, S. W. Sloan, D. C. Sheng, and C. A. Tang. 3d numerical analysis of crack propagation of heterogeneous notched rock under uniaxial tension. *Tectonophysics*, 677–678:45–67, 2016. ISSN 0040-1951. doi: 10.1016/j.tecto.2016.03.042.

[54] J. Zuo, X. Deng, M. A. Sutton, and C.-S. Cheng. Three-dimensional crack growth in ductile materials: Effect of stress constraint on crack tunneling. *Journal of Pressure Vessel Technology*, 130(3):031401–031401–8, 2008. ISSN 0094-9930. doi: 10.1115/1.2937738.

[55] A. F. Bower and M. Ortiz. Solution of three-dimensional crack problems by a finite perturbation method. *Journal of the Mechanics and Physics of Solids*, 38 (4):443–480, 1990. ISSN 0022-5096. doi: 10.1016/0022-5096(90)90008-R.

[56] E. N. Brown, N. R. Sottos, and S. R. White. Fracture testing of a self-healing polymer composite. *Experimental Mechanics*, 42(4):372–379, 2002. ISSN 1741-2765. doi: 10.1007/bf02412141.

[57] H. Gao and J. R. Rice. A first-order perturbation analysis of crack trapping by arrays of obstacles. *Journal of Applied Mechanics*, 56(4):828–836, 1989. ISSN 0021-8936. doi: 10.1115/1.3176178.

[58] H. Gao. A boundary perturbation analysis for elastic inclusions and interfaces. *International Journal of Solids and Structures*, 28(6):703–725, 1991. ISSN 0020-7683. doi: 10.1016/0020-7683(91)90151-5.

[59] J. W. Hutchinson. Mechanisms of toughening in ceramics. In *Theoretical and Applied Mechanics*, pages 139–144. Elsevier, Amsterdam, 1989. ISBN 978-0-444-87302-6. doi: 10.1016/B978-0-444-87302-6.50017-X.

[60] J. J. Reinosa, A. del Campo, and J. F. Fernández. Indirect measurement of stress distribution in quartz particles embedded in a glass matrix by using confocal Raman microscopy. *Ceramics International*, 41(10, Part A):13598–13606, 2015. ISSN 0272-8842. doi: 10.1016/j.ceramint.2015.07.155.

[61] A. Drescher and G. de Josselin de Jong. Photoelastic verification of a mechanical model for the flow of a granular material. *Journal of the Mechanics and Physics of Solids*, 20(5):337–340, 1972. ISSN 0022-5096. doi: 10.1016/0022-5096(72)90029-4.

[62] S. A. Hall, M. Bornert, J. Desrues, Y. Pannier, N. Lenoir, G. Viggiani, and P. Besuelle. Discrete and continuum analysis of localised deformation in sand using X-ray μCT and volumetric digital image correlation. *Géotechnique*, 60:315–322, 2010.

[63] S. A. Hall, J. Desrues, G. Viggiani, P. Bésuelle, and E. Andò. Experimental characterisation of (localised) deformation phenomena in granular geomaterials from sample down to inter-and intra-grain scales. *Procedia IUTAM*, 4: 54–65, 2012. ISSN 2210-9838. doi: 10.1016/j.piutam.2012.05.007.

[64] R. C. Hurley, S. A. Hall, J. E. Andrade, and J. Wright. Quantifying interparticle forces and heterogeneity in 3D granular materials. *Physical Review Letters*, 117(9):098005, 2016.

[65] D. Muir Wood and D. Leśniewska. Stresses in granular materials. *Granular Matter*, 13(4):395–415, 2011. ISSN 1434-5021. doi: 10.1007/s10035-010-0237-0.

[66] F. Radjai, D. E. Wolf, M. Jean, and J.-J. Moreau. Bimodal character of stress transmission in granular packings. *Physical Review Letters*, 80(1):61–64, 1998.

[67] S. A. Hall, J. Wright, T. Pirling, E. Andò, D. J. Hughes, and G. Viggiani. Can intergranular force transmission be identified in sand? *Granular Matter*, 13 (3):251–254, 2011. ISSN 1434-5021. doi: 10.1007/s10035-011-0251-x.

[68] R. Hurley, E. Marteau, G. Ravichandran, and J. E. Andrade. Extracting inter-particle forces in opaque granular materials: Beyond photoelasticity. *Journal of the Mechanics and Physics of Solids*, 63(0):154–166, 2014. ISSN 0022-5096. doi: 10.1016/j.jmps.2013.09.013.

[69] A. Tordesillas and M. Muthuswamy. On the modeling of confined buckling of force chains. *Journal of the Mechanics and Physics of Solids*, 57(4):706–727, 2009. ISSN 0022-5096. doi: 10.1016/j.jmps.2009.01.005.

[70] I. Vlahinić, E. Andò, G. Viggiani, and J. E. Andrade. Towards a more accurate characterization of granular media: extracting quantitative descriptors from tomographic images. *Granular Matter*, 16(1):9–21, 2014. ISSN 1434-7636. doi: 10.1007/s10035-013-0460-6.

[71] A. F. Bower. *Applied Mechanics of Solids*. CRC Press, 2009. ISBN 978-1-4398-0248-9.

[72] T. L. Anderson. *Fracture Mechanics: Fundamentals and Applications, Third Edition*. CRC Press, 2005. ISBN 978-1-4200-5821-5.

[73] D. Broek. *Elementary engineering fracture mechanics*. Springer, Netherlands, 1 edition, 1982. ISBN 978-90-247-2580-9. doi: 10.1007/978-94-009-4333-9.

[74] J. W. Hutchinson. *A course on nonlinear fracture mechanics*. Dept. of Solid Mechanics, Technical University of Denmark, 1979.

[75] J. W. Hutchinson. *Micro-mechanics of damage in deformation and fracture*. Dept. of Solid Mechanics, Technical University of Denmark, 1987.

[76] A. A. Griffith and T. G. Ingram. VI. The phenomena of rupture and flow in solids. *Philosophical Transactions of the Royal Society of London. Series A, Containing Papers of a Mathematical or Physical Character*, 221(582-593): 163–198, 1921. doi: 10.1098/rsta.1921.0006.

[77] P. Jop, Y. Forterre, and O. Pouliquen. A constitutive law for dense granular flows. *Nature*, 441(7094):727–730, 2006. ISSN 0028-0836. doi: 10.1038/nature04801.

[78] H. P. Zhu, Z. Y. Zhou, R. Y. Yang, and A. B. Yu. Discrete particle simulation of particulate systems: A review of major applications and findings. *Chemical Engineering Science*, 63(23):5728–5770, 2008. ISSN 0009-2509. doi: 10.1016/j.ces.2008.08.006.

[79] N. Brodu, J. A. Dijksman, and R. P. Behringer. Spanning the scales of granular materials through microscopic force imaging. *Nat Commun*, 6, 2015. doi: 10.1038/ncomms7361.

[80] R. C. Hurley. *Force chains, friction, and flow: Behavior of granular media across length scales*. Dissertation (Ph.D.), California Institute of Technology, 2016.

[81] J. E. Andrade, K.-W. Lim, C. F. Avila, and I. Vlahinić. Granular element method for computational particle mechanics. *Computer Methods in Applied Mechanics and Engineering*, 241–244:262–274, 2012. ISSN 0045-7825. doi: 10.1016/j.cma.2012.06.012. URL `http://www.sciencedirect.com/science/article/pii/S0045782512002009`.

[82] K.-W. Lim and J. E. Andrade. Granular element method for three-dimensional discrete element calculations. *International Journal for Numerical and Analytical Methods in Geomechanics*, 38(2):167–188, 2014. ISSN 1096-9853. doi: 10.1002/nag.2203.

[83] S. Cottrino, Y. Jorand, E. Maire, and J. Adrien. Characterization by X-ray tomography of granulated alumina powder during in situ die compaction. *Materials Characterization*, 81:111–123, 2013. ISSN 1044-5803. doi: 10.1016/j.matchar.2013.04.004.

[84] F. Forsberg, R. Mooser, M. Arnold, E. Hack, and P. Wyss. 3d micro-scale deformations of wood in bending: Synchrotron radiation μCT data analyzed with digital volume correlation. *Journal of Structural Biology*, 164(3):255–262, 2008. ISSN 1047-8477. doi: 10.1016/j.jsb.2008.08.004.

[85] J. Y. Huang, X. C. Pan, S. S. Li, X. L. Peng, C. Y. Xiong, and J. Fang. A digital volume correlation technique for 3-D deformation measurements of soft gels. *International Journal of Applied Mechanics*, 3(2):335–354, 2011. ISSN 1758-8251. doi: 10.1142/s1758825111001019.

[86] A. I. Hussein, P. E. Barbone, and E. F. Morgan. Digital volume correlation for study of the mechanics of whole bones. *Procedia IUTAM*, 4:116–125, 2012. ISSN 2210-9838. doi: 10.1016/j.piutam.2012.05.013.

[87] M. Sjödahl, C. R. Siviour, and F. Forsberg. Digital volume correlation applied to compaction of granular materials. *Procedia IUTAM*, 4:179–195, 2012. ISSN 2210-9838. doi: 10.1016/j.piutam.2012.05.020.

[88] J. Réthoré, N. Limodin, J.-Y. Buffière, F. Hild, W. Ludwig, and S. Roux. Digital volume correlation analyses of synchrotron tomographic images. *The Journal of Strain Analysis for Engineering Design*, 46(7):683–695, 2011. ISSN 0309-3247. doi: 10.1177/0309324711409999.

[89] M. S. Wu. Strategies and challenges for the mechanical modeling of biological and bio-inspired materials. *Materials Science and Engineering: C*, 31(6): 1209–1220, 2010. ISSN 0928-4931. doi: 10.1016/j.msec.2010.11.012.

[90] L. Margulies, T. Lorentzen, H. F. Poulsen, and T. Leffers. Strain tensor development in a single grain in the bulk of a polycrystal under loading. *Acta Materialia*, 50(7):1771–1779, 2002. ISSN 1359-6454. doi: 10.1016/S1359-6454(02)00028-9.

[91] R. V. Martins, L. Margulies, S. Schmidt, H. F. Poulsen, and T. Leffers. Simultaneous measurement of the strain tensor of 10 individual grains embedded in an Al tensile sample. *Materials Science and Engineering: A*, 387–389: 84–88, 2004. ISSN 0921-5093. doi: 10.1016/j.msea.2004.02.069.

[92] H. Leclerc, S. Roux, and F. Hild. Projection savings in CT-based digital volume correlation. *Experimental Mechanics*, 55(1):275–287, 2014. ISSN 1741-2765. doi: 10.1007/s11340-014-9871-5.

[93] T. Taillandier-Thomas, S. Roux, T. F. Morgeneyer, and F. Hild. Localized strain field measurement on laminography data with mechanical regularization. *Nuclear Instruments and Methods in Physics Research Section B: Beam Interactions with Materials and Atoms*, 324:70–79, 2013. ISSN 0168-583X. doi: 10.1016/j.nimb.2013.09.033.

[94] D. M. Sheppard and C. R. J. Shotton. *Confocal Laser Scanning Microscopy*. Number 38 in Royal Microscopy Society Microscopy Handbooks. Springer-Verlag, New York, USA, 1997. ISBN 0-387-91514-1.

[95] T. Corle and G. Kino. *Confocal Scanning Optical Microscopy and Related Imaging Systems*. Academic Press, Burlington, 1996. ISBN 978-0-12-408750-7. doi: 10.1016/B978-012408750-7/50008-2.

[96] C. Franck. *Quantitative characterization of 3D deformations of cell interactions with soft biomaterials*. Dissertation (Ph.D.), California Institute of Technology, 2008.

[97] J. K. Notbohm. *Dynamics of cell–matrix mechanical interactions in three dimensions*. Dissertation (Ph.D.), California Institute of Technology, 2013.

[98] M. A. Hemphill, B. E. Dabiri, S. Gabriele, L. Kerscher, C. Franck, J. A. Goss, P. W. Alford, and K. K. Parker. A possible role for integrin signaling in diffuse axonal injury. *PLoS ONE*, 6(7):e22899, 2011. doi: 10.1371/journal.pone.0022899.

[99] C. Franck, S. A. Maskarinec, D. A. Tirrell, and G. Ravichandran. Three-dimensional traction force microscopy: A new tool for quantifying cell-matrix interactions. *PLoS ONE*, 6(3):e17833, 2011. doi: 10.1371/journal.pone.0017833.

[100] J. Y. Huang, X. L. Peng, L. Qin, T. Zhu, C. Y. Xiong, Y. Y. Zhang, and J. Fang. Determination of cellular tractions on elastic substrate based on an integral boussinesq solution. *Journal of Biomechanical Engineering-Transactions of the Asme*, 131(6):9, 2009. ISSN 0148-0731. doi: 10.1115/1.3118767.

[101] S. A. Maskarinec, C. Franck, D. A. Tirrell, and G. Ravichandran. Quantifying cellular traction forces in three dimensions. *Proceedings of the National Academy of Sciences*, 106(52):22108–22113, 2009. doi: 10.1073/pnas.0904565106.

[102] J. Notbohm, J. H. Kim, A. R. Asthagiri, and G. Ravichandran. Three-dimensional analysis of the effect of epidermal growth factor on cell-cell adhesion in epithelial cell clusters. *Biophysical Journal*, 102(6):1323–1330, 2012. ISSN 0006-3495. doi: 10.1016/j.bpj.2012.02.016.

[103] J. Notbohm, A. Lesman, D. A. Tirrell, and G. Ravichandran. Quantifying cell-induced matrix deformation in three dimensions based on imaging matrix fibers. *Integr. Biol.*, 7(10):1186–1195, 2015. doi: 10.1039/C5IB00013K.

[104] A. Lesman, J. Notbohm, D. A. Tirrell, and G. Ravichandran. Contractile forces regulate cell division in three-dimensional environments. *The Journal of Cell Biology*, 205(2):155–162, 2014. doi: 10.1083/jcb.201309029.

[105] J. T. Fredrich. 3d imaging of porous media using laser scanning confocal microscopy with application to microscale transport processes. *Physics and Chemistry of the Earth, Part A: Solid Earth and Geodesy*, 24(7):551–561, 1999. ISSN 1464-1895. doi: 10.1016/S1464-1895(99)00079-4.

[106] Q. Gao, C. Wang, H. Liu, C. Wang, X. Liu, and Z. Tong. Suspension polymerization based on inverse Pickering emulsion droplets for thermo-sensitive hybrid microcapsules with tunable supracolloidal structures. *Polymer*, 50(12):2587–2594, 2009. ISSN 0032-3861. doi: 10.1016/j.polymer.2009.03.049.

[107] E. Merson, V. Danilov, D. Merson, and A. Vinogradov. Confocal laser scanning microscopy: The technique for quantitative fractographic analysis. *Modern Imaging Techniques in Fracture and Damage Analyses*, 183(Supplement C):147–158, 2017. ISSN 0013-7944. doi: 10.1016/j.engfracmech.2017.04.026.

[108] J. Sutton, H. Schreier, and M. A. Orteu. *Image Correlation for Shape, Motion and Deformation Measurements: Basic Concepts, Theory and Applications*. Springer US, 1 edition, 2009. ISBN 978-0-387-78747-3. doi: 10.1007/978-0-387-78747-3.

[109] E. Bar-Kochba, J. Toyjanova, E. Andrews, K. S. Kim, and C. Franck. A fast iterative digital volume correlation algorithm for large deformations. *Experimental Mechanics*, 55(1):261–274, 2015. ISSN 0014-4851. doi: 10.1007/s11340-014-9874-2.

[110] E. Marteau and J. Andrade. A novel experimental device for investigating the multiscale behavior of granular materials under shear. *Granular Matter*, 19, 2017. doi: 10.1007/s10035-017-0766-x.

[111] R. C. Hurley, K. W. Lim, G. Ravichandran, and J. E. Andrade. Dynamic inter-particle force inference in granular materials: Method and application. *Experimental Mechanics*, 56(2):217–229, 2016. ISSN 1741-2765. doi: 10.1007/s11340-015-0063-8.

Chapter 2

CRACK PROPAGATION AND RENUCLEATION IN SOFT BRITTLE HYDROGELS

This Chapter is adapted from:

K. A. Mac Donald and G. Ravichandran. “Crack propagation and renucleation in soft brittle hydrogels”. 2019. *Submitted.*

Abstract

Crack tip opening displacement (CTOD) and fracture energy are determined from crack geometry and material properties for very slowly propagating cracks, less than 50 $\mu m/s$, in thin brittle hydrogels on the sub-millimeter scale. 2D fluorescent speckle images are captured using confocal microscopy during propagation, and 3D volumetric images are captured both before propagation begins and after the crack arrests. Fracture energy builds up until a critical value is reached and then remains constant as the crack propagates and eventually arrests when the energy is no longer sufficient for propagation. Once a crack arrests, more energy is needed for renucleation, suggesting that local toughening effects are at play. Based on observations of renucleation events and analysis of 3D crack shapes, this local toughening points to a mechanism for fracture surface roughening observed in the literature for slowly propagating cracks. Additionally, through-thickness variation in fracture energy, while expected from linear elastic fracture mechanics (LEFM) theory, suggests local toughening in the process zone which contributes to this roughening of crack surfaces.

Keywords: brittle, confocal microscopy, fracture mechanics, slow cracks, soft

2.1 Introduction

Pierre-Gilles de Gennes defines soft matter as "comprising all physiochemical systems which have *large response functions*"[1]. This includes many fluids but also includes solids such as gels and rubbers. These types of materials are becoming increasingly important as structural materials. Advances in robotics, wearable and implantable biomedical devices, and additive manufacturing have given rise to great interest in using such materials in load bearing applications [2, 3]. In soft robotics, gels and other soft materials are used to encase hard components so they feel more life-like. They are also used to build soft actuators to perform delicate tasks like picking up glasses or eggs and in realistic joints to minimize friction [4, 5]. In the field of biomedical devices one of the major challenges is producing functional, comfortable, and bio-compatible implants and devices. Many biological tissues are very compliant, so implants and devices with high stiffnesses are likely to cause significant inflammation, leading to scarring and rejection of the implant [6]. Advancements in additive manufacturing techniques have led to interest in printing customized scaffolds for cell growth. Nutrient transport through the scaffold is critical to be able to grow cells in complex geometries [7]. Additionally, it has been shown that substrate stiffness has a great effect on cell growth [8–10]. This suggests that in order to move toward printing viable simple organs, scaffolds must be compliant enough to allow proper growth of cells and tissues.

One of the major drawbacks of conventional synthetic soft materials is their low toughness. Since hydrogels are compliant, they can undergo large deformations but they also typically exhibit very brittle fracture. There are several methods that can be used to increase gel toughness such as double networking which can produce gels with mechanical and fracture responses comparable to biological tissues [5, 11, 12]. Hydrogels also show excellent potential for improving cardiac implants because they can be manufactured with stiffnesses as low as that of cardiac muscle, one of the most compliant yet toughest tissues in the human body.

In addition to their uses in biological applications, conventional hydrogels offer a unique opportunity to improve our understanding of fracture mechanics for both soft and brittle materials. The fracture toughness of conventional hydrogels is comparable to that of ceramics and glasses, but they undergo significantly larger and therefore measurable displacements within the linear elastic regime, making them good candidates for investigating fracture of brittle materials [13–16]. Further study of fracture in conventional gels will also provide insights into the mechanics of toughened gels.

Previous studies of fracture in soft brittle hydrogels have shown some unique behaviors. Of particular note are observations of crack surface roughening in slow crack propagation [2, 17, 18]. Macro-scale chevron shaped ridges in fractal-like patterns, sometimes called cross-hatch regions, have been observed on crack surfaces when propagation is very slow. These ridges seem to be the result of discontinuities in the crack front. At faster rates these ridges do not form but micro-scale generalized roughening is still observed. Another fracture behavior unique to soft hydrogels is fracturing as a result of contact stresses at the gel-water-air interface. Studies have been conducted examining the natural periodicity in formation of such cracks depending on gel thickness. It has been suggested that these cracks then propagate due to the hydrostatic pressure resulting from capillarity [19].

In this chapter we present an experimental method that allows us to measure fracture energy in a soft brittle hydrogel during slow crack propagation on the sub-millimeter scale. Fracture energy is measured using geometric analysis of the crack opening within the linear elastic fracture mechanics (LEFM) regime. Results show the expected characteristic increase in fracture energy followed by a plateau when the crack begins to propagate. Additionally, we visualize renucleation on the scale of the stress concentration near the crack tip and begin to probe the volumetric aspects of fracture by characterizing the crack shape and front. First, we describe the specimens and experimental considerations in Section 2.2. Then, we discuss in Section 2.3 the analysis methods used to measure stress concentration, crack propagation and renucleation, and crack shape. This is followed by a discussion of the results and findings of these 2D and 3D analyses in Section 2.4.

2.2 Materials and Methods

Specimens

A cross-linked polyacrylamide/bis-acrylamide copolymer (polyacrylamide) hydrogel is chosen as the material for this study because it is a well characterized polymer system that shows excellent optical transparency and has highly tunable mechanical properties. It also exhibits linear elastic response up to 10% strain. Once polymerized, polyacrylamide is highly inert and is used in many biological applications ranging from soft contact lenses to burn dressings. Gel stiffness and water content can be controlled by adjusting the cross-linker ratio and monomer concentration respectively. Fluorescent microspheres have been used successfully for confocal microscopy imaging and as speckles for image correlation in similar gels for several biomechanics studies [20–22].

For the fracture experiments, we use a relatively stiff hydrogel and polymerize it in an almost fully swelled state. Specimens are prepared from 1 ml monomer-cross-linker-initiator solutions in deionized water with fluorescent microspheres. The monomer to cross-linker ratio, C, is 5% and the monomer concentration, T, is

10.5%. The monomer-cross-linker-initiator solution is prepared using a 40% w/v solution of acrylamide and bis-acrylamide with a 19:1 monomer to cross-linker ratio (ACRYL/BIS™, AMRESCO®) and a 10% w/v solution of ammonium persulfate (APS, AMRESCO®) prepared from 150 mg tablets added to 1.5 ml deionized water. The APS solution can be stored under refrigeration for up to 7 days before preparing a fresh batch and provides free radicals to initiate polymerization. Red 2.0 μm carboxylate modified polystyrene FluoSpheres® (580 nm peak excitation, 605 nm peak emission, Molecular Probes™) in a 2% solids aqueous solution or green 0.72 μm polystyrene FluoroMax™microspheres (468 nm peak excitation, 508 nm peak emission, Thermo Scientific™) in a 1% solids aqueous solution are added prior to polymerization to produce a volumetric speckle pattern for image and correlation analyses. Once the gel is polymerized, these particles are fixed within it because they are sufficiently large compared to the gel pore size. To achieve an appropriate speckle density, 0.050 ml or 0.025 ml of each microsphere solution are used, respectively. The final solution is mixed gently to avoid introducing excess oxygen which inhibits the polymerization reaction. Just prior to casting, 0.002 ml of Tetramethylethylenediamine (TEMED, Alfa-Aesar®) is added as a catalyst and the solution is gently mixed again. Specimens are cast within 2 minutes to ensure the solution remains a liquid until it has been cast into the specimen's final shape. The polymerization reaction takes two to thirty minutes to complete, depending on ambient conditions and actual volume of catalyst used. A slightly higher ambient temperature can increase reaction speed significantly. Since TEMED is highly volatile and we use such a small volume, there is some uncertainty in the actual volume used and excess catalyst can greatly increase the reaction rate.

Rheological analysis was conducted on several polyacrylamide specimens to determine the prepared gel's mechanical properties. The Young's Modulus, E is approximately 78 kPa and the gel exhibits linear elastic behavior up to 10% strain with viscous effects over time scales on the order of hours to days. Since experiments are conducted on time scales on the order of minutes, we assume that viscoelastic effects are negligible in our experiments.

Experiment

Thin disk specimens are cast by micro-pipetting the monomer solution onto a 25 mm diameter No. 0 glass cover slip (100 μm ± 20 μm thick) and then dropping a second cover slip gently on top. This process is illustrated in Fig. 2.1. Since the monomer is water soluble and the solution has a high water content, surface

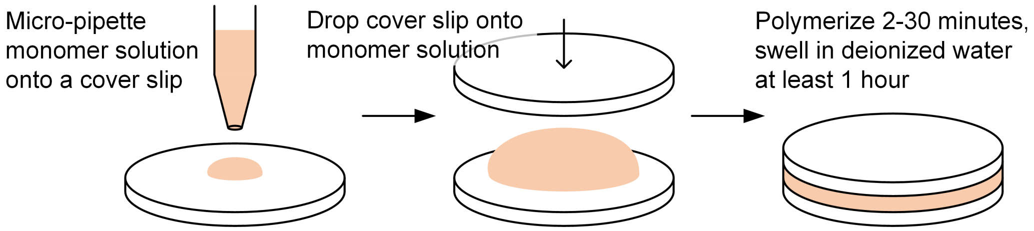

Figure 2.1: Procedure for casting thin polyacrylamide hydrogels between cover slips.

tension is sufficient to support the top cover slip and self align them producing very thin gels with even thicknesses. Typical specimens are about 400 to 700 μm thick where specimen thickness is controlled by the volume of solution pipetted onto the cover slip (0.2 ml to 0.33 ml). During polymerization specimens are kept covered to prevent excessive evaporation of water from the gel structure. Once polymerization is complete, specimens are allowed to soak in deionized water for at least one hour before testing and imaging to ensure that equilibrium swelling is reached. Experiments are conducted within five days of casting to minimize toughening or weakening effects that can occur due to swelling-deswelling cycles and gel aging. This also ensures that the gels remain lightly bonded to the cover slips, which are not removed during the experiments.

Fracture experiments are conducted with *in-situ* three-dimensional imaging via confocal microscopy. An initial crack is introduced by gently inserting a 28 gauge MicroFil blunt needle (350 μm OD, 250 μm ID, World Precision Instruments) between the cover slips and then pulling the needle partially out such that a crack forms ahead of the needle tip. The initial crack is held partially open by the needle. Then the specimen is pre-loaded in compression via a uniaxial compression device mounted to a standard microscope stage insert as shown in Fig. 2.2. A displacement controlled micrometer acts as the loading arm and is gently advanced until it feels just tight and the specimen is firmly held in place on the microscope stage. The compressive load was found to be necessary for stable crack growth and is discussed further in Section 2.3. Glycerol (Proteomics grade, AMRESCO®) is injected into the crack at a rate of 0.050 ml per minute using a micro-syringe pump (Model NE-1000, New Era Pump Systems, Inc.) until the crack begins to advance. The injection fluid, glycerol, was chosen for its incompressibility, high viscosity, and low toxicity. Since the fracture specimens are a hydrogel, water was not an appropriate injection fluid as it quickly dissipated into the gel. The high viscosity of the glycerol significantly reduced this.

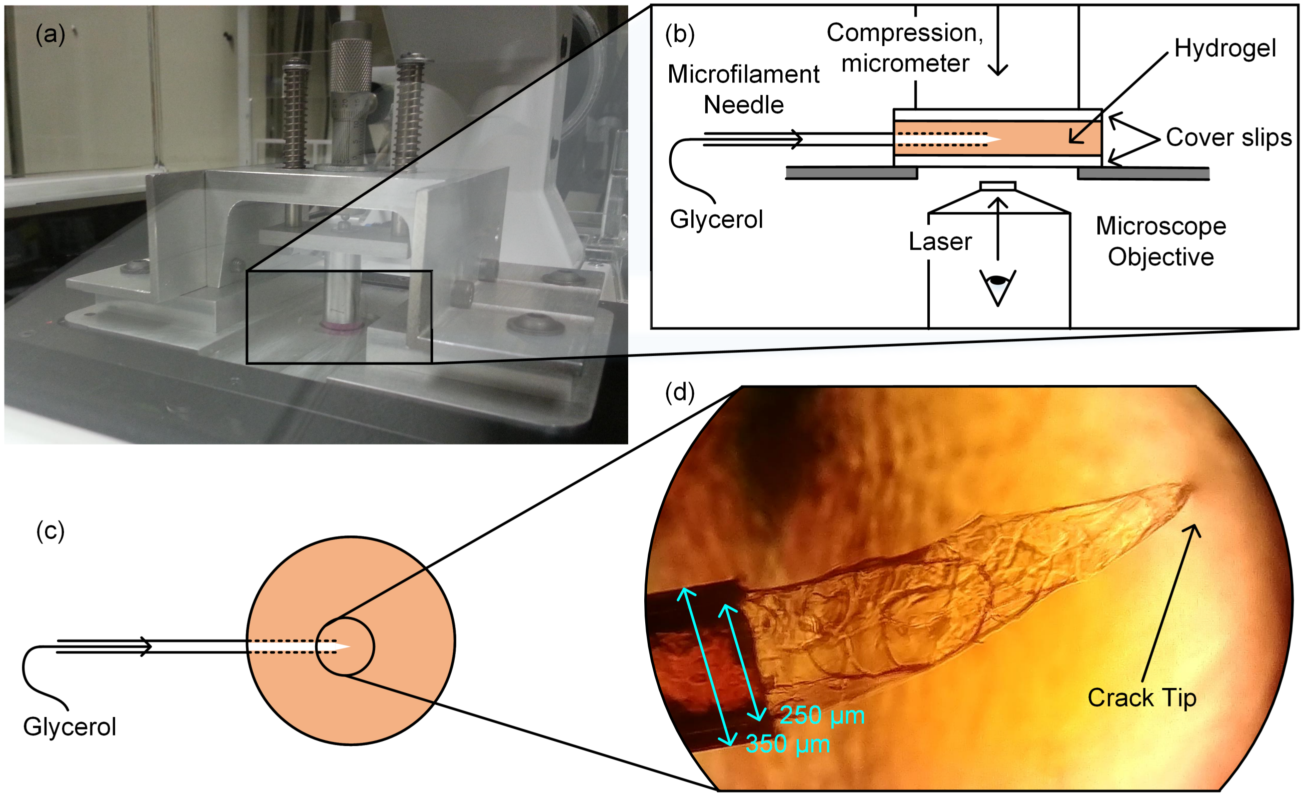

Figure 2.2: (a) Uniaxial compression device mounted on a standard microscope stage insert with a hydrogel specimen. (b) Side view of the experimental configuration with a specimen under compression applied via micrometer and a microfilament needle used to inject glycerol into a precrack. (c) Top view of the specimen and (d) a wide-field image of the specimen with a crack ahead of the microfilament needle.

Imaging

Confocal microscopy captures images by using pinholes and objective lenses to capture light from a single point in three-dimensional space. Raster scanning produces two-dimensional planar images and moving the specimen closer to or farther from the objective allows for building of 3D image stacks from the 2D planes. If the material imaged is optically transparent, like a hydrogel, one can capture a volumetric image of detectable features inside the material. In most cases, confocal microscopes capture reflected or emitted light, so fluorescent dyes are commonly used to make features such as cells detectable. Fluorescent particles or beads are also frequently used as the detectable feature within a gel.

In these experiments, imaging is conducted on a Zeiss inverted laser scanning confocal microscope (LSM 800) with Zen Blue System software. A diode laser excites the fluorescent microspheres that serve as a speckle pattern for image and correlation analyses by emitting light that is captured by a photomultiplier tube (PMT). A pinhole size of approximately one Airy Unit (AU) is used for each imaging configuration to optimize the signal to noise ratio in images. For each experiment, laser intensity and PMT master gain adjustments regulate the number of over exposed voxels. A typical experiment uses a 20× plan-apochromat (corrected for spherical and chromatic aberrations) objective with a 0.8 numerical aperture (NA) and 550 μm working distance (WD). For the green microspheres, a 488 nm laser at 2-4.5% intensity and 600-650 V master gain with a 34 μm pinhole is used. For the red microspheres, a 561 nm laser at 0.25% intensity and 575 V master gain with a 37 μm pinhole is used.

Both 2D time-series and 3D volumetric images are captured during each experiment. The 2D images are captured at 0.933 s intervals and imaging begins when the glycerol pump starts. Once the crack begins to advance the pump is turned off and imaging continues as the crack advances, following the crack path during the whole propagation event. Due to the high viscosity of the glycerol and small diameter of the needle, glycerol continues to enter the initial crack at a steady rate after the pump is turned off. There is no fluid outlet and pressure continues to build in the crack until propagation occurs. Imaging stops when the crack either arrests or reaches the edge of the loading device's viewing window. In a few cases, crack renucleation after arrest is also imaged. Volumetric images, also called z-stack images, are taken before crack propagation begins and after final arrest. A typical z-stack image consists of approximately 200 to 400 slices at 1.25 μm intervals.

The 2D imaging rate of approximately one 512×512 pixel frame per second requires very slow crack propagation rates. For the volumetric images, imaging takes two orders of magnitude longer ($\sim$ $200 - 400s$) necessitating a stationary crack. In addition, if we want to image through the full thickness of the specimen we must consider working distance and imaging depth constraints. With the 550 μm WD and cover slip thickness of 100 μm ± 20 μm, we can theoretically image a 450 μm ± 20 μm compressed specimen. However, the fluorescent microsphere density also contributes to limiting the depth of view. More sparse speckles allow for deeper imaging depths but limit the resolution of image correlation. In most cases, imaging up to 150-200 μm deep within a specimen is usable for analysis.

2.3 Analysis

Several analyses are conducted on each set of images. For the 2D images captured during crack propagation we analyze the strain field near the crack tip using digital image correlation (DIC) [23]. We also quantitatively determine factors describing the crack propagation event including the crack speed, crack tip opening displacement (CTOD, δ), energy release rate (G), and stress intensify factor (K). Qualitative analysis of renucleation events and crack path allow us to examine the complex mechanisms at play in soft materials and hydrogels. For the 3D images we also determine quantitative metrics describing the through-thickness 3D crack shape.

Inducing Crack Propagation

First we assess the validity of our method to induce crack propagation. In the oil and gas industry, injecting fluid into hole through a solid to cause fracturing of the solid is known as fracking. Mechanics theory of fracking essentially simplifies the problem to a plane strain hole in an infinite plate with far-field compression and internal pressure. Far-field compression is a result of the mass of earth around the drilled bore where horizontal and vertical compression are typically on the same order of magnitude. Under this compression alone, the rock is stable with net compressive stresses on the hoop around the hole. Fracking fluid is injected under high pressure and when a critical pressure is reached, a net tensile hoop stress results in the direction of the highest compressive load. Fracture occurs at these tensile hoop stresses, and propagates parallel to the highest compressive load [24, 25]. While our experimental materials are significantly different from those of traditional fracking, our geometry is comparable, thus allowing us to apply a similar analysis and show that the initial vertical compressive load we apply before inducing crack propagation helps to stabilize crack orientation to be perpendicular to the cover slips. Since specimen diameter is almost two orders of magnitude larger than specimen thickness, there is effectively a horizontal compressive load on the bore hole produced by the needle and injected glycerol.

There are some key differences in our geometry compared to that of traditional fracking. First, our specimens are very thin compared to their diameters and the bore hole diameter is comparable to the specimen thickness. This results in an effective weak direction perpendicular to the cover slips. However, without the initial compressive load we were not able to achieve stable, slow crack propagation. In addition, we are interested in propagating a crack ahead of the needle tip, at the end of the bore hole rather than radially outward from the bore. Even though the specimen is thin, the applied compression confines the specimen edges, leading us to expect plane strain conditions. Experimental images show that a wedge shaped parabolic crack advances ahead of the needle tip, so 2D plane strain analysis at internal planes will allow us to characterize fracture properties from these experiments.

We use two freely available Matlab codes to perform DIC and measure the strain field near the crack tip to verify that we are measuring a fracture event in our specimens [26, 27]. The size and shape of the high strain region are indicative of the process zone size and fracture mode. Near the crack tip, in the high strain regions, there may be plastic (inelastic) deformations that dissipate energy. The process zone is generally considered to be a smaller region within the plastic zone where nonlinear processes that lead to fracture occur [28, 29]. Geubelle and Knauss [30] estimate the size of this nonlinear region for a hyperelastic material as

$$r_{NL} = \frac{1}{3\pi}\frac{J}{\mu}, \tag{2.1}$$

where μ is the bulk modulus which can be related to Young's modulus, E and the Poisson's ratio, ν in linear elasticity as

$$\mu = \frac{E}{2(1+\nu)}, \tag{2.2}$$

and J is Rice's J-integral, which corresponds to the energy release rate [31].

Propagation

Several propagation events were extracted from the time series images for each fracture experiment and analyzed to measure crack shape, position, and speed.

Initial observations of the crack shape appear to be parabolic. A parabolic crack opening shape allows us to measure fracture energy from opening displacements knowing the material's elastic properties [28, 32, 33].

Assuming linear elastic fracture mechanics, the crack opening profile, $\delta(r)$ is parabolic and given by [32]

$$\delta(r) = \frac{8K}{\sqrt{2\pi}E'}\sqrt{r}, \tag{2.3}$$

where r is the distance along the crack surface away from the tip, K is the stress intensity factor, and E' is defined in Eq. 1.6. A second order polynomial (parabola) is fitted to the crack shape. To account for initial misalignment and crack meandering (local changes in crack orientation that appear to follow a quasi-periodic pattern) during propagation, an angular sweep from zero to π radians with a step size of 0.001 radians is used and the best fit is selected based on the minimum sum of square residuals of the rotated polynomial fits. A common method of measuring the crack tip opening displacement, CTOD, involves using the intersection of the crack surface with lines at 45° from the vertex of the fitted parabola [31, 34]. This concept is illustrated in Fig. 2.3. We can use this to determine the relationship between $\sqrt{r}$ and $\delta(r)$ using the parabolic shape, where

$$r_t = \frac{\delta_t}{2}, \tag{2.4}$$

δ_t is the CTOD, and r_t is the distance from the crack tip where δ_t is measured. Then

$$\frac{\delta_t}{\sqrt{r_t}} = \frac{\delta_t}{\sqrt{\delta_t/2}} = \sqrt{2\delta_t}. \tag{2.5}$$

This allows us to calculate the stress intensity factor from Eq. 2.3 and 2.5 as

$$K = \frac{\sqrt{\pi\delta_t}E'}{4}. \tag{2.6}$$

Using Eq. 1.5 the energy release rate assuming small scale yielding is

$$G = \frac{\pi\delta_t E'}{16}. \tag{2.7}$$

Thus, the stress intensity factor and energy release rate can be determined from the CTOD and material properties.

An estimate of r_{NL} (Eq. 2.1), the size of the nonlinear region, can be found using $J = G$ for linear elastic materials [28, 32–34]. Combining Eq. 2.1, 2.2, and 2.7,

$$r_{NL} = \frac{1+\nu}{24}\lambda\delta_t, \tag{2.8}$$

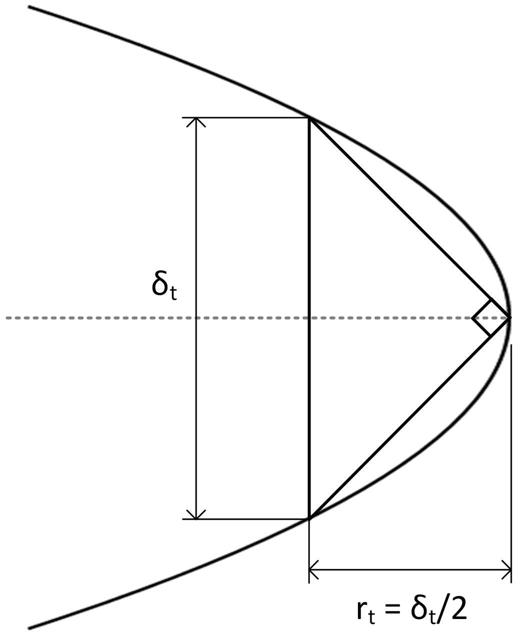

Figure 2.3: Parabolic crack opening profile with the crack tip opening displacement, δ_t, determined by the intersection of lines at 45° from the vertex of the parabola.

where

$$\lambda = \begin{cases} 1 & \text{for plane stress,} \\ \frac{1}{1-\nu^2} & \text{for plane strain.} \end{cases} \tag{2.9}$$

The crack tip location is assumed to be the vertex of the fitted parabola. To determine the change in crack length, we consider both a straight path approximation and account for meandering of the crack tip. For the straight path assumption, advancement is measured as the distance between the current crack tip location and a fixed reference location, typically the initial crack tip. In the meandering case, local and incremental changes in crack orientation are assumed to contribute to the actual length of the crack and advancement is measured incrementally between image pairs, where the sum of these incremental advances represents the net crack length relative to the reference image. Crack speed is measured as the change in crack tip location over time and is affected by both the geometry of the crack and the compressive pre-load applied to the specimens.

Renucleation

In addition to studying crack propagation, we are also able to observe crack renucleation events in some specimens after an arrest occurs. We make several qualitative observations on renucleation sites and large local deformations indicated by apparent changes in speckle density. We also conduct a preliminary quantitative analysis of these local changes in speckle density. A renucleation site is identified and the mean gray intensity value in that region is measured as the new crack begins to form. A second region of comparable size where no renucleation event occurs is also analyzed for comparison.

Crack Shape

To understand the through thickness or spatial variation in crack front shape, we apply similar CTOD analyses as were applied to understand crack propagation. Since volumetric images take orders of magnitude longer to capture than 2D images, crack shape analysis is conducted for stationary cracks only using 2D planes from the volumetric image. In order to capture the geometry in a configuration as close as possible to that of a propagating crack, we primarily use images captured after a crack has fully arrested post propagation event.

2.4 Results and Discussion

Based on visual observations using the microscope eye-piece at the beginning and end of experiments, we successfully introduce an initial crack and propagate that crack using the fluid injection method described in Section 2.2. The crack appears to be wedge shaped as expected from fracking and fracture theories [24, 25]. DIC results further support these observations. A representative example of the displacement vectors and magnitudes ($|\underline{u}|$) in the vicinity of the crack tip during a crack propagation event is shown in Fig. 2.4(a). As expected, there are very large deformations on the crack faces especially near the crack tip and almost no deformations far ahead of the tip. The resulting difference in principal strain field shown in Fig. 2.4(b) indicate that there is a high strain region ahead of the crack tip as expected from fracture mechanics theory.

The shape of the high difference in principal strains region near the crack tip is consistent with what we would expect for Mode I crack opening and plane strain approximation in fracture theory. Additionally, Fig. 2.4(c) shows the size of the region with strains over 0.1 or 10% is comparable to the crack tip opening displacement (CTOD) results discussed in the following section.

Mechanical properties of the gel were determined using an ARES-RFS Rheometer. Results of a dynamic frequency sweep analysis at varying strains are shown in Fig. 2.5. The gel shows no rate sensitivity for the range of frequencies studied and

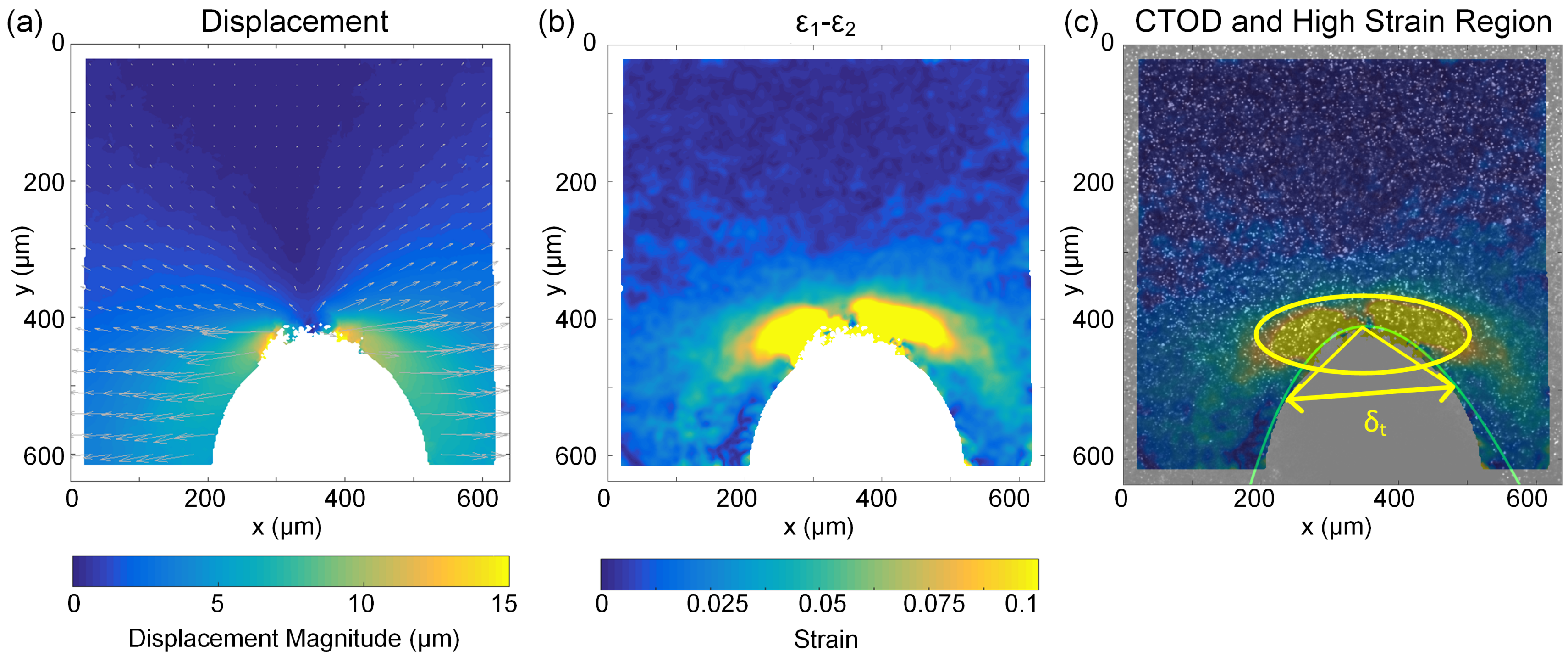

Figure 2.4: Representative results for image #1305 during a crack propagation event: (a) 2D DIC results where the colors correspond to displacement magnitudes and the arrows indicate the direction of the displacements and scale in length with the magnitude. (b) Difference in principal strains (measure of shear) plot showing evidence of strain concentration ahead of the crack tip. (c) Representation of the crack tip opening displacement (CTOD) and large difference in principle strains region overlayed on a speckle image.

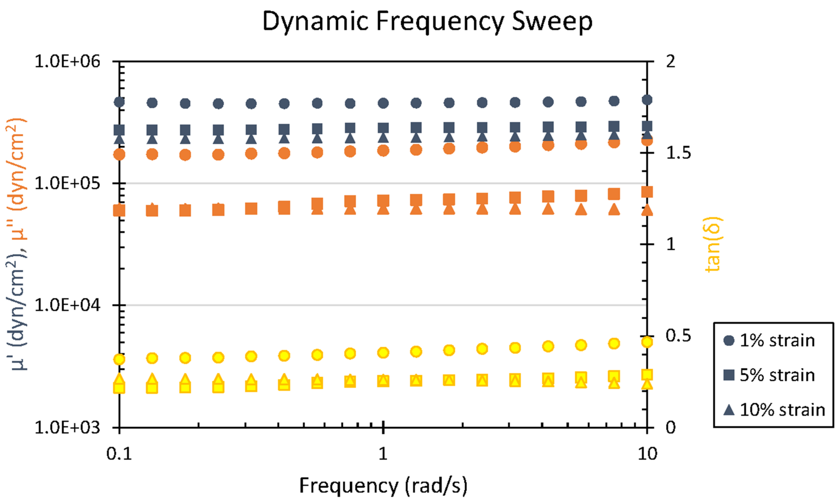

Figure 2.5: Dynamic frequency sweep analysis of the gel at different strain levels.

exhibits no detectable creep over time periods of up to 20 minutes. However, it does show moderate strain sensitivity with a stiffer response at higher strains quickly exhibiting an almost constant, more compliant response at higher strains. Since there is little difference between the response for 5% and 10% strain, the average storage modulus at relatively high strains is $\mu = 26 \pm 2\ kPa$. Polymer gels can be considered incompressible which corresponds to a Poisson's ratio of 0.5, which gives a Young's Modulus, $E = 78 \pm 7\ kPa$.

Propagation

Although imaging began when the glycerol pump started, due to the glycerol's high viscosity and the very small needle diameter, there was a delay before hydrostatic pressure built up to open and eventually advance the crack. Once propagation began it generally continued steadily and slowly for a while before either significantly slowing or suddenly arresting. There are a few likely and possibly interrelated reasons as to why the crack arrests: variation in the gel thickness would change the total critical energy needed for propagation while energy is simultaneously expended in forming new crack surfaces. Additionally, heterogeneities such as local variations in polymer structure and composition could significantly affect local mechanical and fracture properties of the gel thus changing the critical energy for propagation. Since polyacrylamide is a relatively simple polymer it can crystallize in regions with low crosslinking density. The gel recipe that was employed has a relatively high crosslinker concentration of 5% and hence, we do not expect significantly large regions of crystallization.

Figure 2.6 shows a representative series of images taken from a crack propagation event. Prior to image #1301, the crack opens very slowly as pressure builds up. Then it opens more quickly until just before image #1305 when significant propagation begins and the crack propagates steadily for several seconds. The crack itself is the black region with no speckles that is well fit to a parabola, as shown by the lines in the figure. Crack tip advancement is represented by the almost vertical arrows in images #1305 and #1309. This crack shows some meandering, with the rotation of the fitted parabola varying as the crack advances.

Assuming plane strain condition and using 78 kPa as the Young's modulus, 0.5 as Poisson's ratio, and the measured CTODs ($\delta_c tc$) as indicated on Fig. 2.6, the energy release rate (G_c) and stress intensity factor (K_c) were calculated for each opening and propagation event. Figure 2.7 shows a representative plot of CTOD as the crack advances for four propagation events in the same specimen, where event #2 is shown in the other figures in this section. Since imaging started when the crack was almost open to its critical value of the CTOD, the characteristic build up of energy before propagation is not shown in this plot. Once the crack begins to advance, the measured CTOD and thus the energy release rate is approximately constant. The horizontal dashed lines in the figure indicate the mean CTOD for each event. The first three events are taken from a continuous propagation event where the crack slowed but did not arrest between each event and have an average CTOD of 339 ± 36 μm. This corresponds to an SIF of 850 ± 91 $pa\sqrt{m}$ and ERR of 6.9 ± 1.0 $Pa.m$ (J/m^2). The fourth event occurred after the crack arrested and thus required a higher CTOD, 528 ± 41 μm, corresponding to an SIF of 1060 ± 100 $pa\sqrt{m}$ and ERR of 10.8 ± 1.3 $Pa.m$ (J/m^2), to renucleate from the crack tip before propagation could continue. Error is reported as one standard deviation form the mean and is comparable to the errors reported in the literature for more traditional fracture experiment geometries such as single-edge notched bend (SE(B)) tests [2, 35]. The arrow indicates that after renuclation occurs, the CTOD required to continue propagating the crack returns to a similar level as in the other three events. Renucleation results are discussed further in the next section. The mean CTODs and calculated values of K_c, G_c, and r_{NL} are shown in Table 2.1.

The mean CTOD during propagation is comparable to the diameter of the needle used to inject the glycerol and drive the crack propagation. Since the needle tip is relatively far away from the crack tip (typically at lease 1 mm away) we do not expect that varying the needle diameter would significantly impact the CTOD

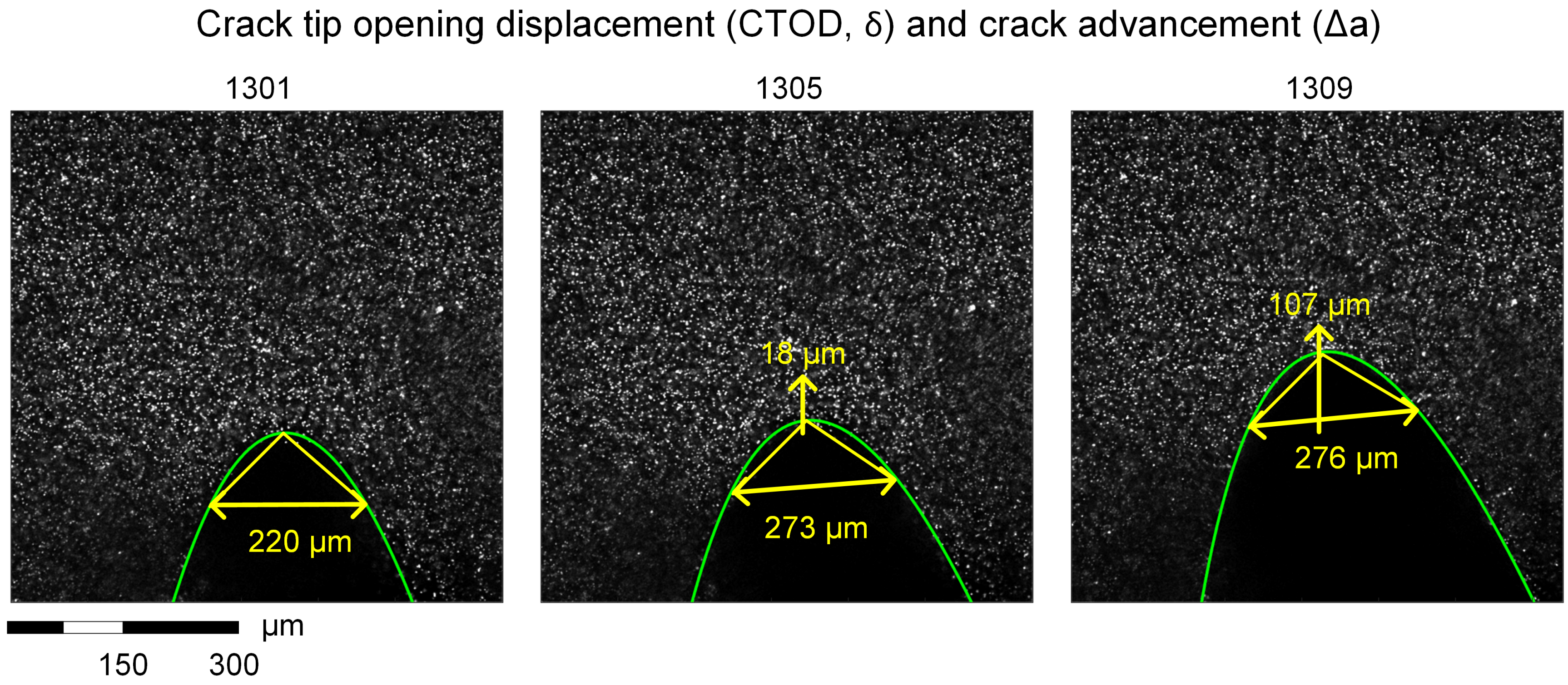

Figure 2.6: 2D internal plane images of a representative crack advancing through a gel specimen. There is an interval of approximately four seconds between each of the images shown. The crack opening shape is fitted to a parabola shown by the green line. Yellow lines at 45° from the parabola vertex are used to measure CTOD which is marked by horizontal arrows on each image. A vertical arrow indicates the direction of crack tip advancement.

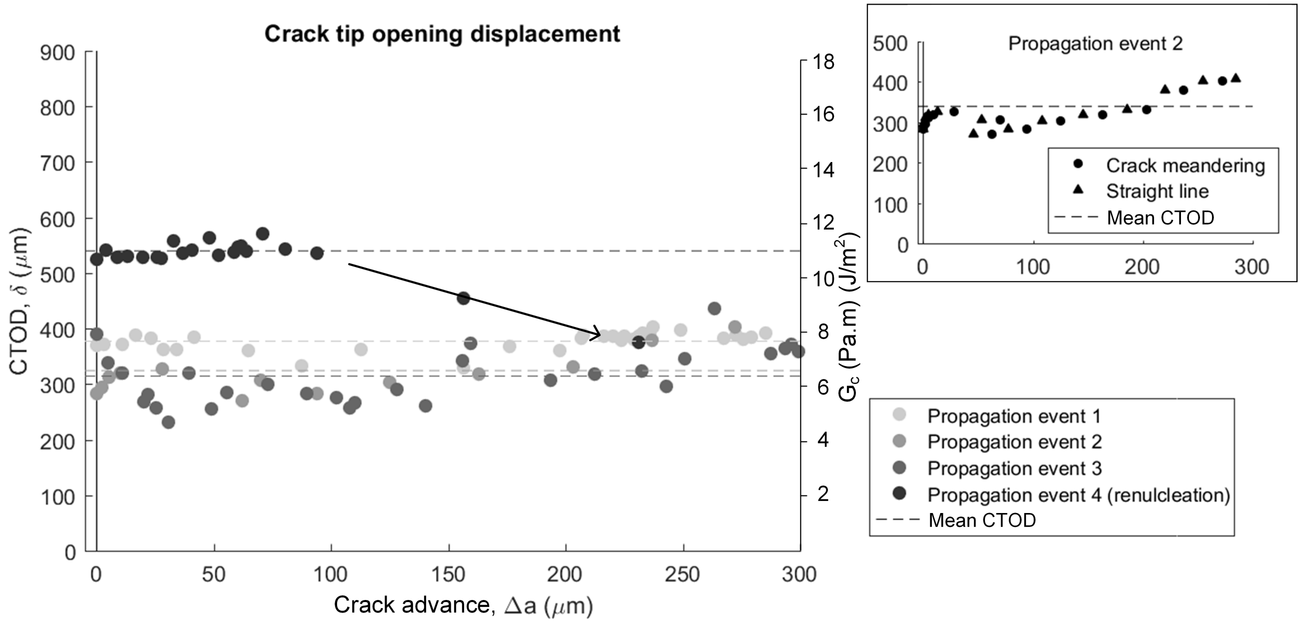

Figure 2.7: Crack tip opening displacement (CTOD), δ_{tc}, versus measured crack advance, Δa, during four propagation events in the same specimen. Event #4 shows an arrested crack that renucleates before it begins to propagate again. The inset compares two methods of estimating crack length, considering crack meandering (circles) and a straight path (triangles) during the third propagation event. The mean CTOD for each event is indicated by the horizontal dashed lines.

Table 2.1: Fracture parameters: δ_{tc} measured from images; K_c, G_c, and r_{NL} calculated from δ_{tc} and material properties

	δ_{tc}		K_c		G_c		r_{NL}	
Propagation Event	mean μm	st.dev. μm	$Pa\sqrt{m}$	st.dev. $Pa\sqrt{m}$	$Pa.m$	st.dev. $Pa.m$	μm	st.dev. μm
1	377	16	900	83	7.7	0.8	31	1.4
2	324	43	830	93	6.6	1.1	27	3.6
3	314	48	820	97	6.4	1.1	26	4.0
avg. 1-3[a]	339	36	850	91	6.9	1.0	28	3.0
4	528	41	1060	100	10.8	1.3	44	3.5

[a] Averaged of propagation events 1 through 3.

during propagation. For a larger needle diameter we would expect the crack tip to propagate further ahead of the needle and for a smaller diameter we would expect to see the CTOD increase significantly before propagation begins. However, further investigation of needle size effects are recommended for future studies.

Although propagation event #4 is a renucleation event, the plot in Fig. 2.7 shows the crack advancing for almost 100 μm prior to the actual crack propagation event. In this plot, crack advance, Δa, is measured accounting for crack meandering. Even when the crack arrests and renucleates, there are still small changes in the crack orientation that result in an increase in the measured crack advance. The inset in Fig. 2.7 shows that during an active propagation event there is little difference between measurements of crack advance when assuming crack meandering (circles) compared to assuming the crack follows a straight path (triangles). While considering meandering does not affect the mean fracture energy (G_c) during propagation, it does give us a more complete picture of the fracture event. In propagation event #4 when the crack arrests, the crack meandering assumption led to large differences in the calculated crack length. However, since the energy release rate is proportional to the surface area of the crack formed, an accurate measure of the crack advance includes local changes in crack orientation and crack surface roughening. This is an important part of understanding the mechanisms affecting fracture. Several researchers have observed that for very slowly propagating cracks in brittle materials there is significant surface roughening [2, 17, 18]. This effect seems to be particularly pronounced in soft gels and can have an impact on measured fracture energy since longer crack paths require more fracture energy. Since our experiments are at the sub-millimeter scale, it is possible that local variations in polymer composition and water content are coming into play. Stiffer or less hydrated regions in the gel may be producing an effective local increase in toughness resulting in the crack path deviation. Locally high stresses may magnify these effects by mechanically forcing water away from the high stress regions.

Variation in specimen thickness as the crack advances may play a role in the variations in fracture energy observed in different propagation events in the same specimen. If the gel becomes thicker or thinner as the crack advances, the new surface area created by the crack propagation would be larger or smaller respectively. Since creating a larger surface area would require more energy, the apparent toughness may increase where the gel is thicker. However, after the crack arrests there is a pronounced increase in fracture energy, indicating that it is likely that a local toughening mechanism is at play. In order for the crack to renucleate, we do expect that more fracture energy is needed.

Renucleation

After a propagating crack arrests, pressure in the fluid filled crack must increase sufficiently before renucleation can occur. The pressure increases by pumping more glycerol into the crack. We have observed several cases of renucleation in these fracture experiments. In many cases, a crack will slow significantly and arrest temporarily before continuing on a nearby path after opening more, indicating some kind of toughening mechanism or local variation in toughness is likely at play. Figure 2.7 shows that a larger CTOD and thus more energy is needed for one of these renucleation events. If the previous crack path turned or deviated significantly from the original crack, stresses can build up at one of the corners or turns resulting in crack branching far away from the previously active crack tip. These events are observed post-mortum after an experiment is completed since we have a single, small frame of view at the previously active crack tip. Commonly, crack path meandering will result in defects or weak spots on the crack surface. When the crack arrests near one of these defects, large local deformations begin in the region near the defect. One such event can be observed in Fig. 2.8 where this increase in local deformation can be seen as a local decrease in speckle density beginning to become apparent in image #50 until some critical limit at which a new crack opens as indicated in image #60. Figure 2.9 shows the variation in mean gray intensity at the renucleation site. The sharp change in slope of the gray intensity trend signifies a transition from local large deformations to crack opening.

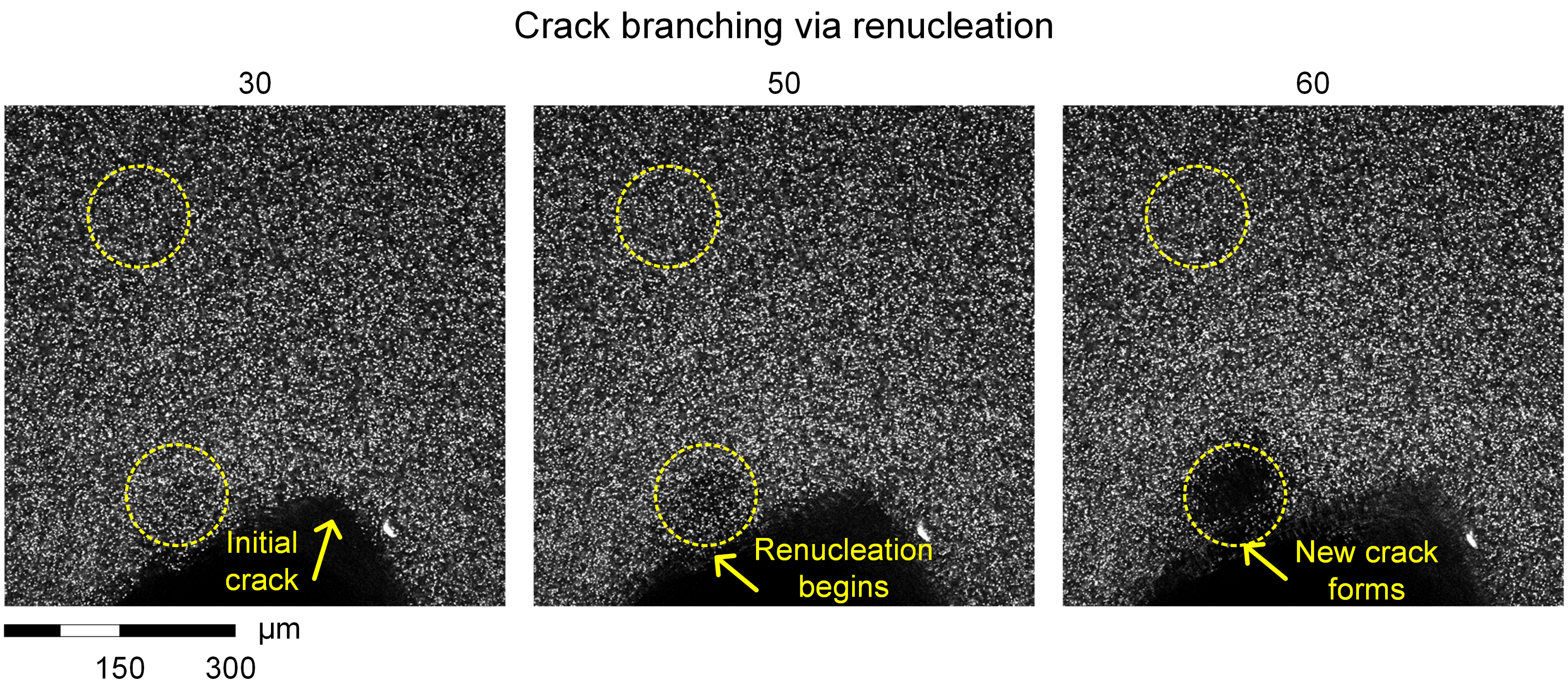

Figure 2.8: An example of 2D crack renucleation in: image #30 an initial crack that has arrested, image #50 a localized region of deformations where renucleation begins, and image #60 a new crack forming while some ligaments remain attached. The circles show regions used for speckle density analysis.

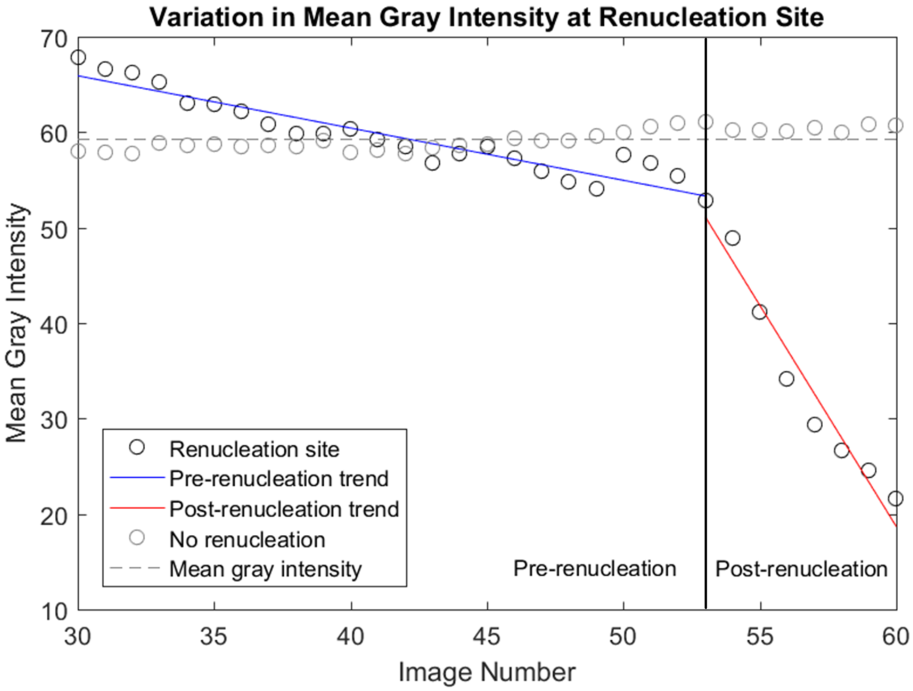

Figure 2.9: Comparison of the gray scale intensity variation at the renucleation site to an area with no renucleation where the regions used in this analysis are shown in Fig. 2.8. Image #53 is taken as the transition between pre-renucleation local large deformations and post-renucleation crack opening. The area with no renucleation has approximately constant mean gray scale intensity.

Close examination of the images reveals that some gel ligaments remain intact initially but break as the new crack opens further and propagates. The attached ligaments indicate crack jumping which strongly suggests that strain hardening effects are leading to local toughening. It is very challenging to measure CTOD during these branching type renucleation events. If the crack renucleates in the original path, we can measure an increase in CTOD prior to the renucleation event. However, in a case where there is branching, the CTOD cannot be measured until the crack fully renucleates. These renucleation events close to the initial crack tip may be one of the mechanisms at play in the slow crack roughening observed by earlier researchers [2, 17, 18].

In the experiments, the hydrostatic pressure is assumed to be constant throughout the whole propagated crack's length. Unlike more traditional tearing or opening type fracture experiments, this geometry allows for renucleation to occur anywhere along the crack path with sufficient stress concentration. Regardless of the renucleation location, these events are indicative of local toughening at the crack tip. That is, the energy needed to resume propagation from the arrested crack tip is higher than that needed to renucleate a crack elsewhere along the crack surface. High stresses can cause local deswelling in hydrogels, significantly changing local material properties. Deswelled gels have a much smaller volume and are significantly stiffer than in the fully swelled state. It may be possible to detect local deswelling as a local increase in mean gray intensity. A local decrease in volume also contributes to stress concentrations in these regions, which impact crack growth. It has been suggested in the literature that fracture surface roughening, especially in soft hydrogels, is caused by local toughening mechanisms, which is supported by these experiments and discussed further in the next section [17, 18].

Crack Shape

Although we were able to achieve very slow crack speeds, <50 $\mu m/s$, by injecting glycerol into the crack at a very slow rate and by applying a compressive pre-load, these speeds were not slow enough to be able to volumetrically capture the crack shape evolution in 3D during a propagation event. We were, however, able to observe geometric features of the fractured gels for initial and arrested cracks. In these analyses, speckle density became critical. The speckles must be sufficiently dense to make a good approximation of the crack shape but if the speckles are too dense they will limit imaging depth. The particles can effectively cast shadows on deeper imaging planes reducing the accuracy of crack shape analysis for deeper layers. Figure 2.10 shows a representation of the initial crack shape for one of the specimens where the parabolas fitted to the crack shape in each z-plane image are shown as a surface plot within the speckles. In this case the speckle density caused shadowing to limit our analysis to approximately half the specimen thickness, about 120 μm.

Some variation in crack tip location can be observed through the thickness. Additionally, the opening displacement and thus the virtual energy release rate or the stress intensity factor shows significant variation. To better understand this variation, Fig. 2.11 shows how the CTOD (δ_t) varies with depth. A linear best fit line indicates a generally increasing CTOD from the cover slip toward the middle of the gel. Immediately adjacent to the cover slip-gel interface the CTOD is typically higher and then drops about 10 μm from the interface before increasing significantly. In the region of the interface, significant noise is expected in the CTOD measurements due to distortions resulting from the mismatch in optical properties between the cover slip and the gel. However, a higher CTOD is expected at the gel surface

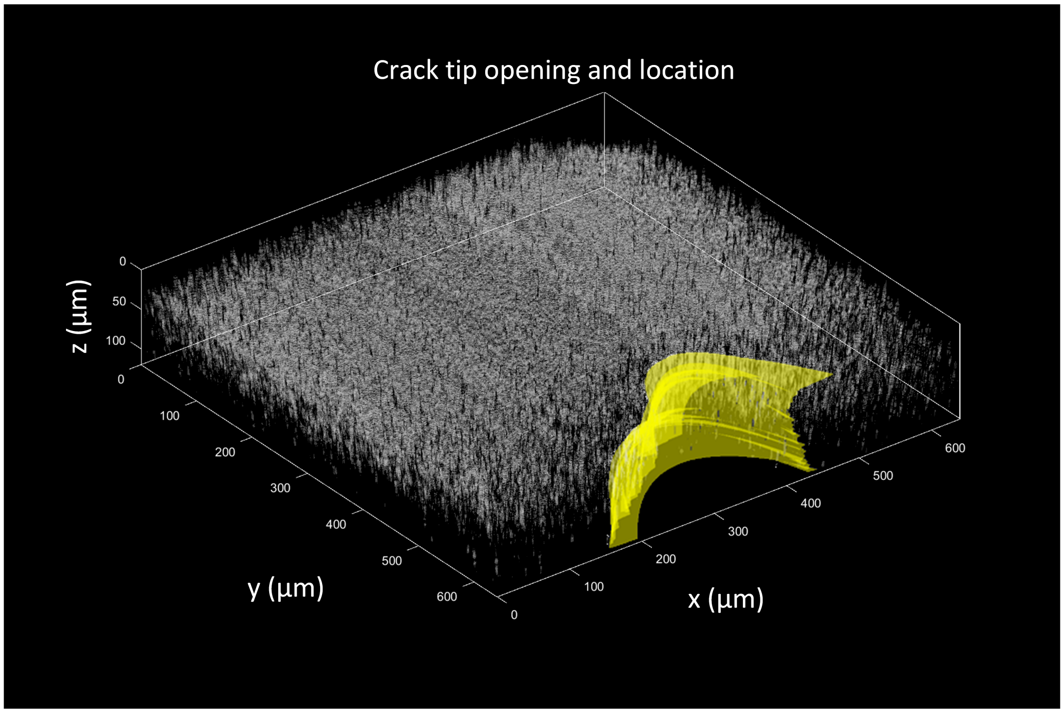

Figure 2.10: 3D representation of an initial crack shape (yellow) and location prior to crack propagation in a volumetric speckle image.

due to both surface pinning and gel-cover slip interfacial bonding effects. Due to the confining compression and friction between the gel and cover slip, the crack does not open as much as would otherwise be expected at the surface.

Where we have been able to measure crack shape deeper into the gel, the CTOD appears to level out in the middle of the gel suggesting that the CTOD will decrease again toward the second cover slip. This trend is in line with what we would expect from traditional LEFM theory which suggests plane stress conditions near the gel surfaces requiring less energy for propagation, and plane strain conditions in the center of the gel requiring more energy for propagation. Although these specimens are very thin, they are also confined, and hence, we expect plane strain assumptions to apply for most of the interior of the specimen.

In addition to understanding how the CTOD varies through the specimen thickness we also seek to understand how the crack tip location varies as a function of both the depth and the CTOD. We determine the crack tip location as the vertex coordinates of the parabola fitted to the crack shape, as we did in our 2D crack propagation analysis. For the purposes of this analysis we are interested in the magnitude of variation in crack tip location and we use the magnitude of the tip location vector

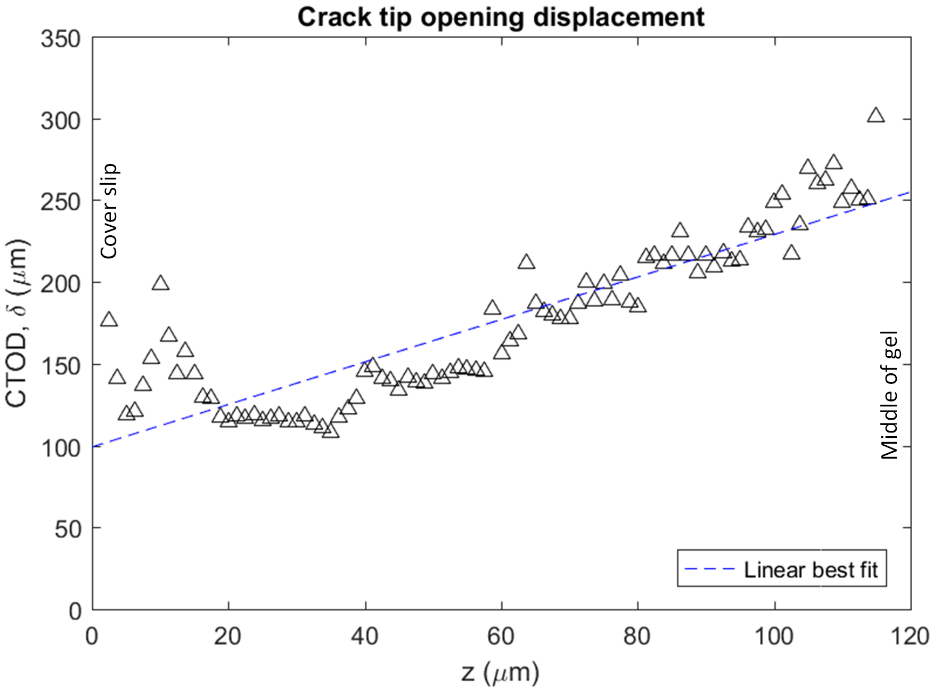

Figure 2.11: Crack tip opening displacement variation through the specimen thickness from the cover slip surface ($z = 0\ \mu m$) to approximately the middle of the gel ($z = 120\ \mu m$).

as our measure of the crack tip location. Figure 2.12 shows an example plot representing the relationship between a (tip location), δ_t (CTOD), and z (depth).

No clear trends beyond what has been described for CTOD varying with depth were observed in this data. In general, the crack tip location showed significant variation through the specimen thickness and even had relatively sharp, almost discontinuous changes in location. These variations do not seem to correlate with the CTOD. The changes in crack tip location through the thickness are, however, suggestive of the observed fracture surface roughening in the literature[2, 17, 18]. In particular, Baumberger et al. [17] observed development of crack front discontinuities for crack speeds below a critical velocity. These studies also show chevron or cross-hatch shaped patterns on the crack surface on the millimeter scale. Our experiments are on the sub-millimeter scale which is comparable to the feature size observed in the literature, and hence we did not observe similar patterns on our crack surfaces. However, further study of the evolution of crack shapes in 3D including postmortem imaging of the fracture surface may reveal more about the development and formation of these characteristic features.

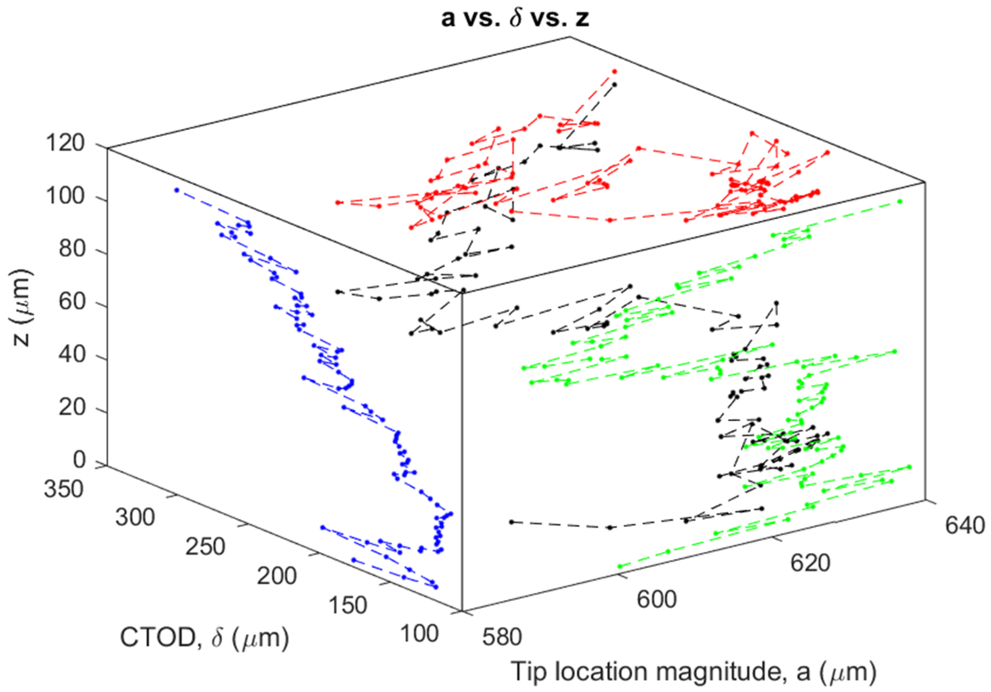

Figure 2.12: Plot showing how crack tip location (a) varies with CTOD (δ) and with depth (z) represented by the black line. The blue line plots δ versus z, the green line a versus z, and the red line δ versus a.

2.5 Conclusions

In this chapter we presented an experimental method to induce very slow crack propagation in thin hydrogel specimens while using confocal microscopy to capture fluorescent speckle images. 2D images are captured during crack propagation and 3D volumetric images are captured both before propagation begins and after the crack arrests. We also presented a methodology to determine crack tip opening displacement (CTOD) on the sub-millimeter scale and fracture energy from crack geometry and specimen stiffness. Before propagation begins there is a build up of fracture energy which corresponds to strain concentration in the vicinity of the crack tip measured using Digital Image Correlation (DIC). This suggests that knowing just the CTOD, we can measure fracture toughness in soft brittle materials during crack propagation. We also observe crack arrest and renucleation events which suggest local toughening. This points to a possible mechanism for the fracture surface roughening observed for slow cracks in the literature. In addition to these 2D analyses, we analyzed 3D crack shapes to better understand through thickness variations. We found that fracture energy seems to be higher at the edges and in the middle of specimens which is consistent with Linear Elastic Fracture

Mechanics (LEFM) theory and the assumption of plane strain conditions in the confined specimen.

Analysis of the existing data accounting for the gel's strain sensitivity through a Neo-Hookean material model may provide more insights into the fracture mechanics of these soft gels. Fracture tests using more traditional geometries such as peeling test could also be conducted and compared to the method developed and presented in this chapter. Additionally, further experiments either at higher resolution or under higher magnification and with smaller fluorescent microspheres as the speckle pattern are recommended to better understand the crack renucleation mechanisms observed in this work. These experiments will also allow for closer examination of the fracture surface and contribute to a better understanding of the crack surface roughening observed both in this work and in previous experiments. Further, the experimental and analysis methods developed here can be applied to study damage development and mechanisms in heterogeneous and toughened gels. Elastic and toughness contrasts can be used to improve our understanding of the mechanics of such toughening mechanisms, leading to developments in soft structural materials for biological and other applications.

Acknowledgments

This material is based upon work supported by the National Science Foundation Graduate Research Fellowship under Grant No. DGE-1144469 and Award No. DMS-1535083 under the Designing Materials to Revolutionize and Engineer our Future (DMREF) program. Imaging was performed in the Biological Imaging Facility, with the support of the Caltech Beckman Institute and the Arnold and Mabel Beckman Foundation.

Computational Details

The Digital Image Correlation (DIC) analyses in this chapter were obtained using the following Matlab packages:
FIDIC (Fast Iterative DIC): `https://github.com/FranckLab/FIDIC`.
Ncorr v1.2: `http://www.ncorr.com/index.php/downloads`.

REFERENCES

[1] P.-G. de Gennes. Soft matter: more than words. *Soft Matter*, 1(1):16, 2005. doi: 10.1039/B419223K.

[2] F. Baldi, F. Bignotti, I. Peroni, S. Agnelli, and T. Riccò. On the measurement of the fracture resistance of polyacrylamide hydrogels by wire cutting tests. *Polymer Testing*, 31(3):455–465, 2012. ISSN 0142-9418. doi: 10.1016/j.polymertesting.2012.01.009.

[3] R. Long and C.-Y. Hui. Fracture toughness of hydrogels: measurement and interpretation. *Soft Matter*, 12(39):8069–8086, 2016. ISSN 1744-683X. doi: 10.1039/C6SM01694D.

[4] S. Coyle, C. Majidi, P. LeDuc, and K. J. Hsia. Bio-inspired soft robotics: Material selection, actuation, and design. *Extreme Mechanics Letters*, 22: 51–59, 2018. ISSN 2352-4316. doi: 10.1016/j.eml.2018.05.003.

[5] J. P. Gong and Y. Osada. Soft and wet materials: From hydrogels to biotissues. In M. Cloitre, editor, *High Solid Dispersions*, pages 203–246. Springer Berlin Heidelberg, Berlin, Heidelberg, 2010. ISBN 978-3-642-16382-1. doi: 10.1007/12_2010_91.

[6] P. Moshayedi, G. Ng, J. C. F. Kwok, G. S. H. Yeo, C. E. Bryant, J. W. Fawcett, K. Franze, and J. Guck. The relationship between glial cell mechanosensitivity and foreign body reactions in the central nervous system. *Biomaterials*, 35(13): 3919–3925, 2014. ISSN 0142-9612. doi: 10.1016/j.biomaterials.2014.01.038.

[7] N. Annabi, J. W. Nichol, X. Zhong, C. Ji, S. Koshy, A. Khademhosseini, and F. Dehghani. Controlling the porosity and microarchitecture of hydrogels for tissue engineering. *Tissue Engineering. Part B, Reviews*, 16(4):371–383, 2010. ISSN 1937-3368 1937-3376. doi: 10.1089/ten.teb.2009.0639.

[8] A. J. Engler, S. Sen, H. L. Sweeney, and D. E. Discher. Matrix elasticity directs stem cell lineage specification. *Cell*, 126(4):677–689, 2006. ISSN 0092-8674. doi: 10.1016/j.cell.2006.06.044.

[9] M. Whang and J. Kim. Synthetic hydrogels with stiffness gradients for durotaxis study and tissue engineering scaffolds. *Tissue Engineering and Regenerative Medicine*, 13(2):126–139, 2016. ISSN 2212-5469. doi: 10.1007/s13770-016-0026-x.

[10] T. Yeung, P. C. Georges, L. A. Flanagan, B. Marg, M. Ortiz, M. Funaki, N. Zahir, W. Ming, V. Weaver, and P. A. Janmey. Effects of substrate stiffness on cell morphology, cytoskeletal structure, and adhesion. *Cell Motility*, 60(1): 24–34, 2005. ISSN 0886-1544. doi: 10.1002/cm.20041.

[11] J. P. Gong. Why are double network hydrogels so tough? *Soft Matter*, 6(12): 2583–2590, 2010. ISSN 1744-683X. doi: 10.1039/B924290B.

[12] S. Naficy, H. R. Brown, J. M. Razal, G. M. Spinks, and P. G. Whitten. Progress toward robust polymer hydrogels. *Australian Journal of Chemistry*, 64(8): 1007–1025, 2011.

[13] S. Agnelli, F. Baldi, F. Bignotti, A. Salvadori, and I. Peroni. Fracture characterization of hyperelastic polyacrylamide hydrogels. *Engineering Fracture Mechanics*, 2018. ISSN 0013-7944. doi: 10.1016/j.engfracmech.2018.06.004.

[14] A. K. Denisin and B. L. Pruitt. Tuning the range of polyacrylamide gel stiffness for mechanobiology applications. *ACS Applied Materials & Interfaces*, 8(34): 21893–21902, 2016. ISSN 1944-8244. doi: 10.1021/acsami.5b09344.

[15] F. Nilsson. A tentative method for determination of cohesive zone properties in soft materials. *International Journal of Fracture*, 136(1):133–142, 2005. ISSN 1573-2673. doi: 10.1007/s10704-005-5125-y.

[16] Y. Tanaka, R. Shimazaki, S. Yano, G. Yoshida, and T. Yamaguchi. Solvent effects on the fracture of chemically crosslinked gels. *Soft Matter*, 12(39): 8135–8142, 2016. ISSN 1744-683X. doi: 10.1039/C6SM01645F.

[17] T. Baumberger, C. Caroli, D. Martina, and O. Ronsin. Magic angles and cross-hatching instability in hydrogel fracture. *Physical Review Letters*, 100(17): 178303, 2008. doi: 10.1103/PhysRevLett.100.178303.

[18] Y. Tanaka, K. Fukao, and Y. Miyamoto. Fracture energy of gels. *The European Physical Journal E*, 3(4):395–401, 2000. ISSN 1292-8941. doi: 10.1007/s101890070010.

[19] J. B. Bostwick and K. E. Daniels. Capillary fracture of soft gels. *Phys. Rev. E*, 88(4):042410, 2013. doi: 10.1103/PhysRevE.88.042410.

[20] C. Franck, S. Hong, S. A. Maskarinec, D. A. Tirrell, and G. Ravichandran. Three-dimensional full-field measurements of large deformations in soft materials using confocal microscopy and digital volume correlation. *Experimental Mechanics*, 47(3):427–438, 2007. ISSN 0014-4851. doi: 10.1007/s11340-007-9037-9.

[21] J. Notbohm, J. H. Kim, A. R. Asthagiri, and G. Ravichandran. Three-dimensional analysis of the effect of epidermal growth factor on cell-cell adhesion in epithelial cell clusters. *Biophysical Journal*, 102(6):1323–1330, 2012. ISSN 0006-3495. doi: 10.1016/j.bpj.2012.02.016.

[22] J. Notbohm, A. Lesman, D. A. Tirrell, and G. Ravichandran. Quantifying cell-induced matrix deformation in three dimensions based on imaging matrix fibers. *Integr. Biol.*, 7(10):1186–1195, 2015. doi: 10.1039/C5IB00013K.

[23] J. Sutton, H. Schreier, and M. A. Orteu. *Image Correlation for Shape, Motion and Deformation Measurements: Basic Concepts, Theory and Applications*. Springer US, 1 edition, 2009. ISBN 978-0-387-78747-3. doi: 10.1007/978-0-387-78747-3.

[24] H. Abé, T. Mura, and L. M. Keer. Growth rate of a penny-shaped crack in hydraulic fracturing of rocks. *Journal of Geophysical Research (1896-1977)*, 81(29):5335–5340, 1976. doi: 10.1029/JB081i029p05335.

[25] C. H. Yew. Chapter 1 - Fracturing of a wellbore and 2-D fracture models. In *Mechanics of Hydraulic Fracturing*, pages 1–29. Gulf Professional Publishing, Houston, 1997. ISBN 978-0-88415-474-7. doi: 10.1016/B978-088415474-7/50013-0.

[26] E. Bar-Kochba, J. Toyjanova, E. Andrews, K. S. Kim, and C. Franck. A fast iterative digital volume correlation algorithm for large deformations. *Experimental Mechanics*, 55(1):261–274, 2015. ISSN 0014-4851. doi: 10.1007/s11340-014-9874-2.

[27] J. Blaber, B. Adair, and A. Antoniou. Ncorr: Open-source 2D digital image correlation matlab software. *Experimental Mechanics*, 55(6):1105–1122, 2015. ISSN 1741-2765. doi: 10.1007/s11340-015-0009-1.

[28] D. Broek. *Elementary engineering fracture mechanics*. Springer, Netherlands, 1 edition, 1982. ISBN 978-90-247-2580-9. doi: 10.1007/978-94-009-4333-9.

[29] C. T. Sun and Z.-H. Jin. Chapter 6 - Crack tip plasticity. In C. T. Sun and Z.-H. Jin, editors, *Fracture Mechanics*, pages 123 – 169. Academic Press, Boston, 2012. ISBN 978-0-12-385001-0. doi: 10.1016/B978-0-12-385001-0.00006-7.

[30] P. H. Geubelle and W. G. Knauss. Finite strains at the tip of a crack in a sheet of hyperelastic material: I. Homogeneous case. *Journal of Elasticity*, 35:61–98, 1994. doi: 10.1007/BF00115539.

[31] J. R. Rice. A path independent integral and the approximate analysis of strain concentration by notches and cracks. *Journal of Applied Mechanics*, 35(2): 379–386, 1968. ISSN 0021-8936. doi: 10.1115/1.3601206.

[32] T. L. Anderson. *Fracture Mechanics: Fundamentals and Applications, Third Edition*. CRC Press, 2005. ISBN 978-1-4200-5821-5.

[33] X.-K. Zhu and J. A. Joyce. Review of fracture toughness (G, K, J, CTOD, CTOA) testing and standardization. *Engineering Fracture Mechanics*, 85:1 – 46, 2012. ISSN 0013-7944. doi: https://doi.org/10.1016/j.engfracmech.2012.02.001.

[34] C. F. Shih. Relationships between the J-integral and the crack opening displacement for stationary and extending cracks. *Journal of the Mechanics and Physics of Solids*, 29(4):305 – 326, 1981. ISSN 0022-5096. doi: https://doi.org/10.1016/0022-5096(81)90003-X.

[35] R. Zhang and L. F. He. Measurement of mixed-mode stress intensity factors using digital image correlation method. *Optics and Lasers in Engineering*, 50 (7):1001–1007, 2012. ISSN 0143-8166. doi: 10.1016/j.optlaseng.2012.01.009.

Chapter 3

CONFOCAL MICROSCOPY AND DIGITAL VOLUME CORRELATION METHODS FOR INTERGRANULAR FORCE TRANSMISSION EXPERIMENTS

This Chapter is adapted from:

K. A. Mac Donald and G. Ravichandran. “Confocal microscopy and digital volume correlation methods for intergranular force transmission experiments”. *Experimental Techniques*, 2018. DOI: `10.1007/s40799- 018-0292-8`.

Abstract

In this work we develop an experimental method to study interparticle force transmission in 3D. An initial 2D study of volumetric data for commercially available polyethylene fluorescent microspheres shows that three-dimensional effects play a significant role in deformation of real granular assemblies. This highlights the need for more experimental work to validate existing numerical models and motivate further development of theory and models describing real 3D granular media. A full 3D analysis method is described where volumetric images are captured via confocal microscopy and the displacement fields for each particle are determined using digital volume correlation (DVC). This data is then used to determine the average strain in each particle as well as the assembly’s fabric (geometric descriptors of particles and contacts) which are in turn used for the Granular Element Method (GEM) to determine interparticle forces. Additionally, we perform a DVC analysis for an in-house produced polyacrylamide copolymer grain with a volumetric fluorescent speckle pattern. This demonstrates that with sufficiently small particles, it is possible to use our imaging and analysis methodology to determine intergranular force transmission in 3D experiments.

Keywords: confocal microscopy, Digital Volume Correlation (DVC), granular mechanics, intergranular forces, polyacrylamide

3.1 Introduction

Granular materials are important in daily life. From embankments and levees to tunnels and foundations, earthworks of granular media support much of our vital infrastructure. Failure of these structures is critically tied to the mechanics of grain interactions. Similarly, hoppers used in industrial applications such as for processing grain crops or pharmaceuticals also rely on granular mechanics. Here, however, good flow is required to prevent jamming. In all of these cases, the interest is in flow which occurs when shear bands form in a granular assembly. Many previous studies have shown the importance of force chain formation and reconfiguration in predicting shear bands and failure [1–3]. Macroscopic loads are carried by the microscopic grain structure via these force chains. When the load increases beyond a critical limit, force chains break, allowing flow in the shear band [4, 5].

Numerical models have improved greatly as computing power has increased but there is still a need for experimental data to support and validate these multi-scale models [6]. Technological progress has also driven development of experiments in granular kinematics. Improved X-ray computed tomography (XRCT) and 3D X-ray Diffraction (3DXRD) imaging capabilities have allowed for measurement of three-dimensional particle motions and average elastic strains via Digital Volume Correlation (DVC) which have been linked to intergranular forces through the physics-based Granular Element Method (GEM) [7, 8] . This marks a significant improvement from previous methods of photoelasticity which suffer from limited applicability and infinite inverse solutions [9–11]. These experiments have also demonstrated that further investigation of three-dimensional effects may improve our understanding of the mechanics of granular materials and shear band formation [12, 13]. However, they are inherently costly both in time and resources.

DVC is a particularly powerful tool in measuring and understanding 3D kinematics provided there is an appropriate correlation pattern that can be volumetrically imaged. Inherent textures such as the defined grain structures of bone and some metals under diffraction type imaging are highly useful [14, 15]. When such a texture is not inherently detectable, internal patterning appropriate to the imaging method must be applied. For example, fluorescent speckles have been used effectively for DVC analysis of a variety of soft materials [16–18]. Many applications of this patterning method involve the biomechanics of cell-matrix interaction and cell communication [19–21]. When these fluorescent speckles are embedded in an optically transparent matrix, volumetric images can be constructed from a sequence of slices taken from

3D space using laser scanning confocal microscopy (LSCM). A series of pinholes and focusing lenses allow confocal microscopes to capture reflected or transmitted light from discrete points in 3D space. This means that individual voxels are captured with minimal noise from out-of-plane reflections and adjacent voxels [22, 23]. Although this type of raster scanning is relatively slow (on the order of 1 second for a 512×512 2D image), spinning disk and swept-field type systems significantly increase imaging speeds by capturing multiple voxels at the same time (30 fps possible depending on pinhole configuration and camera).

The objective of this study is to show that confocal microscopy combined with digital volume correlation (DVC) and the granular element method (GEM) is a viable alternative to other more costly imaging methods for measuring 3D intergranular force transmission. To this end, we develop an experimental setup and an analysis methodology for such studies which is described in the following sections. First, the model granular materials are described, followed by descriptions of the imaging and experimental apparatus. Then the analysis methods and results are discussed, consisting of an effective 2D analysis of volumetric data and a fully 3D volumetric analysis. Finally, we discuss applicability of this methodology to problems in granular mechanics.

3.2 Materials and Methods

Specimens

The specimens in this study are model granular packings of fluorescent microspheres. Granular assembles labeled Granular 1, 2, and 3 consist of 180-212 μm diameter fluorescent red polyethylene microspheres. Granular 4 consists of similar microspheres with a smaller diameter of 53-63 μm (300-550 nm excitation, 605 nm peak emission, Cospheric). These grains are highly spherical and are on the scale of fine sand and coarse silt, respectively. We expect some cohesion effects between the 53-63 μm particles. Fluorescent marking consists of much smaller fluorescent microspheres within the particle resulting in a random speckle pattern which was detectable on the particle surfaces. Granular 1 and 2 are imaged dry while Granular 3 and 4 are immersed in an index matched immersion fluid (n_a = 1.518 immersion oil, Carl Zeiss Immersol™) of similar optical properties as the spheres themselves. The same immersion oil is also used for the oil immersion objective when imaging Granular 4.

Additionally, some larger, optically transparent and fluorescently marked hydrogel particles are produced in-house using inverse suspension polymerization techniques based on manufacturing processes described in the literature [24–28]. An organic phase reaction column consisting of 80 ml chlorobenzene (MilliporeSigma) and 20 ml xylene (mixed, 97+% purity, Alpha-Aesar®) in a glass-graduated cylinder is prepared in a hot water bath on a heated stirrer. While stirring at 400 rpm, the column is gradually heated to 45°C and 1.00 ml Span® 80 (TCI America) is added as a surfactant to aid in the formation of droplets. A monomer solution consisting of 1.316 ml ACRYL/BIS™19:1 40% solution (AMRESCO®), 3.384 ml deionized water, 0.050 ml ammonium persulfate (APS, AMRESCO®) as a source of free radicals, and 0.25 ml fluorescent microsphere solution is also prepared and chilled in an ice bath to prevent polymerization. The fluorescent microspheres are in a 2% solids aqueous solution of 2.0 μm carboxylate modified polystyrene FluoSpheres® (red, 580nm peak excitation, 605 nm peak emission, Molecular Probes™). Once polymerized, the gel pore size is sufficiently smaller than the microspheres so they remain fixed within the gel spheres. Just before filling a 1 ml capacity syringe with some of the monomer solution, 0.167 ml tetramethylethylenediamine (TEMED, Alfa-Aesar®) is added to the solution and mixed well. A 20g luer stub (blunt needle) attached to the end of the syringe is used to drip the chilled monomer into the heated reaction column. The luer stub aids in producing consistent and small droplets and the stirring in the column prevents droplet coalescence. Particles polymerized quickly due to the relatively large amount of catalyst used and the heat. After one hour the heat is turned off and the column is allowed to cool while stirring continues for another hour. Once completely cooled, the particles are removed from the reaction column and allowed to swell in deionized water for at least 24 hours before imaging. The Suspension Polymerization Particles (SPP 1) are imaged in a bath of deionized water ($n_{\mathrm{a}} = 1.33$) to prevent de-swelling. The water also serves as an imaging medium of similar optical properties as the fully swelled polyacrylamide which is mostly water and thus has a similar index of refraction as water.

Imaging

All experiments are carried out on a Zeiss inverted laser scanning confocal microscope (LSM 800) with Zen Blue System software for image stack capture. Reflected light from diode laser excitation is used to capture images via up to three photomultiplier tubes (PMTs), allowing for capture of multi-channel images, if desired. Different objectives, lasers, and pinhole sizes are used to optimize imaging for each

Table 3.1: Microscope imaging configuration

	Objective			Laser				
	Type	Power ×	NA*	$\gamma^{\dagger}$ (nm)	Intensity (%)	Pinhole (μm)	AU[§]	Gain (V)
Gr 1	PlNeofl	10	0.30	561	0.05	42	1.02	650
Gr 2	Pl Apo	20	0.80	561	0.01	18	0.58	650
Gr 3	Pl Apo	20	0.80	561	0.01	18	0.58	600
Gr 4	Pl Apo	40**	1.4	561	0.05	18	0.51	600
SPP 1	Pl Neofl	10	0.30	561	0.75	40	0.99	650

*Numerical Aperture [†]Wavelength (nm) [§]Airy Units **Oil immersion objective

specimen as indicated in Table 3.1. The pinhole size is selected to optimize the signal to noise ratio. Ideally, the pinhole is the same size as the Airy disc for a given configuration. However, with a strong enough signal, a smaller pinhole can further improve image sharpness. In this study the fluorescent signal was generally very strong, allowing for this improved sharpness in many images. Adjustments to the laser intensity and master gain are used to regulate the number of overexposed voxels throughout image stacks for each test.

Prior to DVC analysis, images of Granular 1 and 2 are deconvolved using Huygens Professional (Scientific Volume Imaging) software to remove standard hardware related spurious image data. Point Spread Functions (PSF) for the deconvolution are determined from microscope and objective data to automatically remove background noise, bleaching effects, and spherical aberrations. Images of Granular 3 and 4 are not deconvolved as the immersion oil between particles improves image quality and clarity significantly. Similarly, images of SPP 1 are also not deconvolved since the water bath also greatly improves the quality and clarity of images.

Experimental Design

A uniaxial compression device mounted to a standard microscope stage insert, shown in Fig. 3.1, is used to apply load via micrometer to the specimen during imaging. The load is applied as incremental displacement steps of 0.010 mm to 0.020 mm with holds for imaging between each loading step.

Specimens are mounted in the loading device using a 13 mm inner diameter PLA ring bonded with super glue to a 25 mm diameter glass cover slip which also serves as a confinement device during compressive loading. Depending on the number of voxels in an image, holds for imaging typically lasted six to thirty minutes. The

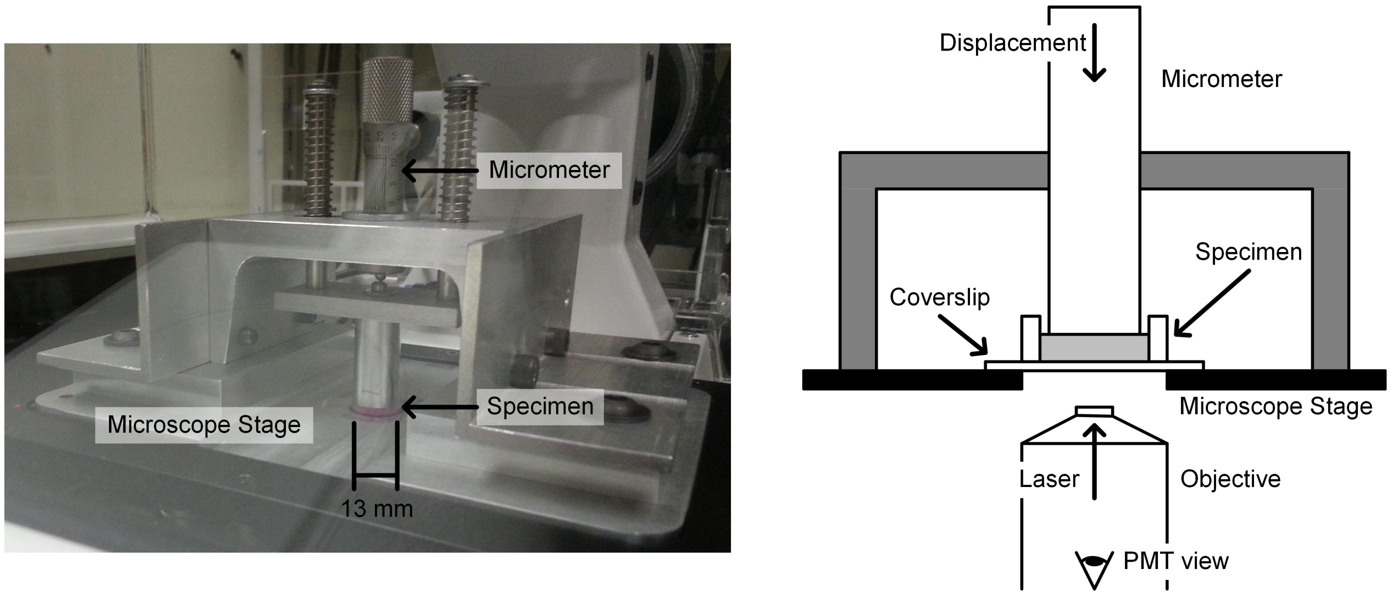

Figure 3.1: Compression loading device mounted to microscope stage showing the micrometer used to apply displacement loading to the specimen.

Table 3.2: Image and voxel dimensions

	Image Size (voxels)			Image Size (μm)			Voxel Size (μm)		
	X	Y	Z	X	Y	Z	X	Y	Z
Gr 1	512	512	109	1277.8	1277.8	703.8	2.50	2.50	6.46
Gr 2	512	512	652	638.9	638.9	424.3	1.25	1.25	0.65
Gr 3	512	512	550	638.9	638.9	356.9	1.25	1.25	0.65
Gr 4	512	512	485	319.5	319.5	150.4	0.62	0.62	0.31
Gr 4*	350	370	200	218.4	230.9	61.8	0.62	0.62	0.31
SPP 1	1024	1024	471	1277.8	1277.8	589.0	1.25	1.25	1.25
SPP 1*	750	750	421	935.9	935.9	526.5	1.25	1.25	1.25

*cropped

image and voxel dimensions used for each specimen are summarized in Table 3.2. In all images, the voxel height (z) to width (x and y) ratio falls between 0.5 and 2.6 to achieve an appropriate z-direction resolution for each specimen. Optimal voxel size can be determined using the Nyquist criterion, which requires a sampling interval of at least twice the resolution of the smallest feature imaged. Practically, this means that the speckles should be larger than a single voxel, ideally at least two voxels in diameter. Resolution is also limited by both the mechanics of the microscope stage and by computation times for the volume correlation.

3.3 Analysis, Results, and Discussion

Initial analysis of Granular 1 shows the potential for applying digital volume correlation (DVC) and the Granular Element Method (GEM) to confocal microscope images of the model granular material. Fig. 3.2 shows one representative slice of a volumetric image. The speckled fluorescent marking on the surface of each sphere is clearly visible even at the relatively low 10× magnification used to capture these images. The gray intensity distribution for this image slice is also shown. Since the grains are discrete, there are a large number of background pixels in the gaps between particles with very low gray values (darker colors) that form a tall but narrow peak in the intensity distribution. A much smoother and wider Gaussian peak represents the gray intensity distribution of the grains themselves. However, there are a relatively large number of overexposed (fully white) voxels. Careful adjustment of laser intensity and PMT gain are necessary to keep the number of overexposed voxels relatively low. Good image correlation requires a wide spread of gray intensities, which is demonstrated by these particles.

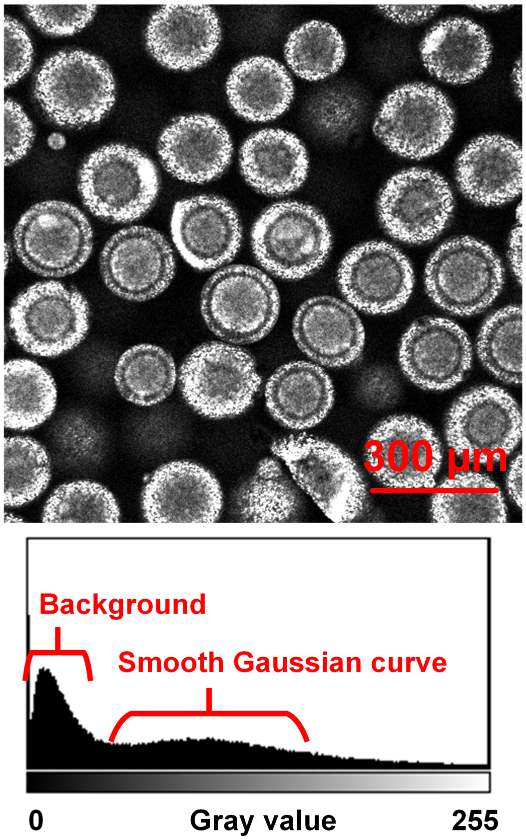

Figure 3.2: Example of 2D speckle pattern of a slice in a 3D granular assembly (Granular 1) with gray scale intensity distribution.

Further analysis of the suitability of these and higher magnification images for DVC is achieved by applying synthetic displacement fields to a representative slice or a 2D projection of 3D data of the volumetric images via the Matlab program DIC_evaluator, developed by Estrada and Franck in 2012 [29]. Comparison of the DIC results with the known synthetic displacement fields allows for determination of the suitability of the speckle pattern. For details on this analysis see the Appendix. Results show that the surface speckle on these fluorescent particles is appropriate for DIC analysis. However, since these images are of discrete particles not of a continuous material, care must be taken to reduce the influence of neighboring particles on displacement results. This is achieved by partitioning images into single particles and then reconstructing the final displacement field from the results for each particle. It should also be noted that the nature of determining deformation gradients using neighboring pixels significantly increases the error and noise in calculated strains, which was observed in the evaluator's strain results.

Images of Granular 2 are taken at a higher magnification (20×) to achieve better definition of the particle surface speckle pattern. Fig. 3.3(a) shows orthographic projections of the volumetric image of this specimen. Due to an index of refraction mismatch between the air and grains combined with poor optical transparency of the grain, imaging is limited to the surface of one side of the particles. To better understand the 3D data, each slice of the volumetric image is added together, forming an effective 2D projection of the intensity data referred to as a z-stack sum and shown in Fig. 3.3(b). This image shows a clear, well defined surface speckle pattern that can be tracked between successive images. Analysis of this 2D projection as well as the 3D volumetric data is considered in the following.

The particles produced using suspension polymerization showed significantly better optical transparency and had an index of refraction extremely close to that of the water surrounding them during the experiment. This allowed for imaging of the fluorescent speckle pattern through the volume of the particles, as can be seen in the orthographic projections and 3D projection shown in Fig. 3.4. Due to the relatively large size of these grains, the number of particles within an image as well as the depth of view was limited. For this reason, specimen SPP 1 includes only two particles and does not capture the entire z-direction. 3D volumetric analysis of these images is still, however, highly valuable.

2D Analysis

A preliminary analysis of 2D projections (z-stack sums) like the one shown in Fig. 3.3(b) is used to understand the in-plane motion of the grains and investigate the validity of 2D experiments in predicting the behavior of 3D granular packings.

DIC is performed on the 2D projection image pairs to determine the in-plane displacements of the individual grains. The DIC code used in this study was developed by Bar-Kochba et al. [30] and uses a fast iterative algorithm equivalent to that used in the DVC counterpart of this code. The resulting correlation coefficients for image pairs are low, indicating that good correlation is achieved. Although minimization of the correlation coefficient is desired, a zero value, which indicates perfect correlation, is actually a sign of an error. The zero values correspond well with gaps between particles where we expected poor correlation based on the DIC_evaluator assessments.

The in-plane displacement results are shown in Fig. 3.5 where points with zero valued correlation coefficients are removed. Examination of the displacement vec-

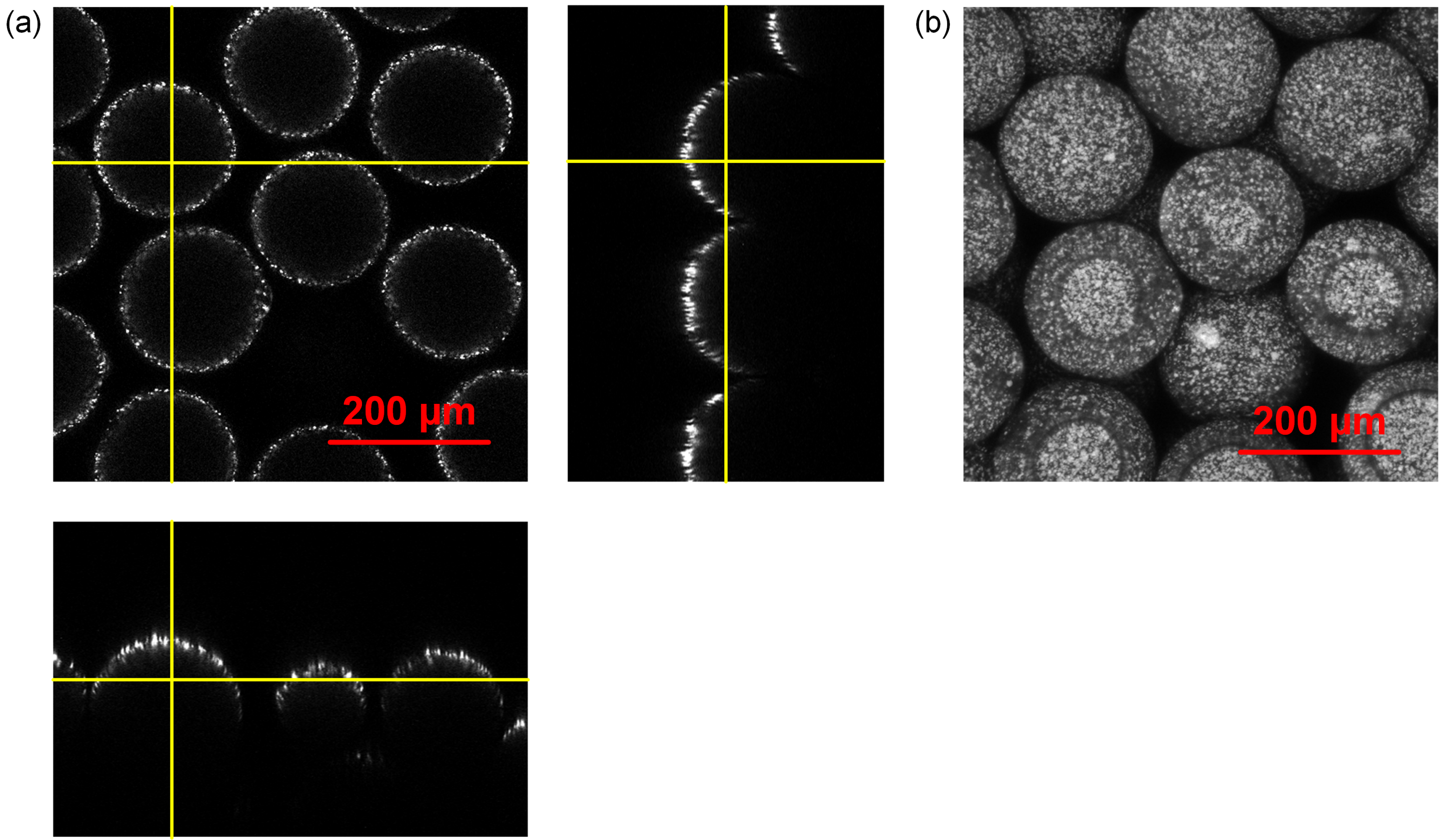

Figure 3.3: Images of the granular assembly specimen, Granular 2: (a) orthographic projections and (b) z-stack sum 2D image.

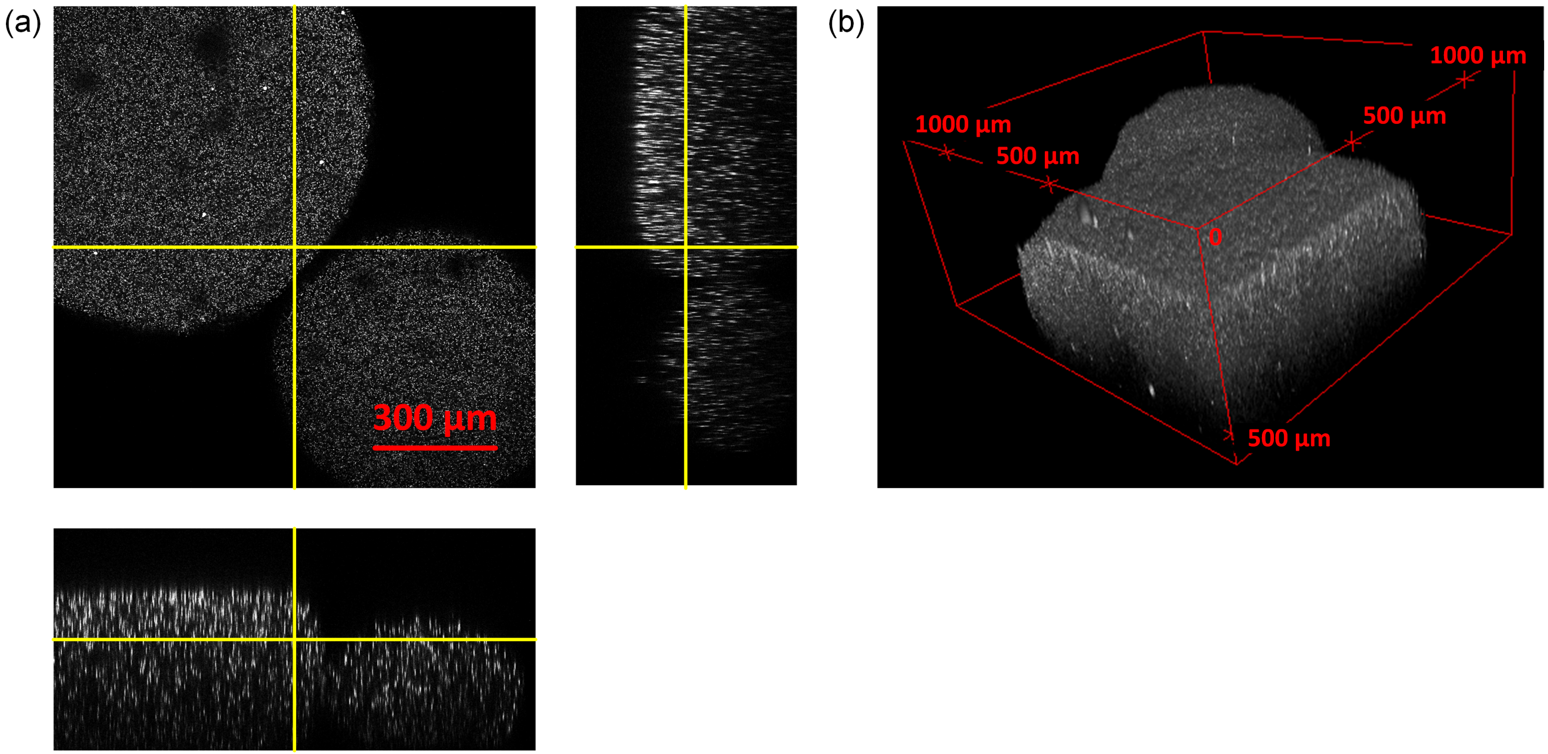

Figure 3.4: Images of Suspension Polymerization Particles (SPP): (a) orthographic projections and (b) 3D projection-view.

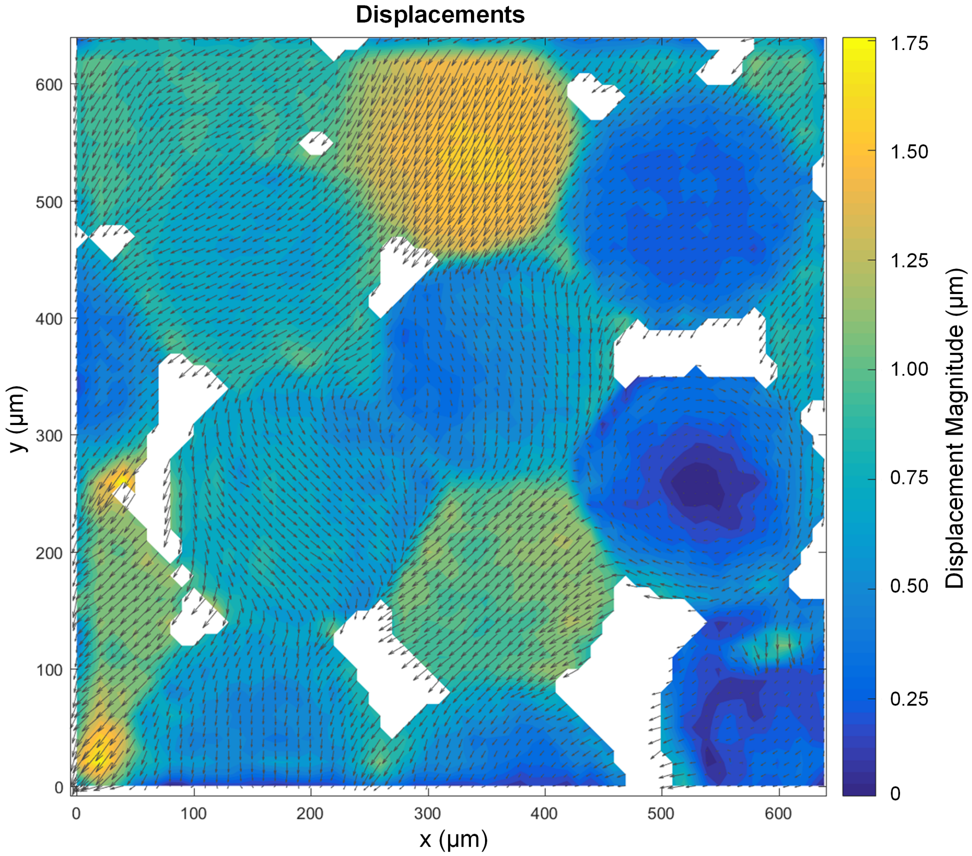

Figure 3.5: 2D DIC displacement results for granular assembly Granular 2 sum image with zero correlation points removed. DIC analysis was performed on the z-stack sum images from the 3D images.

tors show that grain in-plane translations and rotations are captured well. There are suggestions of out-of-plane rotations observed between successive images seen in displacement magnitude variations across grains. This is significantly different than what would be observed in a 2D granular experiment where out-of-plane rotations are inherently restricted by 2D representations of grains.

Strains in the grains are calculated as the displacement gradients across adjacent points. For this 2D analysis, the grain averaged strains are determined by the arithmetic area mean of the strains at each point lying within or on the boundary of each grain. Due to the relatively high stiffness of the polyethylene fluorescent microspheres ($E \sim 0.1 - 1$ GPa) we expect very small grain strains. The applied load, and thus the grain strain, is limited by the strength of the glass cover slip through which images are taken. The grain strains measured in our study are on the order of 0.1% strain. Previous studies using GEM had grain strains an order of magnitude higher than those observed in this study [9].

The Granular Element Method (GEM) uses principles of the Discrete Element Method (DEM) with additional governing equations describing interparticle friction to inversely determine forces between particles at contact points without dependence on a contact law. The inputs for this method are grain averaged strains and fabric. These quantities are used to determine the outputs, interparticle forces. Here, fabric refers to a geometric description of the granular packing. Specifically, contact point locations, master and slave designations, grain volumes (areas in 2D), grain centroid locations, and contact normal and tangential vectors are required. Particles which are only partially imaged at the edges of the field of view are defined as boundary particles for the analysis. The forces exerted by the interior particles onto these boundaries are determined. Fig. 3.6 shows the GEM results for a representative pair of 2D image projections.

Since loading was applied vertically in the z-direction and there is no confinement or bounding walls, one does not anticipate in-plane (x-y) force chains to be present in this experiment. Since there was no way to validate the force magnitudes or determine the z-direction (loading direction) forces, the bars showin in Fig. 3.6 represent the relative magnitudes of the interparticle forces. It is clear that intergranular mechanisms in a 3D granular packing such as grain rotation and sliding (see Fig. 3.5) cannot be appropriately captured by 2D experiments, images, or analyses.

3D Analysis

Following initial exploration of the volumetric data via 2D projections, a fully 3D analysis is performed. The granular images are limited to speckles near the surface and on one side of the particle. As a proof of concept, these images were used to develop the following methodology.

To reduce correlation errors resulting from the discrete motion of each particle, the volumetric images are partitioned into individual grains using a Fiji macro [31]. For each particle, approximate x-y centroid locations are defined and images are cropped to a cylinder with diameter a bit larger than the maximum expected particle size. A series of blurring, thresholding, and watershedding steps allow for particle identification and further cropping based on the actual particle's image size. DVC analysis is performed on image pairs for each identified particle. Final results are shown as a sum of the results from each individual particle after some post-processing to remove spurious correlations. This process is described by the

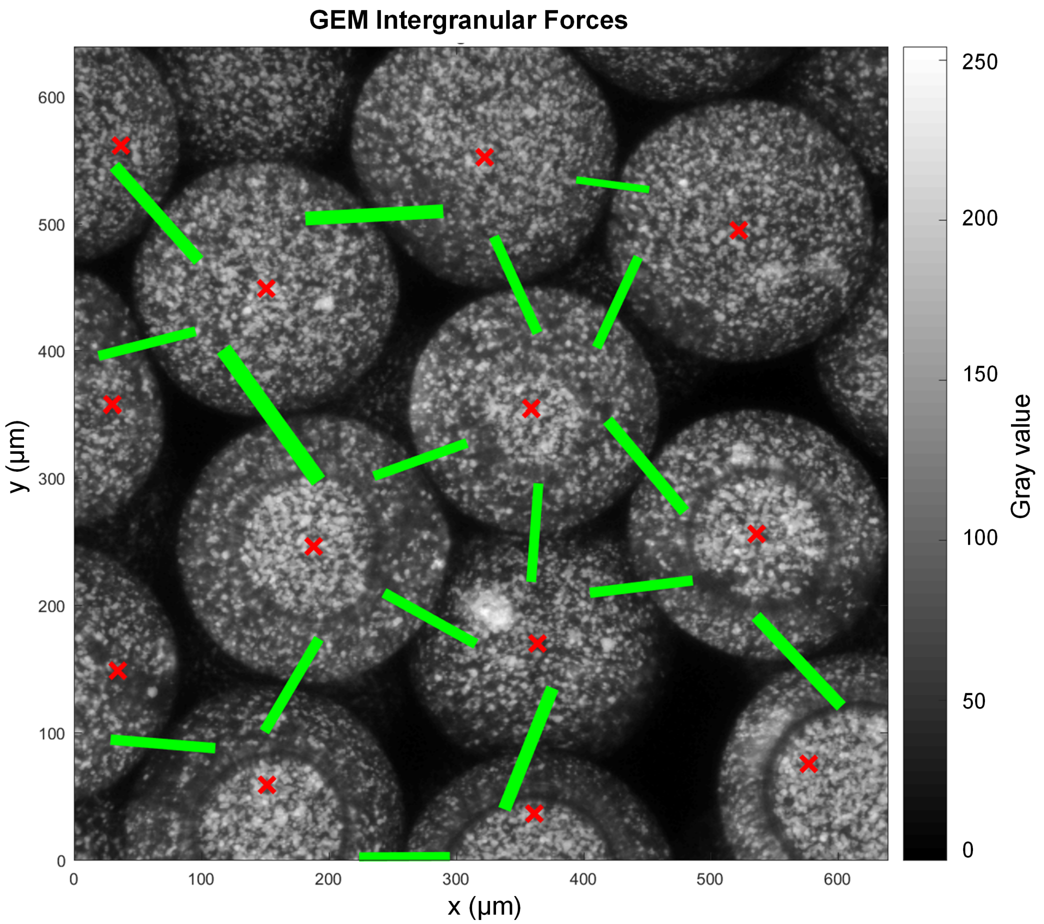

Figure 3.6: Granular Element Method (GEM) analysis results for interparticle forces based on the DIC analysis of the 2D image obtained from the z-stack sums. The direction of the solid lines in the image provides the orientation of the interparticle forces and their size (length and thickness) scales with the relative magnitude of the force.

schematic shown in Fig. 3.7. As in the 2D analysis, post-processing of the DVC outputs includes removing displacement results for which the correlation coefficient is exactly zero. This effectively removes background errors or spurious correlations due to a lack of speckle pattern in the intergranular space and is applied prior to summing the results from individual particles to form the 3D assembled image. Additionally, particles for which the correlation coefficients are NaN (not a number), indicating no correlation, are removed. A case of no or poor correlation results when there is not enough similarity between subsets of subsequent images. Partially imaged particles are again used as boundaries for the analysis.

Fig. 3.8(a) shows the 3D displacement results for Granular 2 where a corner section

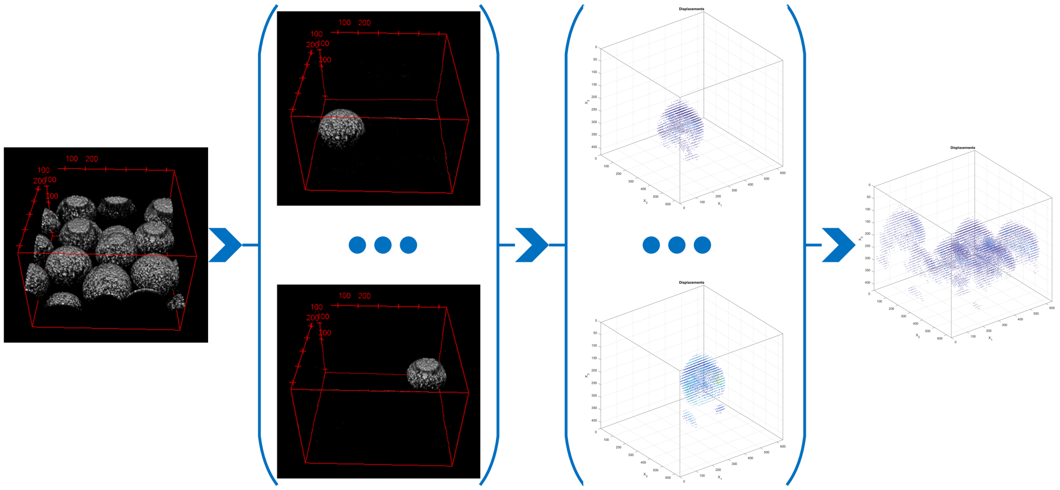

Figure 3.7: Schematic showing how the volumetric image is partitioned into individual grains and then DVC is performed on each individually. Then the individual grains are combined into a complete 3D image of the displacements in the granular assembly.

has been removed from the image to provide an interior view of the displacement fields. These results show no correlation for some of the particles in the images. Examination of the raw image data shows possible moisture accumulation and adhesion between some of the particles and the glass cover slip that affected image accuracy. This appears as raised disks on the surface of particles as seen in the first schematic image in Fig. 3.7 or as dark rings in Fig. 3.3(b), and is a result of refractive index mismatch between the air (imaging medium, $n_a = 1$) and water (accumulated moisture, $n_a = 1.33$). Some partial grain images also had no correlation because too much of the grain moved out of frame between loading steps.

In the 3D case, determining particle averaged strains cannot be accomplished by a simple arithmetic volume mean because the interior displacements, and thus strains, are not known. However, since we do know the displacements on the surface of the particles, we can apply the Divergence Theorem as shown in Eq. (3.1).

$$\begin{aligned} <\underline{\epsilon}>&=\frac{1}{V}\int_{\Omega} sym(\nabla\underline{u})dV \\ &=\frac{1}{V}\int_{\partial\Omega} sym(\underline{u}\otimes\underline{n})dS, \end{aligned} \tag{3.1}$$

where $\underline{u}$ is the displacement vector, $\underline{n}$ is the outward surface normal, and Ω is the volume of the object (grain). Here we have discrete data so we approximate the

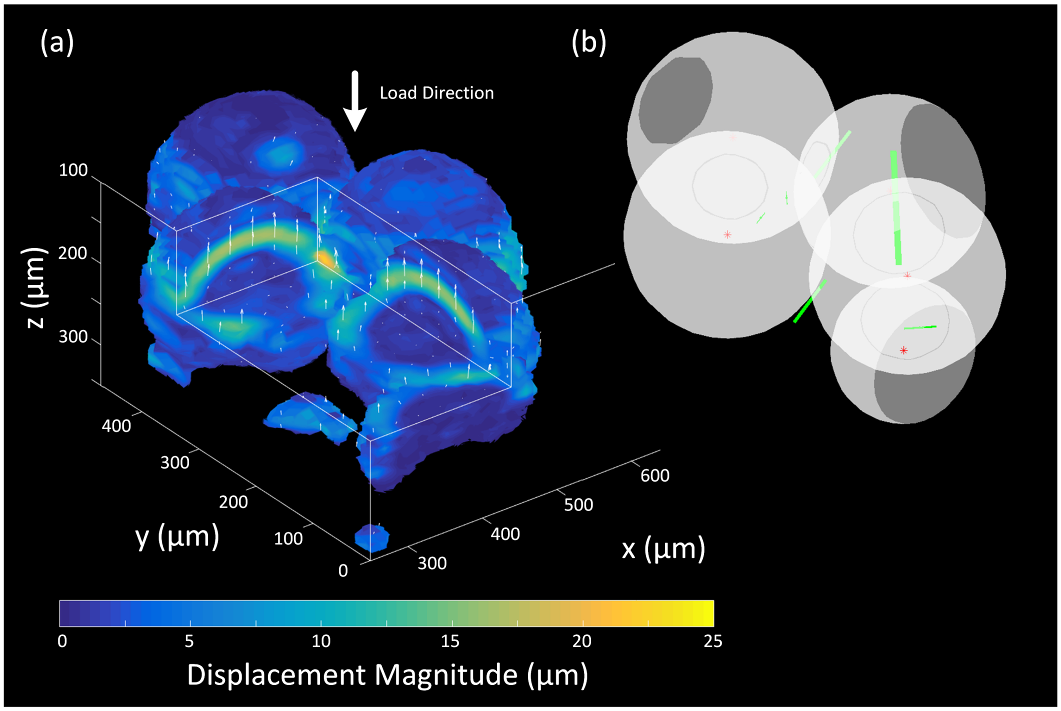

Figure 3.8: (a) 3D displacement results based on the DVC analysis for the granular assembly Granular 2 with zero correlation and no-correlation points removed. A corner section has been removed from the image to provide an interior view of the displacement fields. (b) Representation of the 3D GEM results for the intergranular forces where the solid lines represent relative force magnitudes and orientations, and the stars represent particle centroids.

integral as a sum over the a boundary points as in Eq. (3.2).

$$< \underline{\epsilon} > \approx \frac{1}{V} \sum_{a=1}^{n} sym(\underline{u}^a \otimes \underline{\tilde{n}}^a) \tag{3.2}$$

$$\text{where } \underline{\tilde{n}}^a = \frac{1}{d} \sum_{e} \underline{n}_e^a A_e$$

and e represents the boundary elements connected to each a boundary point, A_e is the area of each boundary surface element, and d is the spatial dimension (in this case, $d = 3$). The boundary nodes are determined as the first and last non-zero valued correlation coefficient points. A tetragonal mesh is created using these boundary points as the nodes for a Delaunay triangulation and the grain surfaces are represented by the mesh free boundary. Further, since only one side of the particles can be imaged, we assume that the average strain in one half of a particle is equal to the average strain in the half of the particle we cannot image. This assumption is only valid for crystalline arrays of particles but quickly breaks down for more random particle arrangements. Since the particles in this experiment are similar in size, we expect their arrangement is close of crystalline.

The 3D granular packing's fabric is determined as follows. Grain centroids are taken to be located at the arithmetic mean of the identified boundary node locations. Grain volumes are determined assuming spherical grains where the radius is calculated as the arithmetic mean of the distance between each boundary node and the grain centroid. Contact point locations are determined by finding the mean location of the nodes with the shortest distance between grains and contact normals are determined as the mean of the surface normals for the corresponding master and slave particles at the contact point location. Knowing the contact normal, a tangent vector can be determined easily using the dot product.

The GEM results for Granular 2 using the above described inputs are shown in Fig. 3.8(b). In this 3D case, significant out-of-plane force components are observed between particles, as expected based on the loading methodology. It is important to note that these are the relative force magnitudes. Due to imaging limitations, only the suggestions of force chains can be observed. Relative interparticle force magnitudes do not appear to agree with those found in the effective 2D study because the out-of-plane component cannot be captured in 2D (see Fig. 3.6).

The analysis methodology described above is also applied to other samples: Granular 3 and a cropped portion of Granular 4. Use of an immersion fluid between the particles eliminates imaging errors due to moisture at grain-cover slip contact points and also allows for clearer, higher quality images. Use of an oil immersion objective for Granular 4 further improves image clarity and quality. However, images are still limited to the surface of one side of the grains and DVC and GEM results are similar to those found for Granular 2. These fluorescent grains do not show sufficient optical transparency to effectively take full volumetric images of individual particles.

The in-house produced suspension polymerization particles do allow for imaging throughout the grain volume when the particles are fully swelled in deionized water. Due to the larger size of the particles produced, only two particles are visible in the SPP 1 images so GEM analysis cannot be performed for these grains. However, DVC analysis is performed on each particle and shows great promise for using similar but smaller grains for a more in-depth study of intergranular force transmission in 3D. Fig. 3.9(a) shows strong variation in the displacement magnitude through the particle which is also captured in the strains. The average strain magnitude for the SPP 1 particle shown in Fig. 3.9(b) is about 1.5% strain, which is on the order of that which is expected for the applied displacement. The strain magnitude is calculated as the Frobenius norm of the strain tensor at each point. Additionally, the measured strain is on the order of the strains reported in previous studies [9]. The swelled polyacrylamide copolymer particles are very compliant, allowing for large, easy to measure displacements and strains appropriate for GEM analyses.

3.4 Conclusions

In this study we explored the potential to use confocal microscopy with digital volume correlation and the granular element method as a viable alternative to more costly and time consuming imaging methods for measuring interparticle force transmission in 3D. Through an effective 2D analysis of volumetric data we were able to show that three-dimensional effects play a key role in the deformation of real 3D granular packings. These 3D motions cannot be effectively captured or measured via 2D methods. Fully volumetric analysis proved challenging due to constraints in optical transparency of some of the granular specimens used in this study. A complete 3D analysis method using grain surface data was completed and showed significant out-of-plane force components between grains, as expected. Additionally, a 3D DVC analysis through the volume of a pair of grains demonstrates that with sufficiently small polyacrylamide copolymer particles it is possible to obtain volumetric data of fluorescent markings within the grains via confocal microscopy which can be used for GEM analysis to determine intergranular forces if the particles mechanical properties are known.

For a the bulk hydrogel used in this study, the Young's modulus was 78 kPa and Poisson's ratio was assumed to be 0.5 (incompressible). However, the properties of the gel when cast as $O(10\mu m)$ microspheres are not known. Single particle compression tests can be used to verify the gel's mechanical properties and validate the assumption of incompressibility. Knowing the material model for the gel spheres opens up numerous avenues for future work. Many experiments can be used to understand the mechanics of failure in granular materials. In this paper we used a simple compression testing setup but the imaging and analysis methods are also applicable to other loading configurations such as shear. Other types of confined and unconfined compression experiments may be used as well as indentation and shear experiments, provided there is a sufficient window for optical imaging and the apparatus can be modified for use in a confocal microscope. Non-spherical particles can also be manufactured by crushing a dehydrated bulk gel and then allowing the resulting particles to swell in water. This would allow us to extend these experiments

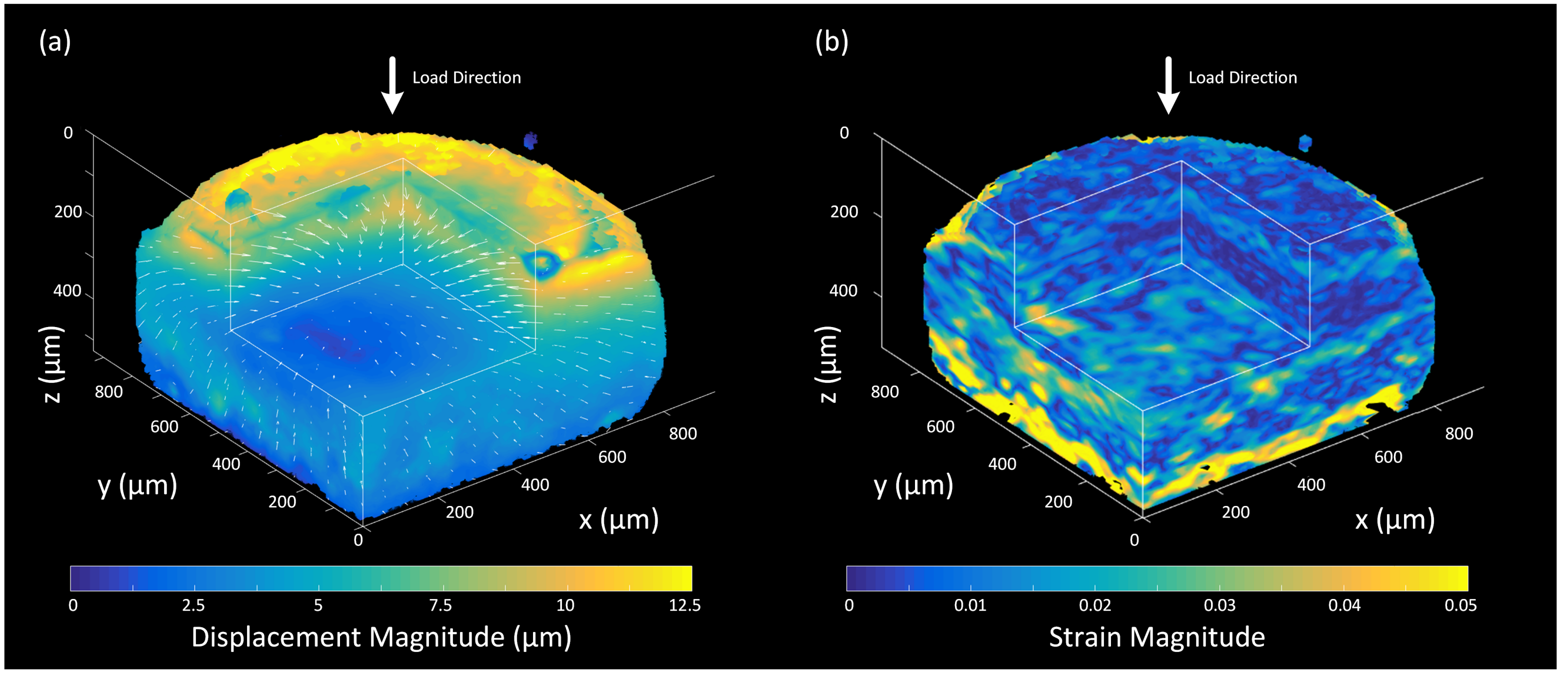

Figure 3.9: (a) 3D displacement results obtained using the DVC analysis of 3D image pairs of the grain in the sample SPP1 with zero correlation and no-correlation points removed. (b) 3D strain magnitudes obtained from the DVC displacement results (Frobenius norm of the strain tensor). A corner section has been removed from both images to provide an interior view of the displacement and strain fields.

to non-ideal or more realistic grain geometries.

Acknowledgments

The project depicted was sponsored by the Department of the Defense, Defense Threat Reduction Agency (HDTRA1-12-0041). The content of the information does not necessarily reflect the position or the policy of the federal government, and no official endorsement should be inferred. This material is based upon work supported by the National Science Foundation Graduate Research Fellowship under Grant No. DGE-1144469 and Award No. DMS-1535083 under the Designing Materials to Revolutionize and Engineer our Future (DMREF) program. Imaging was performed in the Biological Imaging Facility, with the support of the Caltech Beckman Institute and the Arnold and Mabel Beckman Foundation.

REFERENCES

[1] A. Drescher and G. de Josselin de Jong. Photoelastic verification of a mechanical model for the flow of a granular material. *Journal of the Mechanics and Physics of Solids*, 20(5):337–340, 1972. ISSN 0022-5096. doi: 10.1016/0022-5096(72)90029-4.

[2] S. A. Hall, M. Bornert, J. Desrues, Y. Pannier, N. Lenoir, G. Viggiani, and P. Besuelle. Discrete and continuum analysis of localised deformation in sand using X-ray μCT and volumetric digital image correlation. *Géotechnique*, 60: 315–322, 2010.

[3] F. Radjai, D. E. Wolf, M. Jean, and J.-J. Moreau. Bimodal character of stress transmission in granular packings. *Physical Review Letters*, 80(1):61–64, 1998.

[4] S. A. Hall, J. Desrues, G. Viggiani, P. Bésuelle, and E. Andò. Experimental characterisation of (localised) deformation phenomena in granular geomaterials from sample down to inter-and intra-grain scales. *Procedia IUTAM*, 4: 54–65, 2012. ISSN 2210-9838. doi: 10.1016/j.piutam.2012.05.007.

[5] T. S. Majmudar and R. P. Behringer. Contact force measurements and stress-induced anisotropy in granular materials. *Nature*, 435(1079):1079–1082, 2005. ISSN 0028-0836. doi: 10.1038/nature03805.

[6] A. Tordesillas and M. Muthuswamy. On the modeling of confined buckling of force chains. *Journal of the Mechanics and Physics of Solids*, 57(4):706–727, 2009. ISSN 0022-5096. doi: 10.1016/j.jmps.2009.01.005.

[7] J. E. Andrade, K.-W. Lim, C. F. Avila, and I. Vlahinić. Granular element method for computational particle mechanics. *Computer Methods in Applied Mechanics and Engineering*, 241–244:262–274, 2012. ISSN 0045-7825. doi: 10.1016/j.cma.2012.06.012. URL `http://www.sciencedirect.com/science/article/pii/S0045782512002009`.

[8] K.-W. Lim and J. E. Andrade. Granular element method for three-dimensional discrete element calculations. *International Journal for Numerical and Analytical Methods in Geomechanics*, 38(2):167–188, 2014. ISSN 1096-9853. doi: 10.1002/nag.2203.

[9] R. Hurley, E. Marteau, G. Ravichandran, and J. E. Andrade. Extracting interparticle forces in opaque granular materials: Beyond photoelasticity. *Journal of the Mechanics and Physics of Solids*, 63(0):154–166, 2014. ISSN 0022-5096. doi: 10.1016/j.jmps.2013.09.013.

[10] R. C. Hurley, K. W. Lim, G. Ravichandran, and J. E. Andrade. Dynamic inter-particle force inference in granular materials: Method and application. *Experimental Mechanics*, 56(2):217–229, 2016. ISSN 1741-2765. doi: 10.1007/s11340-015-0063-8.

[11] D. Muir Wood and D. Leśniewska. Stresses in granular materials. *Granular Matter*, 13(4):395–415, 2011. ISSN 1434-5021. doi: 10.1007/s10035-010-0237-0.

[12] N. Brodu, J. A. Dijksman, and R. P. Behringer. Spanning the scales of granular materials through microscopic force imaging. *Nat Commun*, 6, 2015. doi: 10.1038/ncomms7361.

[13] S. A. Hall, J. Wright, T. Pirling, E. Andò, D. J. Hughes, and G. Viggiani. Can intergranular force transmission be identified in sand? *Granular Matter*, 13 (3):251–254, 2011. ISSN 1434-5021. doi: 10.1007/s10035-011-0251-x.

[14] A. I. Hussein, P. E. Barbone, and E. F. Morgan. Digital volume correlation for study of the mechanics of whole bones. *Procedia IUTAM*, 4:116–125, 2012. ISSN 2210-9838. doi: 10.1016/j.piutam.2012.05.013.

[15] J. Oddershede, S. Schmidt, H. F. Poulsen, L. Margulies, J. Wright, M. Moscicki, W. Reimers, and G. Winther. Grain-resolved elastic strains in deformed copper measured by three-dimensional X-ray diffraction. *Materials Characterization*, 62(7):651–660, 2011. ISSN 1044-5803. doi: 10.1016/j.matchar.2011.04.020.

[16] C. Franck, S. Hong, S. A. Maskarinec, D. A. Tirrell, and G. Ravichandran. Three-dimensional full-field measurements of large deformations in soft materials using confocal microscopy and digital volume correlation. *Experimental Mechanics*, 47(3):427–438, 2007. ISSN 0014-4851. doi: 10.1007/s11340-007-9037-9.

[17] J. Y. Huang, X. C. Pan, S. S. Li, X. L. Peng, C. Y. Xiong, and J. Fang. A digital volume correlation technique for 3-D deformation measurements of soft gels. *International Journal of Applied Mechanics*, 3(2):335–354, 2011. ISSN 1758-8251. doi: 10.1142/s1758825111001019.

[18] W. R. Liu and R. Long. Constructing continuous strain and stress fields from spatially discrete displacement data in soft materials. *Journal of Applied Mechanics-Transactions of the Asme*, 83(1), 2016. ISSN 0021-8936. doi: 10.1115/1.4031763.

[19] C. Franck, S. A. Maskarinec, D. A. Tirrell, and G. Ravichandran. Three-dimensional traction force microscopy: A new tool for quantifying cell-matrix interactions. *PLoS ONE*, 6(3):e17833, 2011. doi: 10.1371/journal.pone.0017833.

[20] J. Notbohm, J. H. Kim, A. R. Asthagiri, and G. Ravichandran. Three-dimensional analysis of the effect of epidermal growth factor on cell-cell adhesion in epithelial cell clusters. *Biophysical Journal*, 102(6):1323–1330, 2012. ISSN 0006-3495. doi: 10.1016/j.bpj.2012.02.016.

[21] A. Lesman, J. Notbohm, D. A. Tirrell, and G. Ravichandran. Contractile forces regulate cell division in three-dimensional environments. *The Journal of Cell Biology*, 205(2):155–162, 2014. doi: 10.1083/jcb.201309029.

[22] D. M. Sheppard and C. R. J. Shotton. *Confocal Laser Scanning Microscopy*. Number 38 in Royal Microscopy Society Microscopy Handbooks. Springer-Verlag, New York, USA, 1997. ISBN 0-387-91514-1.

[23] T. Corle and G. Kino. *Confocal Scanning Optical Microscopy and Related Imaging Systems*. Academic Press, Burlington, 1996. ISBN 978-0-12-408750-7. doi: 10.1016/B978-012408750-7/50008-2.

[24] B. Brooks. Suspension polymerization processes. *Chemical Engineering & Technology*, 33(11):1737–1744, 2010. ISSN 1521-4125. doi: 10.1002/ceat.201000210.

[25] Q. Gao, C. Wang, H. Liu, C. Wang, X. Liu, and Z. Tong. Suspension polymerization based on inverse Pickering emulsion droplets for thermo-sensitive hybrid microcapsules with tunable supracolloidal structures. *Polymer*, 50(12):2587–2594, 2009. ISSN 0032-3861. doi: 10.1016/j.polymer.2009.03.049.

[26] S. Kiatkamjornwong and P. Phunchareon. Influence of reaction parameters on water absorption of neutralized poly(acrylic acid-co-acrylamide) synthesized by inverse suspension polymerization. *Journal of Applied Polymer Science*, 72(10):1349–1366, 1999. ISSN 1097-4628. doi: 10.1002/(SICI)1097-4628(19990606)72:10<1349::AID-APP16>3.0.CO;2-K.

[27] S. K. Patel, F. Rodriguez, and C. Cohen. Mechanical and swelling properties of polyacrylamide gel spheres. *Polymer*, 30(12):2198–2203, 1989. ISSN 0032-3861. doi: 10.1016/0032-3861(89)90249-8.

[28] M. C. C. Pinto, J. G. F. Santos, F. Machado, and J. C. Pinto. Suspension polymerization processes. In *Encyclopedia of Polymer Science and Technology*. John Wiley & Sons, Inc., 2002. ISBN 978-0-471-44026-0. doi: 10.1002/0471440264.pst597.

[29] J. B. Estrada and C. Franck. Intuitive interface for the quantitative evaluation of speckle patterns for use in digital image and volume correlation techniques. *Journal of Applied Mechanics*, 82(9):095001–095001–5, 2015. ISSN 0021-8936. doi: 10.1115/1.4030821.

[30] E. Bar-Kochba, J. Toyjanova, E. Andrews, K. S. Kim, and C. Franck. A fast iterative digital volume correlation algorithm for large deformations.

Experimental Mechanics, 55(1):261–274, 2015. ISSN 0014-4851. doi: 10.1007/s11340-014-9874-2.

[31] J. Schindelin, I. Arganda-Carreras, E. Frise, V. Kaynig, M. Longair, T. Pietzsch, S. Preibisch, C. Rueden, S. Saalfeld, B. Schmid, J.-Y. Tinevez, D. J. White, V. Hartenstein, K. Eliceiri, P. Tomancak, and A. Cardona. Fiji: An open-source platform for biological-image analysis. *Nature Methods*, 9:676, 2012.

Appendix

DIC_evaluator Analysis

To determine the suitability of a speckle pattern for use as a digital image or volume correlation (DIC or DVC) pattern we use the Matlab program DIC_evaluator. The program applies synthetic displacement fields to an image and then measures the detectable deformations between the original and synthetically deformed images using DIC. It assumes that the material deforms linearly with a Poisson's Ratio of 0.5. Synthetic deformations corresponding to translation, uniaxial tension, pure shear, and point force loading can be applied and the DIC results compared with the known field. Fig. 3.10(a) shows a screen shot of the results for uniaxial tension applied to an example speckle pattern provided with the DIC_evaluator program. We applied 2% strain in the x-direction to the 512 pixel wide image which should result in a maximum x-direction deformation of about ten pixels on the right side of the image, which is approximately what we see in the center plot. In the y-direction we expect zero deformation at the bottom surface and five pixels deformation at the top surface of the image. Although the color bar scale indicates that there is some local error and noise, the right most plot indicates that the measured results are very close to what was applied.

Fig. 3.10(b) shows the DIC_evaluator results for a 2D projection referred to as a z-stack sum from specimen Granular 2. The general trends of the results are similar to those for the example image, indicating that the speckle pattern of these grains is appropriate to capture deformations via image correlation techniques with the 64 pixel subset size and 16 pixel subset spacing used here. There are some significant errors in the measured displacement fields such as in the bottom right corner of the center and right most plots in this row. These errors correspond to areas of the image where the speckle pattern is not appropriate for correlation, such as areas around grains that do not have any speckles or areas where the speckle density is too high and cannot correlate well. While these results suggest that the speckle pattern is usable, we also evaluate a cropped portion of the image centered around a single particle. These results are shown in Fig. 3.10(c) and support our determination that the speckle pattern is appropriate for image correlation.

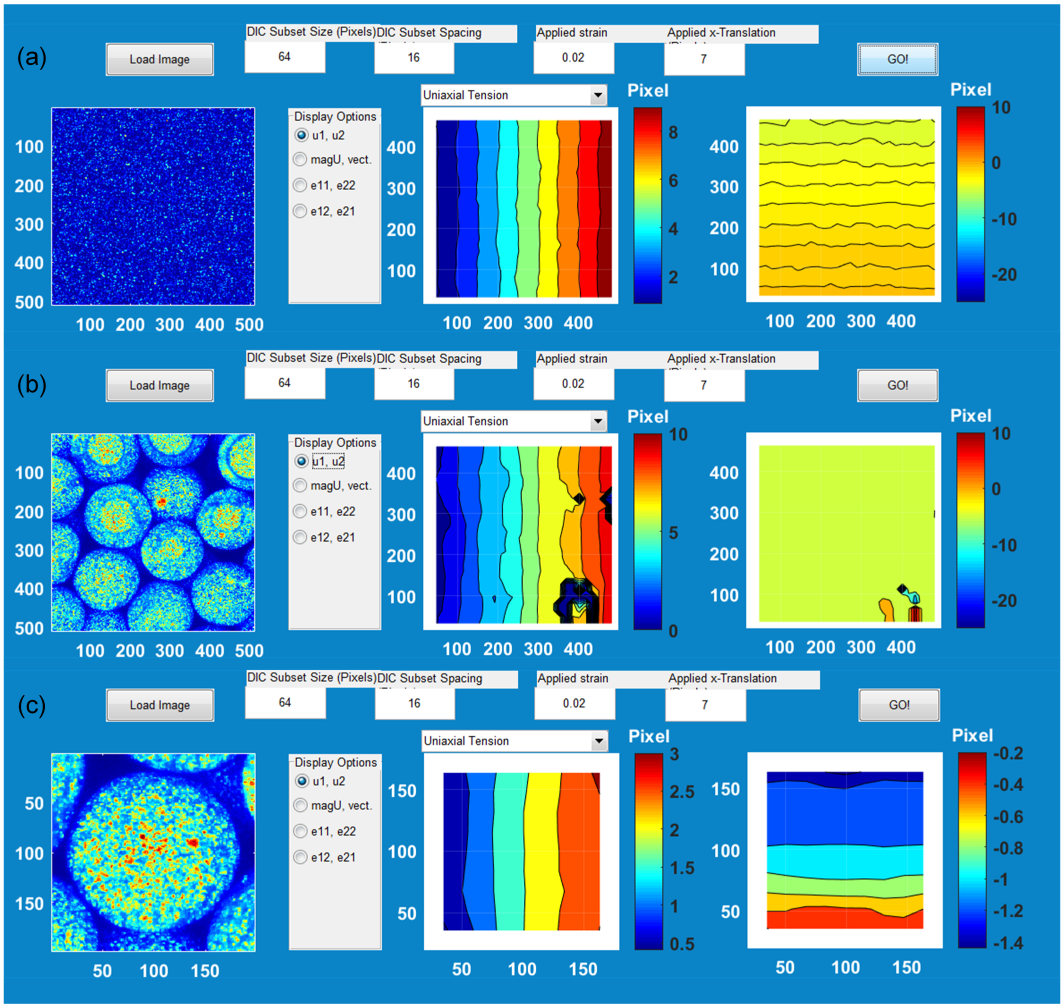

(a)
DIC Subset Size (Pixels): 64
DIC Subset Spacing: 16
Applied strain: 0.02
Applied x-Translation: 7
Uniaxial Tension
Display Options: ● u1, u2 ○ magU, vect. ○ e11, e22 ○ e12, e21

(b)
DIC Subset Size (Pixels): 64
DIC Subset Spacing: 16
Applied strain: 0.02
Applied x-Translation: 7
Uniaxial Tension
Display Options: ● u1, u2 ○ magU, vect. ○ e11, e22 ○ e12, e21

(c)
DIC Subset Size (Pixels): 64
DIC Subset Spacing: 16
Applied strain: 0.02
Applied x-Translation: 7
Uniaxial Tension
Display Options: ● u1, u2 ○ magU, vect. ○ e11, e22 ○ e12, e21

Figure 3.10: Screen shots of the DIC_evaluator results after applying a synthetic displacement field to each image for (a) an example speckle pattern provided with the DIC_evaluator Matlab code, (b) a 2D projection of 3D data for a volumetric image of commercially available particles from specimen Granular 2, and (c) a cropped portion of the image used in (b) centered around a single particle.

Chapter 4

SUMMARY AND FUTURE WORK

The goal of this dissertation is to advance the field of mechanics of materials by improving understanding of deformation and damage processes. Three-dimensional (3D) experimental and quantitative visualization techniques including confocal microscopy, digital image, and digital volume correlation (DIC, DVC) are used to characterize full field displacements. Fracture and granular mechanics experiments give a broad range of applications for these methods where the inherent discontinuities in each of these problems becomes a key factor in the analysis. A range of mechanical quantities from geometry and contact points to material properties and fracture energy are measured through optical imaging. Each study demonstrates these experimental capabilities while improving understanding of deformation and damage processes in materials.

Fluid pressure was used to achieve slow, stable crack propagation in a soft brittle hydrogel. The gel served as a model material for brittle crack propagation while also serving as a material of interest for studying renucleation events. Analysis of fracture energy measured from crack geometry in a 2D internal plane showed constant energy during the propagation event and higher energy needed to renucleate a crack after arrest. Study of renucleation events and 3D crack geometry indicate that toughening mechanisms are a contributing factor in slow crack surface roughening.

An experimental method was also developed to study intergranular force transmission in 3D using simple optical techniques. The method was developed and demonstrated using commercially available microspheres with a fluorescent surface speckle pattern for image correlation. However, the optical properties of these particles were not appropriate for 3D imaging in a confocal microscope. An inverse suspension polymerization method was developed to in-house manufacture customized volumetrically speckled spheres for confocal microscopy imaging and DVC capabilities for these spheres were demonstrated.

4.1 Future Work

The results of the studies presented in this dissertation suggest several new research directions. In the following, a few of these are described.

Mechanics of slow crack roughening

Chapter 2 demonstrated that renucleation events in a networked hydrogel can result in roughening of the crack surface similar to what has been observed by other researchers for slow crack propagation [1–3]. This work also suggests that local toughening leads to the crack arrest and renucleation. Several factors come into play at and near the crack tip. First, there is a large stress concentration immediately ahead of the crack tip. Under high stresses, pore water pressure in the hydrogel increases which, over time, causes water to diffuse out of the gel, and thus is expected to cause water to diffuse away from the region ahead of the crack tip. With lower water content, the gel shrinks and becomes more stiff. Second, there are large deformations causing stretching of the gel network immediately at the crack tip. This stretching opens the gel pores allowing more water to diffuse into that area of the gel further contributing to the increased stresses on the gel network [4–6]. Finally, due to the free-radical polymerization, there may be local variations in the crosslink ratio creating flaws (extra large pores) and both stiffness and toughness variations.

Several new experiments are needed to characterize each of these effects and describe the gel behavior both in theory and in models. The effects of mechanically induced diffusion in the region of the crack tip could be explored by tracking the flow of fluorescent nanoparticles or dyes through the gel network while under load using the experimental configuration described in this dissertation. Care will need to be taken to select a tracking particle sufficiently small to move through the gel's pores and that will not significantly impact the swelling ratio of the gel. The pore radius of the gel used in this work can be estimated as $O(0.01 - 0.1\mu m)$ based on recommendations for molecular size ranges for electrophoresis and data in the literature [7]. Gels with larger pore sizes can be manufactured by decreasing the crosslinker ratio or by decreasing the monomer concentration. Separate experiments with high internal stresses and high surface strains in a bulk gel can help to determine the individual effects of these mechanisms while a fracture experiment can show the net effects.

Local variations in gel properties and pore structure can be explored using atomic force microscopy (AFM) and scanning electron microscopy (SEM) technologies [8].

Images of as cast gels as well as postmortem fracture surfaces can demonstrate how the pore structure impacts crack propagation. It is hypothesized that renucleation sites will be located at or very near to large pores in the gel.

3D analysis of fracture toughening

The experimental design presented in Chapter 2 can also be used to study the effects of toughening mechanisms in 3D. Contrasts in elastic moduli can be introduced by adjusting the gel's crosslink ratio and casting the stiffer and more compliant gels into a single specimen. Many geometries can be considered. A simple planar interface can be achieved by casting a specimen either as two layers or in two halves depending on the desired test geometry. Particle inclusions can also be considered by manufacturing gel spheres as described in Chapter 3 and embedding them in a stiffer or more compliant gel matrix. This will allow for exploration of how cracks navigate inclusions and improve our understanding of the mechanisms that lead to toughening in a 3D sense. Furthermore, this research can lead to improvements in soft, toughened materials for biocompatible implants and devices.

Granular mechanics in 3D

The experimental methods and techniques described in Chapter 3 can be extended to any loading configuration that can be designed on a microscope stage insert and that can be imaged by the confocal microscope. This allows for 3D study of many granular loading mechanisms for coarse silt to fine sand scale grains ($\phi \approx 30 - 250 \mu m$). Since shear failure is a critical and common failure mode in granular structures, experiments that seek to better understand, describe, and model this are of particular interest. Confined compression in a deformable sleeve is one method to study shear and shear band formation in granular materials. However, this experimental geometry poses many challenges for imaging in a confocal microscope. A plate shear experiment, with either a unidirectional plate or a rotating annular plate geometry, would be more compatible with confocal microscopy imaging. Additionally, these geometries would enable better control of the shearing rate, allowing for detailed analysis of force chain reconfiguration.

REFERENCES

[1] T. Baumberger, C. Caroli, D. Martina, and O. Ronsin. Magic angles and cross-hatching instability in hydrogel fracture. *Physical Review Letters*, 100(17): 178303, 2008. doi: 10.1103/PhysRevLett.100.178303.

[2] Y. Tanaka, K. Fukao, and Y. Miyamoto. Fracture energy of gels. *The European Physical Journal E*, 3(4):395–401, 2000. ISSN 1292-8941. doi: 10.1007/s101890070010.

[3] F. Baldi, F. Bignotti, I. Peroni, S. Agnelli, and T. Riccò. On the measurement of the fracture resistance of polyacrylamide hydrogels by wire cutting tests. *Polymer Testing*, 31(3):455–465, 2012. ISSN 0142-9418. doi: 10.1016/j.polymertesting.2012.01.009.

[4] S. Kiatkamjornwong and P. Phunchareon. Influence of reaction parameters on water absorption of neutralized poly(acrylic acid-co-acrylamide) synthesized by inverse suspension polymerization. *Journal of Applied Polymer Science*, 72(10): 1349–1366, 1999. ISSN 1097-4628. doi: 10.1002/(SICI)1097-4628(19990606)72:10<1349::AID-APP16>3.0.CO;2-K.

[5] R. Long and C.-Y. Hui. Crack buckling in soft gels under compression. *Acta Mechanica Sinica*, 28(4):1098–1105, 2012. ISSN 1614-3116. doi: 10.1007/s10409-012-0130-7.

[6] S. Naficy, H. R. Brown, J. M. Razal, G. M. Spinks, and P. G. Whitten. Progress toward robust polymer hydrogels. *Australian Journal of Chemistry*, 64(8): 1007–1025, 2011.

[7] N. C. Stellwagen. Apparent pore size of polyacrylamide gels: Comparison of gels cast and run in Tris-acetate-EDTA and Tris-borate-EDTA buffers. *Electrophoresis*, 19(10):1542–1547, 1998. doi: 10.1002/elps.1150191004.

[8] C. Spagnul, L. C. Turner, F. Giuntini, J. Greenman, and R. W. Boyle. Synthesis and bactericidal properties of porphyrins immobilized in a polyacrylamide support: influence of metal complexation on photoactivity. *J. Mater. Chem. B*, 5(9):1834–1845, 2017. doi: 10.1039/C6TB03198F.